**Università degli Studi di Parma**
Dottorato in Scienza e Tecnologia dei Materiali Innovativi
XXV Ciclo

**Université Rennes 1**
Ecole Doctorale Science de la Matière
*Mention: Chimie*

# *Functional Fluorescent Organic Nanoparticles*

Author:
**Elisa Campioli**

Supervisors:
**Dr. Francesca Terenziani**
**Dr. Mireille Blanchard-Desce**

Coordinator :
**Prof. Enrico Dalcanale**

Parma, 2013

# Contents

# List of Abbreviations

ACQ *Aggregation-Induced Quenching*
AFM *Atomic Force Microscopy*
AIE *Aggregation-Induced Emission*
CT *Charge Transfer*
DFT *Density Functional Theory*
DLS *Dynamic Light Scattering*
DMSO *Dimethylsulfoxide*
EET *Excitation Energy Transfer*
FONs *Fluorescent Organic Nanoparticles*
NIR *Near Infrared*
NPs *Nanoparticles*
PET *Photoinduced Electron Transfer*
PMMA *Polymethylmethacrylate*
QDs *Quantum Dots*
SEM *Scanning Electron Microscopy*
TEM *Transmission Electron Microscopy*
THF *Tetrahydrofuran*
TPA *Two-Photon Absorption*
TPEF *Two-Photon Excitation Fluorescence*
VDWL *Van der Waals-London*

# Introduction

During the past two decades, increasing research attention has been devoted to nanomaterials (materials in the range of 10-100 nm) because of their unique properties. Generally, nanostructures can be divided into inorganic materials, organic macromolecular materials, organic low-molecular-weight nanoparticles and hybrid inorganic-organic nanocomposites.

Zero-dimensional (0D) inorganic nanostructures as nanoparticles, clusters and quantum dots have been well investigated during the last years. For example, works on preparation [1], shape control [2] and size-dependent optoelectronic properties [3] of various nanodevices based on semiconductor quantum dots have been reported by many research groups (such as light-emitting diodes [4], solar cells [5], chemical sensors [6]). Another important area of 0D inorganic nanomaterials is metal [7] and magnetic compound nanoparticles [8] for bio-applications.

Besides inorganic nanomaterials, those composed of macromolecules, such as polymers, biomolecules, dendrimers, ecc., have also been extensively investigated during the past decade. For example, nanospheres have been obtained from polystyrene [9], conjugated polymers [10] or block copolymers [11] by self-assembly and microemulsion processes in solution.

Instead, nanomaterials based on small organic molecules are subject of research only since very recent years, as attested by the few review works on the preparation methods and applications of this type of nanostructures [12, 13]. The reason is twofold: first, these nanomaterials are characterized

by poor thermal instability and mechanical properties that give few routes for nanostructure preparation; second, the optical and electronic properties of the obtained nanoparticles are very difficult to be predicted from the molecular structure. Indeed, differently to what happens in inorganic nanoparticles, weak intermolecular interactions, such as hydrogen bonds, π-π stacking, and Van der Waals contacts, are responsible for the optical and electronic properties of organic nanostructures.

The preparation of organic nanoparticles can be attained principally by two routes:

- the mechanical milling of the raw materials by ultrasounds and/or laser ablation;
- the conversion of the products or educts dissolved in suitable solvents into nanodispersed systems by reprecipitation, condensation or by specific procedures.

At the moment little is know about the molecular processes which take place during the mixing of two starting solutions for producing the state of supersaturation which initiates particles formation. Understanding the mechanism of organic nanoparticles formation is of prime importance because it can lead, by variation of process parameters, to a specific manipulation of final properties, as size, shape, stability, optical behavior, ecc.

However, organic nanomaterials have gained more and more attention for their unique optoelectronic properties such as size-dependent optical properties [14], luminescence [15], large nonlinear optical efficiency [16, 33]; they are thus expected to serve as novel functional materials in electronics and photonics.

Another very recent class of organic nanostructures consists of so-called organic nanocomposites, obtained by two or more different starting compounds. They differ from hybrid inorganic-organic materials because they

are composed only of organic compounds; an example of this new class of nanostructures are doped organic nanoparticles, that show very interesting properties, such as tunable emissions [19].

In this thesis the attention is focused on the preparation and characterization of organic nanoparticles and nanocomposites derived from different types of small organic molecules, their stabilization and the use of these materials as biphotonic probes for bio-imaging [17]. Furthermore, new types of organic binary and ternary nanoassemblies for biologic and optoelectronic applications with unique optical properties have been developed [18].

In Chapter 1 we describe some methods used to obtain this type of nanoparticles focusing the attention on the description of the reprecipitation process and the classical nucleation theory. In the experimental section, we focus the attention on the spectroscopic characterization of fluorescent organic nanoparticle (FONs) suspensions, their colloidal stability during time and the morphological characterization of the obtained nanostructures. We also demonstrate that not all the starting chromophores are adequate to lead stable suspensions.

In Chapter 2 we briefly describe the multiphoton microscopy technique and the most popular inorganic and organic (or hybrid organic/inorganic) biphotonic probes such as quantum dots, dye-loaded silica nanoparticles and nanodots. Then, we focus the attention on the use of fluorescent organic nanoparticles as biphotonic probes and we report a study on FONs designed for this purpose. Those nanostructures have been fully characterized from a spectroscopic and morphological point of view and finally tested for *in vivo* multiphoton microscopy.

Chapter 3 is dedicated to the strategies for stabilizing colloidal nanoparticle suspensions. In the first part of the chapter the most popular strategies of stabilization are described, such as electrostatic, steric and depletion stabilization processes. In the second part we describe two alternative methods to improve the colloidal stability: the use of different types of additives dur-

ing the preparation process, and the molecular design. This last method can be briefly described as conceiving organic dyes whose molecular structure is intended to favor stable colloidal suspensions during time.

The last part of this thesis, Chapter 4, is focused on novel types of organic nanoassemblies conceived to obtain efficient energy and electron transfer between the chromophores that compose the same nanostructure. In the first part of the chapter we describe energy and electron transfer processes from a theoretical point of view, while in the second part we describe the experimental results. In particular, the preparation and the spectroscopic and morphological characterization of fully organic composite and core@shell nanostructures in water are reported. Our novel organic binary core@shell nanostructures show unique photo-luminescence properties related to the very efficient energy transfer process that takes place between the two compounds. These novel materials can be seen as a promising green and biocompatible alternative to the inorganic quantum dots in biological applications. We also report the preparation of ternary core@shell@shell nanoassemblies able to provide energy transfer cascade between the three compounds, and the improvement of their photo-luminescence during time by the use of a commercial polymer. In the last part of the chapter we describe the preparation and some preliminary experimental results of a core@shell nanostructure designed for electron transfer. The properties of this last type of nanosystem are actually under study.

# Chapter 1

# Organic Nanoparticles: Preparation and Characterization

This chapter is basically divided into three parts: in the first part the reprecipitation methods for the preparation of organic nanoparticles and the classical nucleation theory are described; in the second part the characterization methods for the detection of optoelectronic and morphological characteristics of nanostructures are briefly summarized; the last part focuses on the experimental results on some fluorescent organic nanosuspensions obtained from different organic chromophores.

## 1.1 Preparative Methods

Organic nanoparticles are nanoaggregates entirely composed by organic molecules (or polymers); their dimension is typical of nano-objects, with diameter in the range of 10 - 100 nm.

Nanodispersed organic systems can be generally obtained in two ways:

- by mechanical milling of bulk materials (ultrasounds or laser ablation);

- by precipitation or condensation of the products or educts.

In both techniques, additives such as surfactants and polymers can be added as colloidal stabilizers.

The use of ultrasounds in milling processes is, in principle, unsuitable for the production of systems with a narrow size distribution because this technique favors the aggregation of smaller particles [12]. Instead, with the use of laser ablation, concentrated nanoparticle dispersions have recently been obtained [20, 21, 22]. In this method microcrystals are suspended in water (or another solvent in which molecules are not soluble) and exposed to intense laser pulse that induce the fragmentation of the microcrystals.

An overview of the production of organic nanoparticles in aqueous media by precipitation and condensation methods is reported in Figure 1.1. Starting from a hydrophobic organic compound, three types of processes can be differentiated depending on the type of solvent [12]:

1. **Lipophilic solvent** (I and II). In this case nanoparticle formation takes place in o/w microemulsion, thanks to the evaporation of the lipophilic solvent that promotes the conversion of the emulsion into a nanodispersion.

2. **Hydrophilic solvent** (IV and V). In this process the particle formation occurs by precipitation because of high level of supersaturation obtained by mixing the organic hydrophilic solvent and water.

3. **Amphiphilic solvent** (III). With the use of this type of solvent, nanoparticle formation takes place through a transient emulsion phase that evolves towards a nanodispersed state.

Aqueous nanoparticle dispersions from polymers are also called pseudolatex, while those obtained from small organic molecules are also called hydrosols,

as reported in Figure 1.1. In this thesis the attention is focused on the process that allows to obtain hydrosols (I and V), as described below in detail.

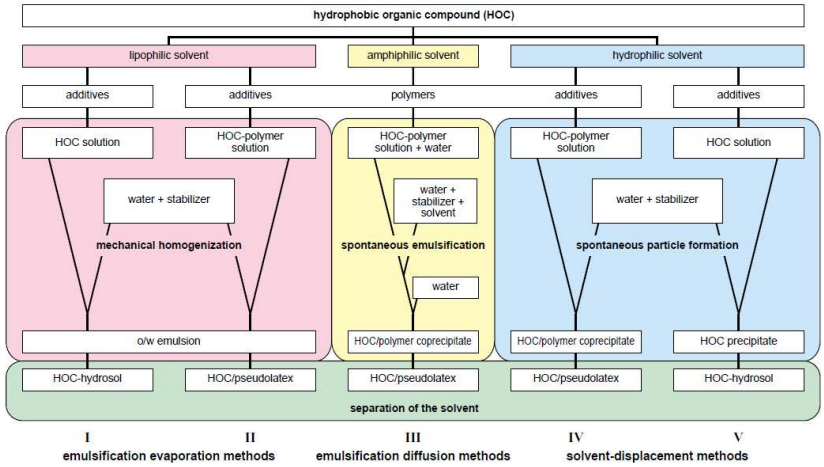


*Figure 1.1: Precipitation and condensation processes for the preparation of organic nanoparticles [12].*

### 1.1.1 Hydrosols Systems from Hydrophilic Solvents

The precipitation method to obtain organic nanoparticles was first reported by Nakanishi and coworkers in 1992 [23, 24]. It involves a solvent-exchange process: a concentrated solution of a hydrophobic compound, dissolved in an organic hydrophilic solvent, is rapidly introduced into a large amount of water under vigorous stirring. The rapid mixing of the stock solution with the poor solvent changes the micro-environment of the molecules and induces the precipitation of the compound, which generally forms micro/nanoaggregates or micro/nanocrystals. Hydrophilic solvents used for setting the highest supersaturation possible can be small-chain alcohols, acetone, acetonitrile or tetrahydrofuran (THF). In detail, the following conditions must be fulfilled:

- Nucleation must take place at the highest level of supersaturation possible to maximize the nucleation rate.
- The limitation of particle growth and the setting of a narrow size distribution require a controlled and rapid reduction in supersaturation subsequent to the nucleation step. This can be achieved using sufficiently low active-compound concentration so that secondary crystallization or particle agglomeration processes can be limited. The use of additives as specific growth inhibitors can also be considered.

With the reprecipitation method, a series of organic nanoparticles were successfully prepared by several groups. For example, Nakanishi's, Majima's and Barbara's groups prepared and studied perylene nanoparticles [25, 26], Horn and coworkers prepared nanoparticles from β-carotene [27] and Yao's and Park's groups studied the size dependence of the luminescence and the enhanced emission of nanoparticles prepared in this way [28, 29].

The reprecipitation can be monitored by UV-Vis absorption spectroscopy, recording spectra at different time delays after the initial mixing. When any change in the spectrum is no more detectable, the reprecipitation process can be considered as come to an end. Depending on the properties of the molecule, some hours or few seconds are required (Figure 1.2).

### 1.1.2 Hydrosols Systems from Lipophilic Solvents

The preparation of the nanoparticles can be carried out by dissolving the active compound together with an emulsifier in a suitable lipophilic solvent, then emulsifying this solution with an aqueous solution and finally removing the organic solvent by distillation. The actual precipitation/crystallization takes place in the emulsion droplets during distillation, when the solubility limit is crossed. The final size of the particles depends on the size of the emulsion droplets and the concentration of the active compound. The particle morphology is usually polycrystalline since the solid formation takes

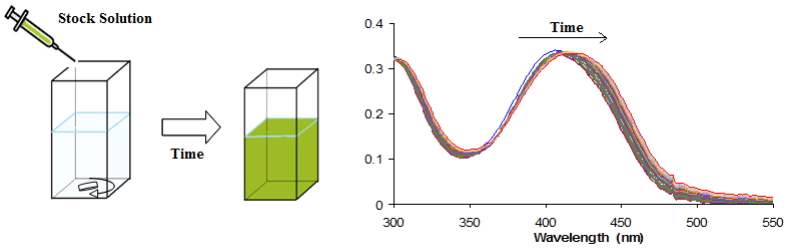


*Figure 1.2: In the precipitation method an amount of a stock solution of the small organic compound in an organic hydrophilic solvent is added to a large volume of water under vigorous stirring (left). The process can be monitored by UV-Vis absorption spectroscopy (right).*

place by evaporation at low supersaturation. An inherent difficulty in this process lies in the removal of as much solvent as possible from the final product [12]

## 1.2 Theoretical Approaches

### 1.2.1 Classical Nucleation Theory

Despite a century of investigations, the nucleation process is still not completely understood. This is particularly true for nanoparticle systems in which nucleation is typically rapid and can be strongly coupled to both growth and Ostwald ripening. One of the most widely accepted models for colloid nucleation is the classical homogenous equilibrium nucleation theory [30].

#### 1.2.1.1 Homogenous Nucleation: Thermodynamic Aspects

For the formation of nanoparticles by homogenous nucleation, a supersaturation of growth species must be created in liquid solution: when the concentration of the solute in a solvent exceeds the solubility limit a new phase appears.

The thermodynamic drive force (or supersaturation) for phase transformation is given by the difference between the chemical potentials of the two individual phases forming the phase boundary. For a liquid-solid system this is given by:

$$\Delta\mu_v = \mu_{solid} - \mu_{liquid} \tag{1.1}$$

where $\mu_{solid}$ and $\mu_{liquid}$ are the chemical potentials of the liquid and solid phases, respectively. Assuming that in diluted solutions activity approximates molarity and assuming solid incompressibility, the chemical potentials of a bulk species (radius $\rightarrow \infty$) are given by:

$$\mu_{liquid} \approx \mu_e + RT \ln\left(\frac{C}{C^0_{flat}}\right) \tag{1.2}$$

$$\mu^{flat}_{solid} \approx \mu_e \tag{1.3}$$

where $R$ is the gas constant in units $JK^{-1}mol^{-1}$, $T$ is the temperature $(K)$,

$\mu_e$is the equilibrium chemical potential ($J/mol$), $C$ ($mol/m^3$) is the real concentration and $C^0_{flat}$ is the equilibrium concentration for a surface with infinite curvature. The supersaturation can therefore be expressed as

$$\Delta\mu_v^{flat} = -RT\ln\left(\frac{C}{C^0_{flat}}\right) = -RT\ln S \tag{1.4}$$

where $S = C/C^0_{flat}$ is typically termed the supersaturation ratio. For systems where the solid phase crystallizes with a finite size (i.e. for nanoparticles), one has to account for the increase of the chemical potential of the solid caused by the significant surface free energy contribution. For spherical particles this factor is described by the Kelvin equation:

$$\mu_s(r) = \mu_{solid}^{flat} + \frac{2\gamma V_m}{r} \tag{1.5}$$

where $\gamma$ is the surface tension ($Jm^{-2}$) and $V_m$ is the molar volume ($m^3/mol$). By combining equations 1.1, 1.2 and 1.5 an expression for the size-dependent chemical potential change for the nucleation of a spherical particle is obtained:

$$\Delta\mu_v(r) = \Delta\mu_v^{flat} + \frac{2\gamma V_m}{r} \tag{1.6}$$

If thermodynamic equilibrium, $\Delta\mu_v(r) = 0$, is assumed, by combining equations 1.4 and 1.6, the Gibbs-Thomson equation is attained:

$$C(r) = C^0_{flat}\exp\left(\frac{2\gamma V_m}{RTr}\right) \tag{1.7}$$

In essence, this relation describes the equilibrium concentration of monomer needed in solution to sustain a particle of radius $r$. This relationship is at the heart of all nucleation phenomena and has been invoked in practically every growth model of colloids. Its main limitation lies in the questionable definition of surface energy for nanometer sized particles.

The classical nucleation theory assumes that nuclei must overcome a

potential energy barrier due to the newly forming surface area in order to reach a metastable particle size. The maximum in this potential barrier corresponds to the critical radius $r^*$, where the particle is at equilibrium with the solution monomer as governed by the Gibbs-Thomson equation. The barrier to nucleation can be determined directly by calculating the free energy ($\Delta G$) needed to create a nucleus with size $r$:

$$\Delta G = \frac{4}{3}\pi r^3 \Delta G_v + 4\pi r^2 \gamma \tag{1.8}$$

where $\Delta G_v$ is the change in the Gibbs free energy per unit volume ($J/m^3$) and is related to the chemical potential energy through $\Delta \mu_v = V_m \Delta G_v$. The first part of 1.8 accounts for the favorable free energy associated to the formation of a defined volume of material, while the second part accounts for the free energy associated with the unfavorable formation of the surface. Figure 1.3 reports the plot of the overall free energy as a function of the particle size. When the particle size increases below the critical radius ($r < r^*$) the free energy of the system increases because the surface component of the Gibbs free energy dominates over the thermodynamically favorable volume component. As the size increases further ($r > r^*$), the volume component begins to make the major contribution to the barrier to nucleation, so that the free energy decreases. The critical radius, corresponding to the barrier maximum, represents the boundary between thermodynamically stable and unstable nanoparticles. Nanoparticles smaller than $r^*$ are unstable, so that they will dissolve, while those that are larger ($r > r^*$) will grow into bigger particles.

The critical radius $r^*$ and the activation energy can be found by setting to zero the first derivative of $\Delta G$ :

$$r^* = -\frac{2\gamma}{\Delta G_v} = \frac{2\gamma V_m}{RT \ln S} \tag{1.9}$$

$$\Delta G^* = \frac{4\pi\gamma}{3} r^{*2} \tag{1.10}$$

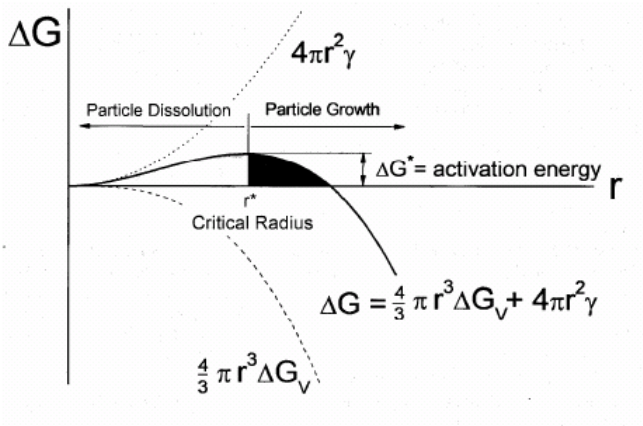


*Figure 1.3: A schematic of the Gibbs free energy of nucleation. Particles with a radius $r < r^*$ redissolve, those with $r > r^*$ grow further.*

#### 1.2.1.2 Homogenous Nucleation: Kinetic Aspects

The nucleation rate, that is the number of nuclei which form per unit time and volume can be written as:

$$J = K_J \exp\left(-\frac{\Delta G^*}{k_B T}\right) \tag{1.11}$$

where $K_J$ is a factor (weakly dependent on temperature) determined by the frequency of the process and $k_B$ is the Boltzmann constant. Combining equations 1.11 and 1.10:

$$J = K_J \exp\left(-\frac{16\pi V_m^2 \gamma^3}{3N_A^2 k_B^3 T^3 \left(\ln S\right)^2}\right) \tag{1.12}$$

If we observe the plot of $J$ as a function of $S$ (Figure 1.4) we can recognize a metastable zone (under the so-called critical supersaturation) where, even if the solution is supersaturated, nucleation is almost negligible because the

rate $J$ is too low (for low values of $\gamma$).

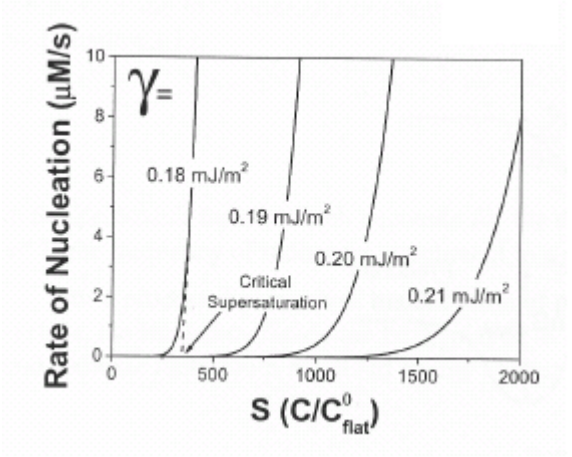


*Figure 1.4: The rate of homogenous nucleation given by equation 1.12 for variable $\gamma$.*

An interplay between thermodynamics and kinetics is always occurring for a given nucleation event. It is important to note that nucleation is always occurring concurrently with growth. As such, the nucleation event coupled with growth acts to rapidly deplete the monomer concentration from the system. The resulting decrease in supersaturation suppress any further nucleation. Growth and Ostwald ripening at this point become the two major mechanisms of evolution for a colloidal ensemble.

Figure 1.5 schematically illustrates the process of nucleation and subsequent growth. When the concentration of the solute increases as a function of time, the nucleation occurs if the supersaturation reaches a certain value above the solubility. After the initial nucleation, the concentration of the solute decreases and the change of Gibbs free energy reduces; there is a moment in which nucleation and growth are inseparable processes. When the concentration decreases below a specific concentration, which corresponds to the critical energy, no more nuclei would form, whereas growth will pro-

ceed until the concentration of growth species has attained the equilibrium concentration or solubility.

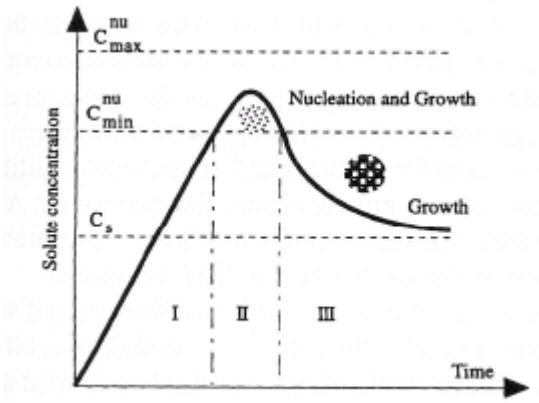


*Figure 1.5: Schematic of the process of nucleation and subsequent growth (La Mer's diagram [31]).*

#### 1.2.1.3 Mechanism of Growth

For the preparation of nanoparticles with uniform size distribution, it is best if all nuclei are formed at the same time. In this case, all the nuclei are likely to have similar size, since they are formed under the same conditions. In addition all the nuclei will have the same subsequent growth. In practice, to achieve a sharp nucleation, the concentration of the growth species is increased abruptly to a very high supersaturation and then quickly brought below the minimum concentration for nucleation. The size distribution of nanoparticles can be further altered in the subsequent growth process, depending on the kinetics.

A general analysis of the growth process is important to understand nanocrystal synthesis. In general, the surface to volume ratio in smaller

particles is quite high. As a result of the large surface area, it is observed that surface excess energy becomes more important in very small particles. Hence, for a solution that is initially not in thermodynamic equilibrium, a mechanism that allow the formation of larger particles at a cost of the smaller particles reduces the surface energy and hence plays a key role in the growth of nanoparticles.

Coarsening effects, controlled either by mass transport or diffusion, are often termed the Ostwald ripening process. This process is dominated by the surface energy of the particle. The chemical potential of a particle increases with decreasing particle size so the equilibrium solute concentration for a small particle is much higher than for large particles, as described by the Gibbs-Thompson equation 1.7. The resulting concentration gradients lead to transport of the solute from the small particles to the larger particles [32].

### 1.2.2 Aggregation

Aggregation phenomena play a critical role in the preparation of many colloidal systems, so that explanations are needed for the condition under which colloids are stable, or how particles themselves can be aggregated or flocculated in a targeted manner [12]. There are two main types of colloidal forces: van der Waals interactions and electrical double-layer interactions [33].

#### Van der Waals Force

The Van der Waals force ($F_{disp}$) between two identical spherical particles of radius $r$ at separation $D$ ($D <$ 10-100 nm) can be described by the Hamaker equation [34]:

$$F_{disp} \cong \frac{Ar}{12D^6} \tag{1.13}$$

where $A$ is the Hamaker constant, a property of the material and the environment. Since $A$ is positive, the van der Waals interaction is attractive.

### Electric Double-Layer Interactions

Electrostatic interactions originate due to the presence of induced charges at particle surfaces. The charge is concentrated at the particle/solvent interface, forming a thin layer of negligible dimension in comparison with the particle size. The surface charge is compensated by a charge of opposite sign distributed throughout the continuous phase in order to fulfill the overall electroneutrality condition. In the case of polar media (aqueous solutions) an electrical double layer is formed (Figure 1.6), which affects most of the dynamic phenomena occurring in colloidal systems, as well as their stability. However no complete theory has yet emerged on this subject. At present, two main paths of thinking about the double layer exist:

- A phenomenological approach based on the local thermodynamic balance (DLVO theory) [36];
- The statistical-thermodynamic approach [37].

The former approach is less strict and, as such, it is applicable to a broad range of situations of practical interest, while the more general statistical-thermodynamic approach produces rather specific results, so that it is mainly applicable for planar geometry.

Without going into the mathematical details it must be pointed out that the presence of the electrical double-layer creates a potential around the particle called zeta-potential, that is directly related to the surface potential, as shown in Figure 1.6.

The stabilization of nanoparticle dispersions against aggregation requires the presence of an energy barrier between the particles that prevents their approach when the van der Waals attraction is large. Two general mechanisms for the stabilization of suspensions can be offered. The first is referred to as electrostatic stabilization and is based on charge separation and formation of electrical double layers in aqueous medium, which determines the repulsion of particles and prevents aggregation; the second is the use of

surfactants or polymers around the particle surface that prevent, by electrostatic or steric interactions, the formation of aggregates [38]. It has been empirically demonstrated that nanoparticle suspensions with zeta-potential absolute values above 30 mV can be considered stable.

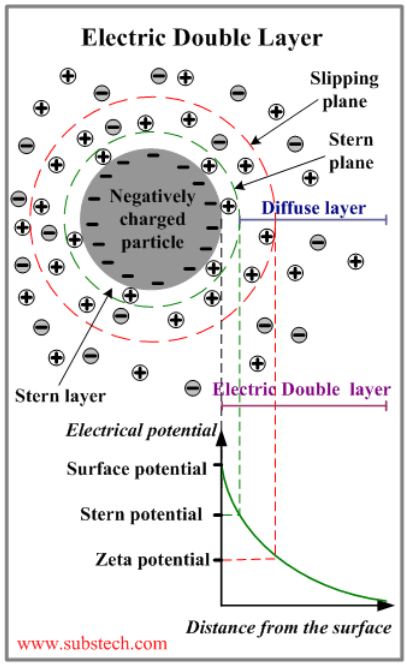


*Figure 1.6: Schematic of electrical double layer at the surface of a nanoparticle.*

## 1.3 Characterization Methods

In general it is very hard to follow experimentally the formation of organic nanoparticles from the timepoint when supersaturation is realized, because the particle formation during precipitation occurs on a short time scale, down to millisecond for some systems. In most cases a description of the mechanism of particle formation is still limited to a retrospective derivation from the structure of the particles formed [12]. Anyway, it is possible to follow the formation of nanoparticles by UV-vis spectroscopy and to establish when reprecipitation is complete (Figure 1.2). The formation and the growth of nanoparticles affect the optical properties of the suspension: generally a decrease on absorption maximum (i.e. extinction coefficient) and a shift (often towards the red) of the maximum are observed from the supersaturation time until the end of the process. When no changes are any more detectable on the absorption spectrum of the colloid, the reprecipitation can be considered as come to an end.

Characterization of the as-prepared suspensions is done by using a variety of different techniques, which depend on the properties of interest. Generally, nanoparticle properties are divided in optoelectronic and morphological properties, often related to each other.

### 1.3.1 Optoelectronic Properties

It was found that the optical and electronic properties of organic nanomaterials are fundamentally different from those of their inorganic counterparts, because the intermolecular interactions in organic materials are basically of weak types, such as hydrogen bonds, π-π stacking, van der Waals contacts and charge transfer (CT) interactions. The resulting properties, such as size-dependent optical properties [39], size-tunable emission, multiple emission [40], tunable/switchable emission [41], aggregation-induced emission [42] are principally studied by UV-vis and fluorescence spectroscopy and fluorescence microscopy in the case of micro-structures. Nonlinear optical properties,

such as two-photon excitation fluorescence (TPEF) and two-photon absorption (TPA), can be studied by TPEF spectroscopy (see Appendix 2) or Z-scan method.

### 1.3.2 Morphological Properties

There are various techniques for detecting, measuring and characterizing the morphology of nanoparticles. There are methods that give informations on an amount of nanoparticulate material and those that can look at the individual nanoparticle within the sample. Sometimes they are combined to extract more information from one sample.

The common techniques used to characterize the morphology of nanoparticles (size, shape, dispersity) are electron microscopy, such as transmission electron microscopy (TEM) or scanning electron microscopy (SEM), atomic force microscopy (AFM) and dynamic light scattering (DLS), Table 1.1.

#### 1.3.2.1 Microscopy Methods

Transmission Electron Microscopy (TEM) uses an electron beam to interact with a sample to form an image on a photographic plate or specialist camera. The sample must therefore be able to withstand the electron beam and also the high vacuum it is subjected to. The sample preparation is a delicate procedure, as a thin sample on a support grid must be prepared. Furthermore, for organic samples (such as organic nanoparticles), a contrasting agent is required: typically uranyl acetate or ammonium molybdate are used.

Scanning Electron Microscopy also uses a high-energy electron beam but the beam is scanned over the surface and the back scattering of the electrons is looked at. The sample must again be kept under vacuum and it must be electrically conductive at the surface. This can be achieved by sputter coating a non-conductive sample. This requirement can be restrictive and this technique can be time consuming and expensive.

Atomic Force Microscopy is a form of Scanning Probe Microscopy. It

*Table 1.1: Morphological characterization techniques for Organic Nanoparticles*

| Technique | Measures | Sample | Sensitivity |
|---|---|---|---|
| **TEM** | **Particle size and characterization** | **It must be deposited on a carbon grid and be stable under an electron beam and a high vacuum** | **From 1 nm** |
| **SEM** | **Particle size and characterization** | **It must be conductive or sputtered coated** | **From 1 nm** |
| **AFM** | **Particle size and characterization** | **It must adhere to a substrate and be rigid and dispersed on the substrate** | **1 nm - 8 μm** |
| **DLS** | **Average particle size and size distribution** | **It must be a very diluted suspension** | **10 nm - 10 μm** |

uses a mechanical probe to probe the surface of a sample. A cantilever with a nanoscale probe is moved over the surface of a sample and the forces occurring between the probe tip and the sample are measured from the deflection of the cantilever. The deflection moves a laser spot that reflects into an arrangement of photodiodes. This can offer a 3D visualization. Air samples or liquid dispersions can be looked at and AFM is less costly and time consuming than TEM or SEM. However the sample must adhere to a substrate and be rigid and dispersed on it. The roughness of the substrate must be less than the size of the nanoparticles being measured.

#### 1.3.2.2 Dynamic Light Scattering

DLS measures the scattering pattern produced when light is shown through a sample. It combines this with calculations of the diffusion caused by

Brownian Motion in the sample in a relationship described by the Stokes-Einstein equation. This gives an estimation of the average particle size and distribution of particle size through the sample. The sample must be a liquid, a solution or a suspension. It must also be very dilute, otherwise the scattering of light can be unclear. The technique is sensitive to impurities and the viscosity and pH of the sample must be known.

## 1.4 Experimental

In this section the preparation and characterization of fluorescent organic nanoparticles (FONs) performed in my PhD work are reported. All the nanoparticle suspensions have been obtained through the reprecipitation method, starting from different chromophores (all molecular structures reported in Appendix 1). In particular the experimental studies are focused on a series of families of organic molecules with different properties (described in the next sections):

- Triphenylamine-based derivatives
- Thiophene-based derivatives
- Bodipy-derivatives
- Commercial laser dyes: **Nilered** and **DCM**

The studied systems are surely not exhaustive to describe the variety of organic nanoparticles that could be prepared, but they have been chosen to demonstrate that it is possible to obtain nanoparticles from chemically different organic structures with the specific goal of obtaining fluorescent nanosystems to be exploited for bioimaging or photovoltaic devices. The properties of the obtained nanoparticles (spectroscopic, morphological, stability) depend on the molecular structure of the constituent chromophores and are related to the solid-state properties, but predicting them safely and accurately is not straightforward.

From an empirical point of view, in order to obtain nanoparticles that preserve fluorescence on aqueous suspension, it is necessary to start from a solid-state fluorescent dye, insoluble in water and soluble in organic solvents. However, it must be pointed out that not all organic dyes with the described characteristics yield stable nanosuspensions in water. For example, in some cases (**Nilered** and **DCM**) the nanosuspensions are not stable and precipitate after few minutes or hours, in other cases nanoparticles are

stable during few days and then they aggregate or precipitate. In conclusion it is possible to approximately predict their emitting behavior (if they will be fluorescent or not and the raw color of fluorescence), but it is very hard to predict their stability.

The next sections are divided according to the molecular families. For every family, the most important structural characteristics of the chromophores are introduced and the experimental results about spectroscopy and morphology of the nanoparticles are reported.

### 1.4.1 Triphenylamine-based derivatives

A series of triphenylamine-based derivatives[1], which belong to the family of conjugated molecules called charge-transfer (CT) or push-pull chromophores, are tested for the preparation of organic nanoparticles (called **T1**, **T2**, **T3** and **T4**, see Figure 1.7).

CT chromophores are constituted by electron-donor (D) and electron acceptor (A) groups, linked by a π-conjugated bridge to form molecules of different symmetry and dimensionality. A dipolar push-pull molecule is composed by a single electron-donor group and a single-electron acceptor group linked together by a π-bridge. A quadrupolar push-pull chromophore has two D (or A) groups linked to an A (or D) group to give linear centrosymmetric structures. In so-called octupolar chromophores a planar structure is formed linking three A (or D) groups to a central D (or A) group, according to a $C_3$ symmetry axis.

On the basis of this description, **T1** and **T3** are dipolar molecules, while **T2** and **T4** are octupolar chromophores (Figure 1.7). All these triphenylamine-based derivatives have the same electron-donor group, constituted by an amino group; for **T1** and **T2** the electron-acceptor group is an aldehydic group while for **T3** and **T4** a cyano-vinyl or dicyano-vinyl group.

A spectroscopic study of chromophores **T1, T2** and **T3** in different sol-

[1]Synthesized by M. Blanchard-Desce's group.

vents has been achieved by Sissa et al [43].

The experimental results on the obtained nanoparticle suspensions are divided into two groups, according to the molecules and FONs emission: **T1-T2**, that emit in the yellow-orange region and **T3-T4** that emit in the orange-red region.

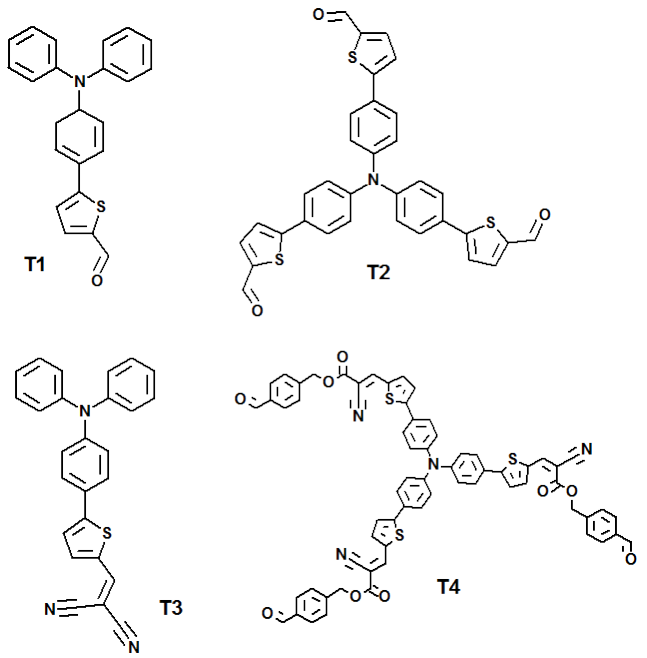


*Figure 1.7: Molecular structure of triphenylamine-based chromophores used for the preparation of nanoparticle suspensions.*

#### 1.4.1.1 T1 and T2 Nanoparticle Suspensions

**Preparation**

Nanoparticles of **T1** and **T2** were prepared through the standard reprecipitation process.

Tetrahydrofuran (THF) is chosen as the organic solvent, because the

compounds are well soluble in this medium and high concentrations can be attained. Stock solutions are prepared at a concentration of $1 \times 10^{-3} M$. An aliquot of the organic stock solution is mixed with a known amount of water under vigorous stirring to reach the final nominal dye concentration of $2 \times 10^{-5}$M. This corresponds to high dye supersaturation in the medium. To the naked eye, just after mixing, the dye suspensions change color and their fluorescence decreases. The suspension of **T2** FONs remains clear while the suspension of **T1** FONs progressively becomes cloudy. Nanoparticle formation has been monitored through UV-Vis spectroscopy (Figure 1.8): the absorption spectrum of the suspension changes during particle growth. When no further changes are detectable on the absorption spectrum, the nanoparticle formation is considered as accomplished. For **T1** chromophore the reprecipitation process takes place in about 2 hours; the scattering signal increases during time (see the broad spectral feature developing as time elapses, Figure 1.8) because of the growth of nanoparticles and/or the presence of nanoaggregates, thus explaining the cloudiness of the final suspension [17].

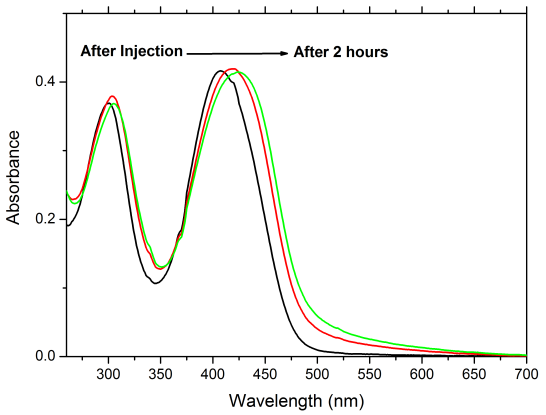


*Figure 1.8: Evolution of the UV-Vis absorption spectrum of **T1** during the reprecipitation process in water/THF 98:2 v/v.*

### Spectroscopic Characteristics of the Suspensions

Absorption and fluorescence spectra are recorded for the dye suspensions in the native aqueous mixture, at the end of the reprecipitation process. Table 1.2 and Figure 1.9 collect the data obtained for **T1** and **T2** FONs, together with data for the dyes in organic solvents of different polarity. The absorption spectra of the FON suspensions in water show an intense absorption band peaking around 418 - 422 nm. A broadening of the main absorption band of FONs (Figure 1.9) and a marked hypochromic effect (see Table 1.2) are observed as compared to the dyes dissolved in organic solvents. A reduction of 36% and 34% of the maximum extinction coefficient is obtained for **T1** FONs and **T2** FONs, respectively, as compared to that of the corresponding dyes in chloroform. Whereas the absorption spectrum of **T1** nanoparticles in water is red-shifted with respect to that of **T1** dissolved in organic solvents (including polar dimethylsulfoxide, DMSO), the absorption band of **T2** nanoparticles peaks at similar wavelength as that of **T2** dissolved in chloroform. Regarding fluorescence properties, the emission maximum of **T1** FONs falls in the green spectral region, and is comparable to that of **T1** in chloroform. On the other hand, **T2** FONs show a yellow-orange emission, the emission spectrum resembling the spectrum of **T2** in highly-polar solvents, such as DMSO. Moreover, the emission spectra of the suspensions are quite close to those of the dyes in the solid state (Figure 1.10). This suggests that the molecular arrangement could be quite similar in both cases, and the small differences in the spectra may be explained by the crystal defects, by finite-size effects, and the aqueous environment of the FONs. The fluorescence quantum yield was found to be 0.15 and 0.02 for the suspensions of **T1** and **T2**, respectively. These values are lower than those of the dyes dissolved in chloroform or even in more polar organic solvents, such as DMSO, where the quantum yields are found to be 0.25 and 0.10 for **T1** and **T2**, respectively. The fluorescence decays of all the samples dissolved in organic solvents are found to be monoexponential with fluores-

cence lifetimes in the nanosecond range. On the contrary, the fluorescence decays are found to be bi-exponential in nanoaggregates (Table 1.2).

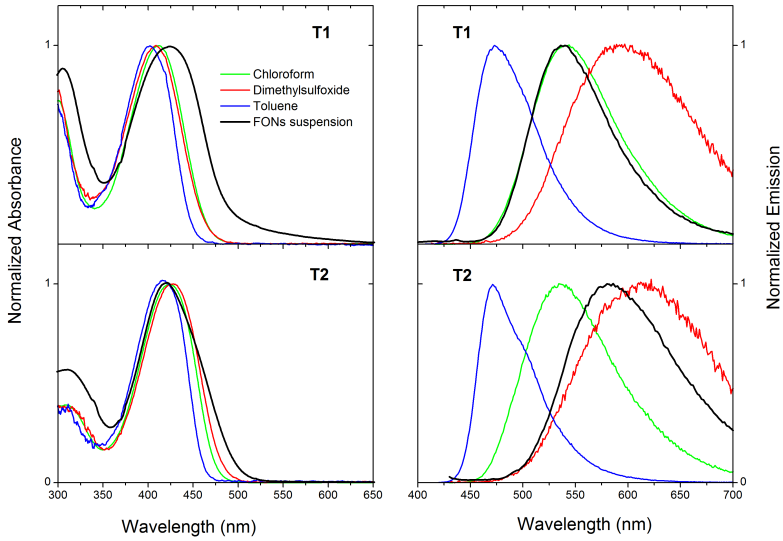


*Figure 1.9: Absorption (left panel) and emission (right panel) spectra of the **T1** and **T2** solutions in organic solvents and of their FON suspensions [17].*

*Table 1.2: Spectroscopic characteristics of **T1** and **T2** in different solvents and of their FONs in aqueous suspensions.*

| | Solvent | $\lambda_{abs}^{max}$ [nm] | $\lambda_{em}^{max}$ [nm] | ε [$\times 10^4$ $M^{-1}cm^{-1}$] | Φ[a] | τ [ns][b] |
|---|---|---|---|---|---|---|
| T1 | Toluene | 400 | 473 | 2.87 | 0.89 | **2.57** |
| | Chloroform | 411 | 541 | 2.80 | 0.82 | **4.03** |
| | Dimethylsulfoxide | 409 | 593 | 2.65 | 0.25 | **2.04** |
| | FONs | 418 | 538 | 1.80[c] | 0.15[d] | **0.98 (0.43); 3.38 (0.57)** |
| T2 | Toluene | 411 | 470 | 6.38 | 0.68 | **1.79** |
| | Chloroform | 423 | 536 | 6.35 | 0.63 | **4.09** |
| | Dimethylsulfoxide | 428 | 610 | 6.09 | 0.10 | **1.09** |
| | FONs | 422 | 582 | 4.20[c] | 0.02[d] | **0.84 (0.55); 3.40 (0.45)** |

*[a] Fluorescence quantum yield estimated using Fluorescein as reference ($\phi = 0.90$) [b] Fluorescence lifetimes and, in parentheses, corresponding fraction of the fluorescence decay [c] Referring to total dye concentration [d] Fluorescence quantum yield measured using an integrating sphere in center-mount sample holder configuration*

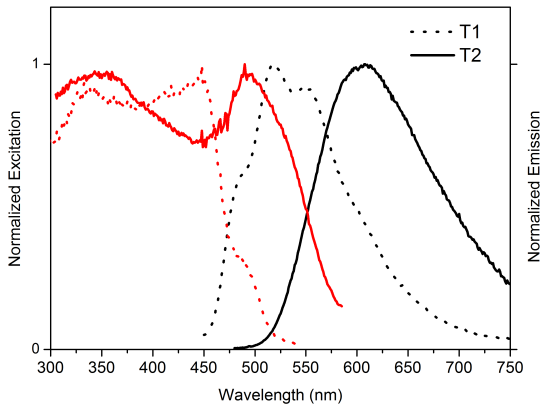


*Figure 1.10: Excitation (left, red) and emission (right, black) fluorescence spectra of **T1** (dotted line) and **T2** (solid line) in the solid state.*

### Morphological Characteristics of Nanoparticles

The suspensions of **T1** and **T2** FONs, observed by TEM, show spherical particles measuring about 30-40 nm in diameter, which tend to agglomerate. To test the stability of the particles, suspensions are left to stand in the dark at room temperature during 3 weeks (Figure 1.11). No difference in the particle size is found for **T2**, but the agglomerates are bigger than in freshly-prepared suspensions. For **T1**, the average size of the particles after the elapsed time is about 100 nm, that is more than twice their original size, and the size of the agglomerates is also increased significantly. It must be pointed out that the observation of aggregates on TEM grids could be also an effect of the evaporation of the solvent on the support, so that it is not a definite proof of the formation of aggregates in the suspension. These observations indicate that the nanoparticles of the octupolar dye **T2** are more stable than those of the dipolar dye **T1** over long periods of time. The observations by TEM are also supported by the observations of the suspensions to the naked eyes during time: **T1** suspension becomes progressively more cloudy and after some weeks it is possible to observe the formation of micro-aggregate, instead suspension **T2** remains limpid and uniform for weeks and no micro-aggregates or powders are detectable. There could be different explications for the growth of **T1** nanoparticles during time: one is that **T1** is partially soluble in water and the molecules in solutions add to the formed nanoparticles during time; another is the Ostwald ripening, so the bigger particles grow thanks to the dissolution of the smaller ones.

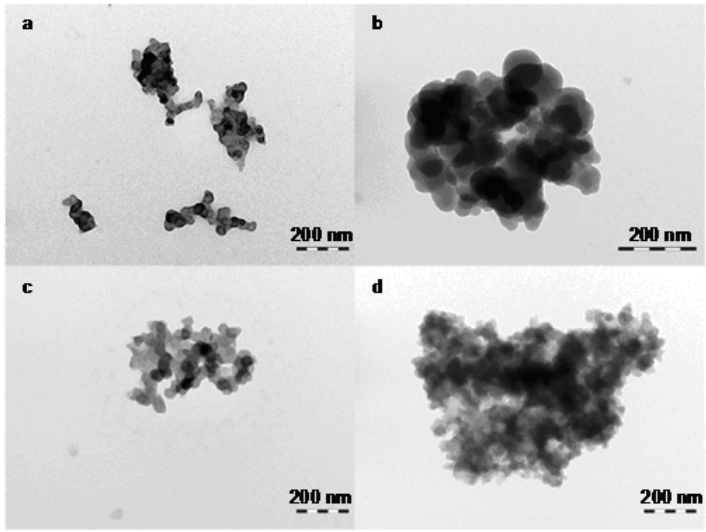


*Figure 1.11: Observation by TEM of the particles of* ***T1*** *freshly prepared (a) and after 3 weeks (b) and* ***T2*** *freshly prepared (c) and after 3 weeks (d).*

#### 1.4.1.2 T3 and T4 Nanoparticle Suspensions

**Preparation**

Preparation of **T3** and **T4** nanoparticle suspensions follows the same procedure described for **T1** and **T2**. After 30 minutes under vigorous stirring the reprecipitation is completed and the obtained FON suspensions are limpid and red-purple colored.

**Spectroscopic Characteristics of the Suspensions**

Figure 1.12 and Table 1.3 collect the spectroscopic data of **T3** and **T4** FONs and of the dyes dissolved in organic solvents of different polarity. The absorption spectra of the FON suspensions in water show an intense absorption band peaking around 500 nm for both systems and no shifts are observed compared to the dyes in solution. As in the case of **T1** and **T2**, a broadening of the main absorption band of FONs is observed as compared to dyes in organic solvents, but in this case no scattering tail is observed. Regarding fluorescence properties, the emission of **T3** and **T4** FONs falls in the red spectral region, and is comparable to those of **T3** and **T4** in dichloromethane. The fluorescence quantum yield was found to be 0.03 for both the suspensions.

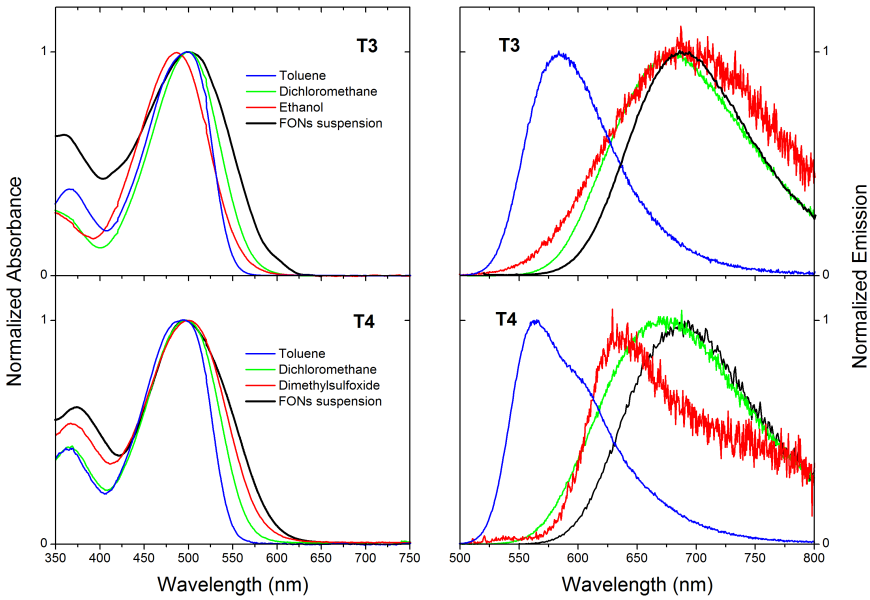


*Figure 1.12: Absorption (left panel) and emission (right panel) spectra of the **T3** and **T4** solutions in organic solvents and of their FON suspensions in water.*

*Table 1.3: Spectroscopic characteristics of **T3** and **T4** in different solvents and of their FONs in aqueous suspensions.*

| | Solvent | $\lambda_{abs}^{max}$ [nm] | $\lambda_{em}^{max}$ [nm] | $\Phi^a$ |
|---|---|---|---|---|
| T3 | Toluene | 500 | 584 | - |
| | Dichloromethane | 500 | 680 | - |
| | Ethanol | 486 | 687 | - |
| | FONs suspension | 500 | 689 | 0.03[b] |
| T4 | Toluene | 494 | 564 | 0.44 |
| | Dichloromethane | 488 | 672 | 0.16 |
| | Dimethylsulfoxide | 500 | 637 | 0.01 |
| | FONs suspension | 500 | 686 | 0.03[b] |

*[a] Fluorescence quantum yield estimated using Fluorescein as reference ($\phi = 0.90$). [b] Fluorescence quantum yield measured using an integrating sphere in center-mount sample holder configuration.*

### Morphological Characteristics of Nanoparticles

**T3** FONs, observed by TEM, show spherical and polydispersed particles measuring from 20 nm to 100 nm in diameter, while **T4** FONs display an irregular shape (from spherical to ellipsoidal) and a low polidispersity, with diameter from 15 nm to 40 nm (Figure 1.13). Suspensions remain limpid and uniform and no micro-aggregates or residual powders are detectable on the sample to the naked eyes even after some weeks.

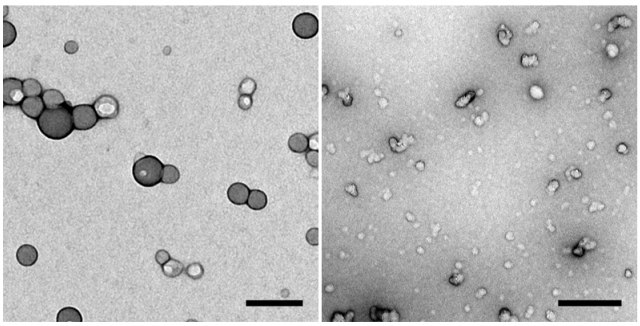

*Figure 1.13: Observation by TEM of the particles of **T3** (left) and **T4** (right) freshly prepared. Scale bar = 150 nm.*

### 1.4.2 Thiophene-based derivatives

Two thiophene-based derivatives (called **TP1** and **TP2**)[2] have been tested for the preparation of organic nanoparticles (Figure 1.14). These molecules show a very interesting phenomenon in the solid state known as aggregation-induced emission (AIE).

In general the fluorescence efficiency of organic chromophores, especially those with aromatic rings in disc-like shape, decreases in the solid state, as a result of π-π stacking interaction, even though they show high fluorescence efficiency in solution. The excited states of the aggregates often decay via non-radiative pathways, which is known as aggregation-caused quenching (ACQ) of light emission in condensed phase. In 2001 Tang's group discovered a series of silole molecules that were non-luminescent in the solution state, but emissive in the aggregate state (as nanoparticles suspensions in poor solvents or as thin films in the solid state) [42]. The mechanistic cause for the AIE effect can be ascribed to the restriction of conformational degrees of freedom of the molecule in solid-state compared to the solution: the physical

[2]**TP1** was synthesized by G. Barbarella's group, Università di Bologna; **TP2** was synthesized by M. Blanchard-Desce's group.

constraint blocks the non-radiative path and activates the radiative decay [44]. Recently, some works on molecules that show AIE have been reported [45, 46, 47], but to the best of our knowledge no work that involve the use of thiophene derivatives to prepare AIE-nanoparticles has been reported yet. Barbarella et al. published some studies on thiophene derivatives in solution and thin films, but not for their nanoparticles [48].

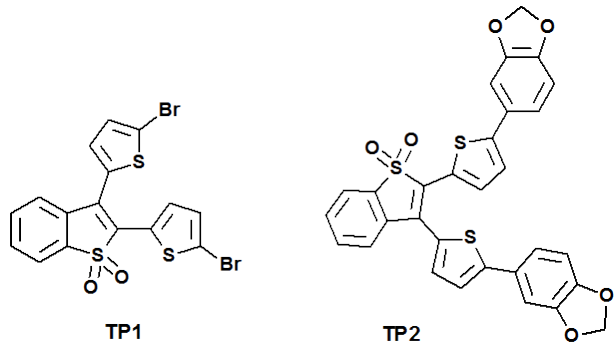


*Figure 1.14: Molecular structure of thiophene-based chromophores used for the preparation of nanoparticle suspensions.*

#### 1.4.2.1 TP1 and TP2 Nanoparticle Suspensions

**Preparation**

Stock solutions of **TP1** and **TP2** (1 mM) are prepared in THF. An aliquot of these solutions is added to a known amount of water under vigorous stirring to achieve a final nominal concentration of $2 \times 10^{-5}$M for both compounds. The proportion of THF in water is 2% v/v. The solutions are kept under stirring for 30 minutes to complete the reprecipitation process.

**Spectroscopic Characteristics of Suspensions**

The absorption spectra of the FON suspensions show an intense absorption band peaking around 380 nm for **TP1** and 430 nm for **TP2**. The

absorption spectra of both **TP1** and **TP2** nanoparticles are quite similar to those of **TP1** and **TP2** molecules dissolved in organic solvents, but broader (Figure1.15, left panel). The fluorescence of **TP1** and **TP2** dissolved in organic solvents is very weak (fluorescence quantum yield $< 1\%$, see Table 1.4; emission of **TP1** is too weak to be detected), while the fluorescence signal drastically increases for FON suspensions, yielding a quantum yield of 0.20 and 0.14 for **TP1** FONs and **TP2** FONs respectively, which is a clear evidence of the aggregation-induced emission phenomenon. The emission maximum of **TP1** FONs falls in the green spectral region while **TP2** FONs show an orange emission (Figure 1.15, right panel).

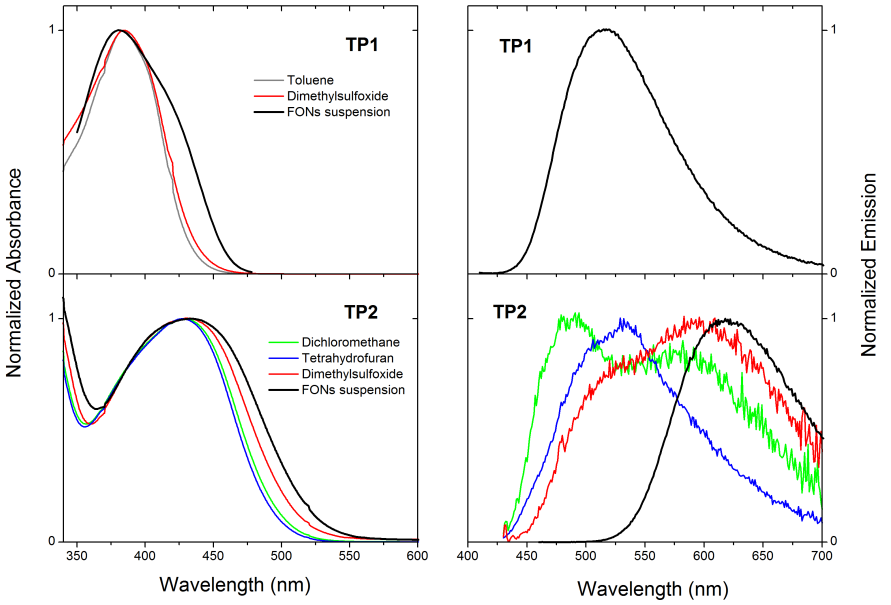


*Figure 1.15: Absorption (left) and emission (right) spectra of **TP1** and **TP2** solutions in organic solvents and their FON suspension.*

*Table 1.4: Spectroscopic properties of **TP1** and **TP2** in different solvents and of FONs in aqueous suspensions.*

| | Solvent | $\lambda_{abs}^{max}$ [nm] | $\lambda_{em}^{max}$ [nm] | ε [$\times 10^4$ $M^{-1}cm^{-1}$] | $\Phi^a$ |
|---|---|---|---|---|---|
| **TP1** | Toluene | 384 | 524 | - | <0.01 |
| | Dimethylsulfoxide | 385 | 520 | - | <0.01 |
| | FONs | 382 | 515 | - | 0.20[b] |
| **TP2** | Dichloromethane | 428 | 490 | - | <0.01 |
| | Tetrahydrofuran | 428 | 533 | 1.87 | <0.01 |
| | Dimethylsulfoxide | 433 | 590 | - | <0.01 |
| | FONs | 434 | 615 | - | 0.14[b] |

*[a] Fluorescence quantum yield estimated using Fluorescein as reference ($\phi = 0.90$). [b] Fluorescence quantum yield measured using an integrating sphere in center-mount sample holder configuration.*

### Morphological Characteristics of Nanoparticles

**TP1** FONs have been observed by TEM (Figure 1.16). Nanoparticles are quite spherical in shape and weakly polydispersed, with a diameter from about 15 nm to 40 nm

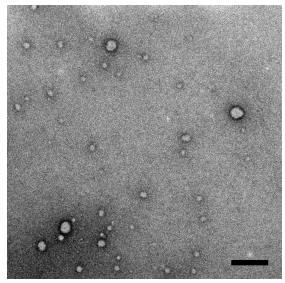

*Figure 1.16: Observation by TEM of freshly-prepared **TP1** nanoparticles. Scale bar = 150 nm.*

### 1.4.3 Bodipy derivatives

Bodipy dyes are typically strongly UV-absorbing small molecules, that emit relatively sharp fluorescence peaks with high quantum yields. They are relatively insensitive to the polarity and to the pH of their environment and are reasonably stable under physiological conditions. Small modifications to their structures enable tuning of their fluorescence characteristics; consequently, these dyes are widely used to label proteins and DNA [49]. In general, the apolar bodipy dyes form H- or J-aggregates due to facile stacking of the electron-rich dipyrromethene core. In H-aggregates, the bodipy planes stack in parallel to give essentially nonfluorescent structures featuring a blue-shifted absorption profile. In the J-aggregates, the transition dipoles are not parallel but aligned on the same plane. Such aggregates or dimers are weakly fluorescent and usually exhibit a red-shifted absorption spectrum [50]. Fluorescence of molecular micro and nanocrystals (particles size from 100 nm to 650 nm) prepared with BODIPY derivatives are reported in Ref. [51]. In that work the authors focus their attention on Trimesitybodipy (TMB) and Mesitybodipy (**MB**, structure in Figure 1.17) and evidence the formation of fluorescent excimers in crystalline TMB. Their nanocrystals are prepared in sol-gel thin film.

In this section a study of nanoparticles of **MB** prepared by the reprecipitation method is reported.

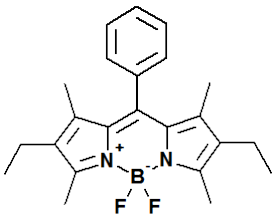


**MB**

*Figure 1.17: Molecular structure of the bodipy chromophore (**MB**) used for the preparation of nanoparticle suspensions.*

#### 1.4.3.1 MB Nanoparticle Suspension

**Preparation**

**MB** FONs are prepared by reprecipitation by adding 300 µL of a 1 mM THF solution of **MB** to a 14.700 mL of water under stirring to achieve a final nominal concentration of $2 \times 10^{-5}$M (2% v/v THF/$H_2O$). The suspension is kept under constant stirring for 1.5 hours. Nanoparticles are also prepared in 4% v/v THF/$H_2O$ and 10% v/v THF/$H_2O$ to evaluate the effect of the possible partial solubilisation of molecules in THF/$H_2O$ at the same final concentration mixtures. All the obtained suspensions are pink and limpid to the naked eyes.

**Spectroscopic Characteristics of Suspensions**

The spectroscopic behavior of **MB** in ethanol and chloroform is reported in Ref. [52]. Here we describe the spectroscopic behavior of **MB** suspensions in 2%, 4% and 10% v/v THF/$H_2O$.

Regardless of the clearness of the solution to the naked eyes, scattering is clearly recognizable in the absorption spectrum measured with UV-Vis spectrophotometer (see Figure 1.18) but not in the absorption spectrum measured with a spectrofluorimeter equipped with integrating sphere, because

of the particular geometry of detection that avoid the scattering signal from the sample. The main absorption band of **MB** displays a hypochromic effect and a spectral broadening compared to that of the dye dissolved in THF, while the absorption maximum is red-shifted of about 20 nm (from 524 nm to 544 nm) with respect to the maximum in THF. The phenomenon of scattering is probably caused by the presence of aggregates of approximately hundreds nanometer of size in suspension.

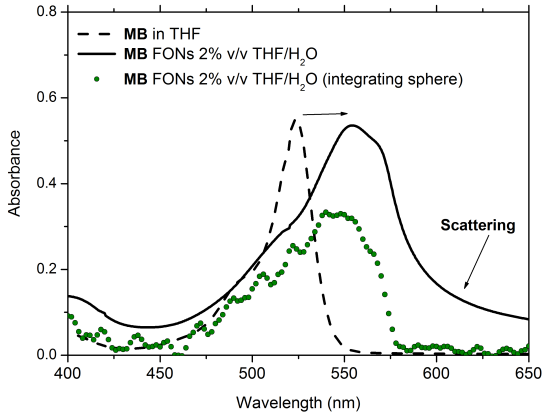


*Figure 1.18: Absorption spectra of **MB** dissolved in THF (dashed black line) and **MB** FONs measured with UV-Vis spectrophotometer (solid black line) and with integrating sphere (green circles).*

Regarding fluorescence properties, the emission spectrum of **MB** dissolved in THF shows a maximum at 544 nm and the emission spectrum of solid state is characterized by a maximum at 628 nm and two shoulders at about 590 nm and 700 nm respectively. The peak at about 630 nm has been attributed to the presence of J aggregates or excimers [53]. The shape of emission spectra of FON suspensions depends on the THF/H2O ratio. In THF/H2O 2% v/v or 4% v/v, fluorescence spectra show three well resolved peaks (540 nm, 570 nm and 625 nm), in THF/H2O 10% v/v there is a domi-

nant peak at 544 nm and the other two peaks are less intense and broadened. The interpretation of the suspension spectra is quite hard: the peak at 625 nm corresponds to the maximum of emission of the solid state and it could indicate the presence of nanoparticles/nanoaggregates or polycrystalline materials, while the peak at 540 nm corresponds to the maximum emission of **MB** in THF and it could indicate the presence of molecules dissolved in solution (this is indeed the main peak for 10% v/v THF/$H_2O$ system).

The suspension of **MB** FONs in 10% v/v THF/$H_2O$ after one day is cloudy to the naked eyes, while the other suspensions are still limpid. To evaluate the hypothesis of partial dissolution of **MB** molecules or the presence of aggregates, the emission spectrum has been registered before and after filtration. From a spectroscopic point of view the 10% (v/v) sample shows a growth of the two bands at 570 nm and 620 nm, together with a blue-shift of the main peak of about 15 nm (Figure 1.20). If this solution is filtered with 0.2 μm PTFE filter a very pale solution (almost colorless) is obtained. The emission spectrum of the filtered solution has only one peak (525 nm) and it is very similar in shape to the emission spectrum in THF, but blue-shifted of about 25 nm.

Badré et al. in Ref. [51] obtained similar results for nanocrystals of **TMB** in sol-gel films: nanocrystals have about the same spectrum as **TMB** dissolved in dichloromethane (but red-shifted of 50 nm) and they attributed the emission spectrum to the presence of J-aggregates. In our case the peaks at 570 and 630 nm could also be attributed to aggregates. It could also be possible that some different crystalline forms are present in this type of nanoparticles.

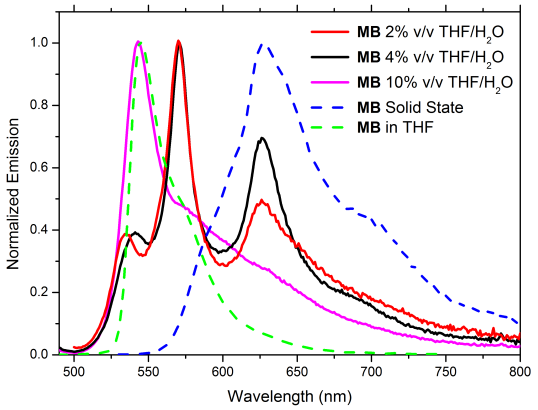


*Figure 1.19: Emission spectra of **MB** dissolved in THF (dashed green line), **MB** solid state (dashed blue line) and freshly-prepared **MB** nanoparticle suspensions with different $THF/H_2O$ ratio.*

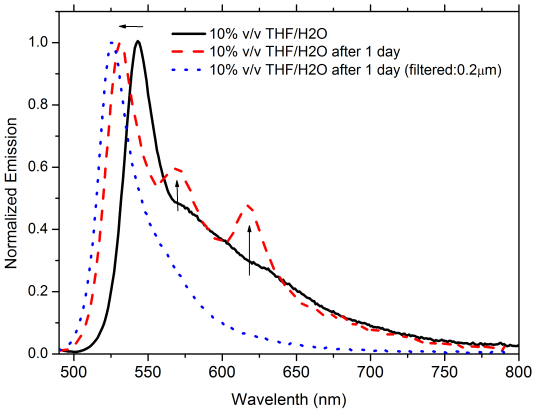


*Figure 1.20: Emission spectra of 10% v/v **MB** $THF/H_2O$ FONs suspension after the reprecipitation process (solid black line), after one day (dashed red line) and after one day and filtration with 0.2 μm filter (dotted blue line).*

### 1.4.4 Commercial Chromophores: Nilered and DCM

**Nilered** and **DCM** (structures in Figure 1.21) are two commercial compounds widely used as laser dyes in the orange-red region [54, 55, 56, 57]. **Nilered** is also used in biological applications as lipid probe [58, 59], protein label [60, 61] and membrane and micelles probe [62, 63, 64]. **DCM** is fluorescent at the solid state, while **Nilered** is only weakly fluorescent at the solid state. Both compounds are insoluble in water, so we tested the possibility to obtain their nanoparticles in aqueous suspension.

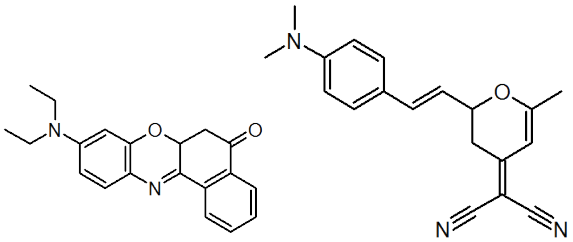


*Figure 1.21: Molecular structure of **Nilered** (left) and **DCM** (right).*

#### 1.4.4.1 Nilered and DCM Suspensions

**Preparation**

Nanoparticles of **Nilered** and **DCM** are prepared by the reprecipitation method by adding 150 µL of a 1 mM THF stock solution of the selected dye to 14.850 mL of water under vigorous stirring to achieve a final nominal concentration of $1 \times 10^{-5}$M (2% v/v THF/$H_2O$). Few minutes after injection the solution becomes more and more colorless for both compounds and after about one hour some micro-aggregates are visible to the naked eyes.

**Spectroscopic Characteristics of the Suspensions**

The evolution of UV-Vis spectra of **Nilered** and **DCM** suspensions (Figure 1.22) supports the formation of large aggregates through a very marked

hypochromic effect: the absorption extinction coefficient of both suspensions decreases during time and after 30 minutes is almost zero. The dyes aggregate and precipitate in few minutes. So it can be concluded that it is not possible to obtain stable suspensions from **Nilered** or **DCM** using the simple precipitation method.

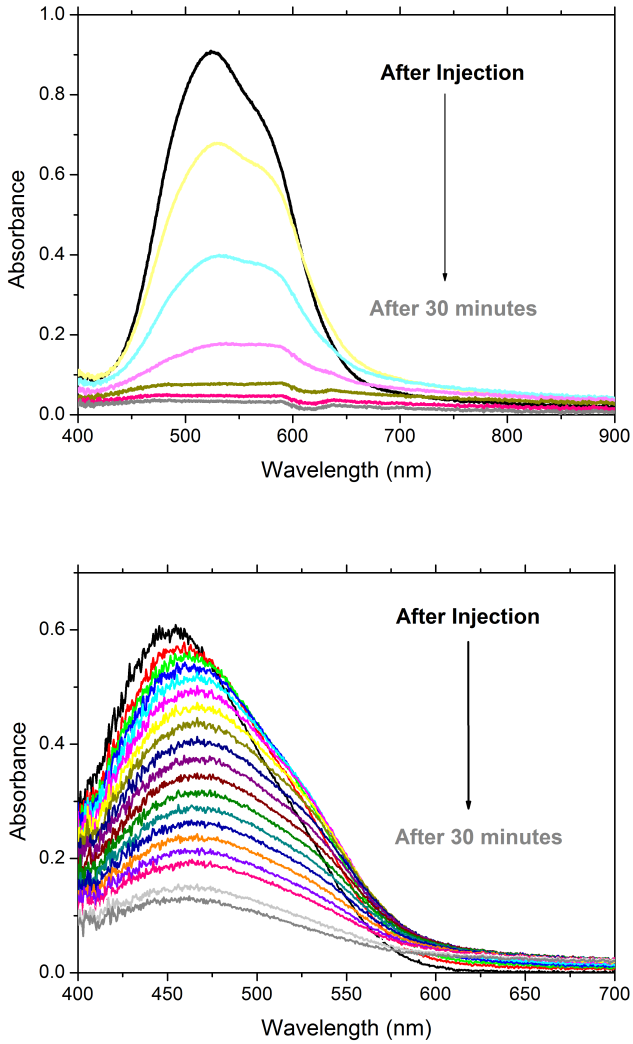


*Figure 1.22: Evolution of the UV-Vis absorption spectrum of* ***Nilered*** *(top) and* ***DCM*** *(bottom) during the reprecipitation process. The great hypochromic effect is due to the formation and precipitation of micro-aggregates, also visible to the naked eyes.*

## 1.5 Conclusions

In general, combining theory and empirical observations it is possible to define some basic rules that can help to obtain fluorescent organic nanosuspensions in water:

- The chromophores must be fluorescent at the solid state to have a good probability to obtain fluorescent nanoparticles.
- The chromophores must be as insoluble as possible in water and soluble in organic solvents (for example THF) to assure high supersaturation level and, consequently, the success of the reprecipitation process.
- The optimal concentration of chromophores in the final suspension is experimentally found to be on the order of $10^{-5}$M.

Even if all of these rules are followed during the preparation of the nanoparticles this does not grant the colloidal stability of the suspensions. From an empirical point of view it has been observed that some chromophores yield stable nanosuspensions, while other chromophores with similar structures yield unstable systems. For example, the two triphenylamine-based compounds **T1** and **T3** have very similar structures, but **T1** FONs are less stable during time than **T3** FONs. The stability can be evaluated by the direct observation of the suspensions to the naked eyes and/or by spectroscopic and morphological characterizations. It has been observed that **T1** suspensions become more and more colorless during time and some microaggregates appear after some weeks, while **T3** nanosuspensions always preserve the same color and no aggregates are detectable to the naked eyes. It is quite difficult to explain the reasons of these two different behaviors. Probably the nanoparticles have different zeta-potentials, i.e. different charges at the surfaces; in particular it could be expected that **T3** nanoparticles have higher zeta-potential than **T1** nanoparticles (this is reasonable because of the different polarizability of the two molecules) so that electrostatic repul-

sion forces could be responsible for the absence of aggregation phenomena for **T3** nanoparticles.

However, the polarizability of the molecule cannot be the only parameter to explain the stability of nanosuspensions: **Nilered** and **DCM**, for example, are highly-polarizable chromophores so in principle they could give nanoparticles with high zeta-potential, but in fact during the reprecipitation process nanoparticles aggregate and precipitate. In this case the geometry of the molecule (essentially planar for both compounds) may play a role in the packing inside the nanostructure and, consequently, on the surface properties and colloidal stability.

In conclusion there are plenty of parameters that could affect the aggregation: molecular structure, polarizability, solubility in water, temperature, concentration and it is almost impossible to found safe general rules to obtain stable nanoparticles in water. Unfortunately for these systems the only method to evaluate the colloidal stability is still "trial and error".

# Chapter 2

# Fluorescent Organic Nanoparticles as Biphotonic Probes

## 2.1 Two-Photon Microscopy

The invention of two-photon-excited fluorescence (TPEF) light microscopy by Denk, Webb and co-workers [65] revolutionized three-dimensional (3D) *in vivo* imaging of cells and tissues. In 1931, the theoretical basis of two-photon excitation was established by Maria Göppert Mayer, but this photophysical effect was verified experimentally by Kaiser and Garret only in 1963. Two-photon-excited fluorescence is a fluorescence emission process induced in a fluorophore by the simultaneous absorption of two photons (Figure 2.1). The familiar one-photon-excited fluorescence process involves the excitation of a fluorophore from the electronic ground state to an excited state by a single photon. This process typically requires photons in the ultraviolet or blue/green spectral range. However, the same excitation process can be stimulated by the simultaneous absorption of two less energetic photons (typically in the infrared spectral range) under sufficiently

intense laser illumination. This nonlinear process can occur if the sum of the energies of the two photons corresponds to the energy gap between the molecule's ground and excited states. Since this process depends on the simultaneous absorption of two photons, the probability of two-photon absorption by a molecule is a quadratic function of the excitation radiance (see Appendix 2). Under sufficiently intense excitation, three-photon and higher multi-photon excitation is also possible [66]. The nonlinear excitation process provides a number of distinct advantages compared to the conventional one-photon excitation microscopy. To begin with, the high incident photon density necessary for sample excitation limits the excitation volume to the focal spot. Appreciable two-photon fluorescence occurs only at the microscope focal volume, where the photon density is high; negligible fluorescence is excited outside of this volume. As a result, confocal-like 3D resolution (i.e. submicrometer) can be achieved without the use of confocal apertures. In addition, the limited focal volume limits sample photobleaching to the focal spot. This feature allows prolonged biological imaging to be achieved. Furthermore, the low-frequency photons (typically in the NIR) used for sample excitation are absorbed and scattered less by tissue components than the photons that would be required for linear excitation. As a result, imaging using multiphoton microscopy can achieve greater penetration depths than one-photon microscopy [67]. Furthermore, the use of biphotonic probes with large two-photon absorption action cross section allows a great selectivity. In bioimaging applications, multiphoton microscopy has been successfully applied to areas such as neurobiology, developmental biology, and tissue imaging [68, 69, 70]. A critical component in a two-photon microscope is its light source; a high-radiance light source is required for efficient excitation. Two-photon microscopy based on continuous-wave lasers has been demonstrated. However, the high average laser power is a concern for pigmented biological samples with appreciable one-photon absorption. High repetition rate (100 MHz), ultrafast (femtosecond or picosecond pulse widths) lasers, such as titanium–sapphire and Nd:YLF lasers, are the most widely used

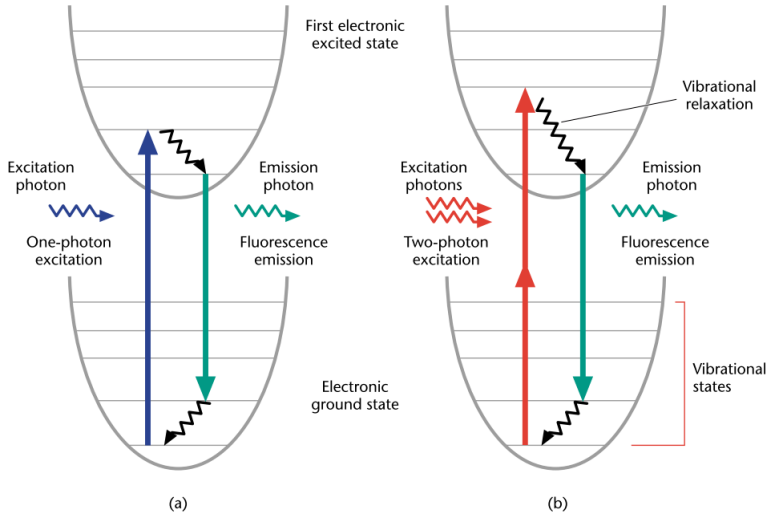


*Figure 2.1: Jablonski diagram of one-photon (a) and two-photon (b) excitation, which occurs as fluorophores are excited from the ground state to the first electronic states. One-photon excitation occurs via the absorption of a single photon. Two-photon excitation occurs via the simultaneous absorption of two lower-energy photons. After either excitation process, the fluorophore relaxes to the lowest energy level of the first excited electronic state via non-radiative path. The subsequent fluorescence emission process proceeds in the same way in both cases [66].*

light sources. The high peak power and the low duty cycle of these lasers minimize average power deposition in the specimen while maximizing two-photon excitation efficiency.

### 2.1.1 *In Vivo* Imaging

*In vivo* microscopy (bioimaging) is a powerful method for studying fundamental issues of physiology and pathophysiology. The recent development of multiphoton fluorescence microscopy has extended the reach of *in vivo* microscopy, supporting high-resolution imaging deep into the tissues and organs of living animals. As compared with other *in vivo* imaging techniques, multiphoton microscopy is uniquely capable of providing a window into cellular and subcellular processes in the context of the intact, functioning animal. While the volume of tissue that can be imaged by *in vivo* fluorescence microscopy is not as large as that obtained by conventional *in vivo* imaging methods, the capability of this technique to provide images in living animals at subcellular resolution in 1 second or less is a unique advantage. Furthermore, the simultaneous imaging of multiple fluorophores makes fluorescence microscopy uniquely capable of multiparameter imaging, supporting powerful correlative analysis. Additionally, similar to the conventional forms of *in vivo* imaging, *in vivo* fluorescence microscopy can be used to image an animal longitudinally (i.e. before and after an intervention), which enables the collection of within-animal control data and reduces the number of animals needed for a given analysis. This technique is capable of collecting high-resolution (0.4 μm) fluorescence images hundreds of μm into tissues (Figure 2.2). In addition to providing better penetration and resolution than traditional methods of microscopy (Figure 2.3), the use of infrared light also makes multiphoton microscopy significantly less toxic. For the capability of collecting fluorescence images of living animals at a subcellular resolution, *in vivo* multiphoton microscopy has revolutionized the way biomedical researchers can study physiology, pathophysiology, and drug action [71].

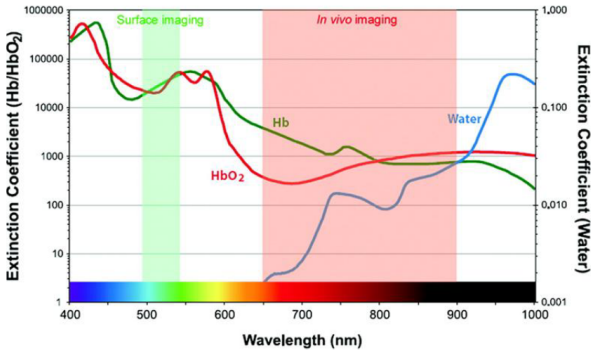


*Figure 2.2: Definition of the optical window for in vivo imaging [65].*

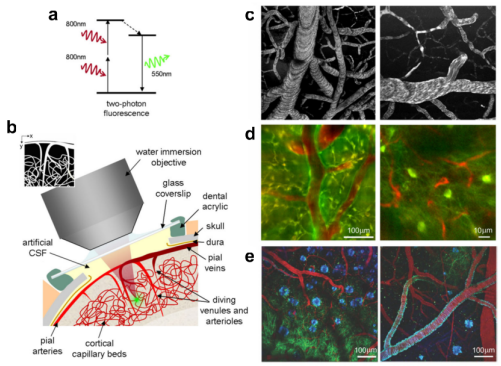


*Figure 2.3: Two-photon microscopy of in vivo brain function. (a) Basic mechanism of two-photon fluorescence. (b) Schematic of surgical preparation of exposed cortex, with sealed glass window and microscope objective positioning. Green dot shows location of two-photon fluorescence. (c) Examples of two-photon maps of the vasculature following intravenous injection of dextran-conjugated fluorescein. Black dots and stripes show red blood cell motion. (d) Dual-channel imaging of neuronal (green) and vascular (red) signals: (left) Oregon Green 488 BAPTA-1 AM calcium sensitive dye stained neurons and (right) transgenic mouse expressing green fluorescent protein (GFP) in a subpopulation of neurons. Texas dextran red is the intravascular tracer in both cases. (e) Three channel imaging of Tg2576 APP Alzheimer's disease mouse model with amyloid-targeting dye (blue), GFP expressing neurons and dendrites (green) and vasculature (red). From [76].*

## 2.2 Biphotonic Probes

It is now well recognized that TPEF (or "biphotonic") probes offer distinct advantages with respect to classical fluorescent probes [72, 73, 74, 75]. There are several properties of a successful optical probe for multiphoton *in vivo* imaging including emission wavelength, brightness, two-photon absorption cross section, bio- and photo-stability. The emission wavelength and brightness are important parameters for biological applications of TPEF: red or near-infrared emitting probes assure the detection of fluorescence signal through biological tissues, such as skin. Probes with high two-photon absorption cross section assure high sensitivity to the method because endogenous molecules in tissues typically do not naturally have large TPA cross section and, consequently, they present negligible fluorescence signals compared to ad-hoc designed biphotonic probes.

In particular, biphotonic nanoprobes can be divided in two main categories: those based on organic nanoparticles and those based on inorganic nanocrystals such as semiconductiong quantum dots or silica nanoparticles.

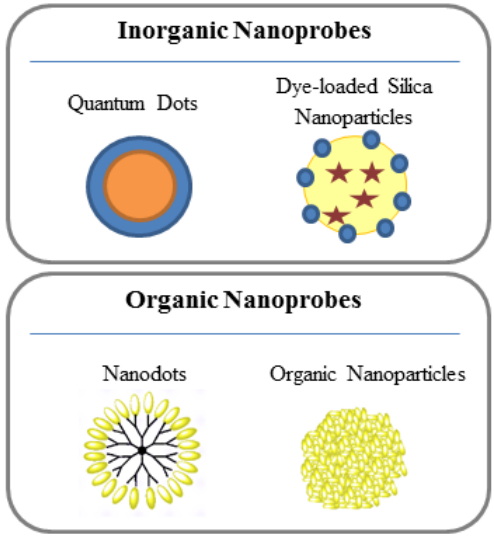


*Figure 2.4: Schematic structures of fluorescent nanoprobes. Inorganic nanoprobes are quantum dots or dye-loaded silica nanoparticles (top panel). Organic nanoprobes can be divided into two main families: nanodots and organic nanoparticles (bottom panel). Other types of organic nanoparticles include dye-loaded polymer-based and dye-loaded lipid-based nanoparticles.*

### 2.2.1 Quantum Dots

Quantum dots are inorganic nanocrystals whose excitation and emission is fundamentally different than traditional organic fluorophores. Instead of electronic transitions from one valence orbital to another, quantum-dot fluorescence involves exciting an electron from the bulk valence band of the semiconductor material across an energy gap, making it a conduction electron and leaving behind a hole. The electron–hole pair (also known as an exciton) is quantum-confined by the small size of the nanocrystal. When the electron–hole pair eventually recombines, a characteristic photon is emitted. Minute changes to the size of the confining crystal alter the energy bandgap, thus determining the color of the fluorescence photon. In general, the smaller

the quantum dot, the larger the bandgap energy for a given material, and thus, the shorter the wavelength of the emitted fluorescence. Of the many types of quantum dots that can be made from various semiconductor materials, CdSe/ZnS quantum dots are presently the most common commercially available. They are composed of a core of cadmium selenide (ranging from about 10 to 50 nm in diameter and about 100 to 100,000 atoms in total). Covered by a thin zinc sulfide passivating layer that improves the fluorescence quantum efficiency and stability of the quantum dots and an organic polymer coating to make them water soluble and enabling bioconjugation. They exhibit high fluorescence quantum yield and, as would be expected from a solid-state material, they are extremely resistant to reactive oxygen-mediated photobleaching. They typically have large absorption cross-sections and broad absorption spectra with narrow band fluorescence emission that can be tuned over a broad range from blue to near-infrared (Figure 2.5).

Quantum dots offer several advantages as biphotonic probes such as high brightness, robustness and tunable emission, however many quantum dot core compositions include toxic elements such as cadmium, arsenic or lead and this clearly constitutes an obstacle for their translation to clinics. Therefore, even if studies demonstrated the possibility to passively or actively address the particles to tumor sites [77, 78, 79], their future use in tumor diagnostics in clinics seems compromised.

*Figure 2.5: Micromolar aqueous suspensions of 525, 565, 585, 605, and 655 quantum dots (left to right) under UV illumination.*

### 2.2.2 Dye-loaded Silica Nanoparticles

Other inorganic probes have been proposed as fluorescent nanotracers, relying on the encapsulation or surface binding of organic fluorescent dyes to inorganic nanoparticles, mainly silica, calcium phosphate oxide or gold nanoparticles. Because of the absence of toxic heavy metal constituents, silicon nanoparticles are perceived to be less toxic than the commonly used cadmium-based QDs. However, they have not been frequently used in bioimaging applications because of the complex problem of making them optically and colloidally stable in biological media. The C-dots developed at Cornell University [80] are certainly among the most described silica nanoprobes as they entered clinical trials in Fall 2011 for lymph node diagnosis and staging in advanced melanoma. Silica is an interesting material for the design of functional nano-objects: active molecules can be encapsulated inside the pores of the matrix, or the use of organic modified silanes can allow their covalent attachment in the core or the shell of the particles. Synthesis protocols such as the Stöber's process are well mastered and easy to implement [81]. The optical properties of the dyes such as cyanines are well preserved and even enhanced in the silica matrix. Similarly to quantum dots, very small nanocrystals ($<$10 nm) seem to undergo urinary excretion, whereas larger nanoparticles ($>$20 nm) rather distribute in liver, spleen, stomach and undergo hepatobiliary excretion [82].

### 2.2.3 Fully-Organic Probes

At first, TPEF was developed using conventional fluorophores whose two-photon absorption (TPA) characteristics were not optimized, but it was soon realized that molecules specifically engineered for TPEF can significantly outperform standard fluorophores One-photon and two-photon excitation are fundamentally different quantum-mechanical processes and have different selection rules. A fluorophore's two-photon excitation spectrum scaled

to half the wavelength is typically not equivalent to its one-photon excitation spectrum. However, a fluorophore's emission spectrum, in the absence of ground-state heterogeneity, is independent of the excitation mechanism, since the molecule relaxes to the same excited state through vibrational mechanisms before emission. Since two-photon spectra of many molecules can be significantly different from their scaled one-photon equivalent, it is important to characterize the spectral properties of fluorophores under two-photon excitation. The goal is to search for fluorophores combining a high fluorescence quantum yield ($\Phi$) and a high TPA cross section ($\sigma_2$) in the spectral region of interest for bioimaging. Molecular engineering of optimized chromophores with large TPEF cross-sections has been particularly active in the last decade [83, 84, 85]. More recently, different types of organic architectures have been conceived for maximizing fluorescence quantum yield and TPA cross section, such as nanodots and organic nanoparticles.

#### 2.2.3.1 Nanodots

A "soft" and biocompatible alternative to quantum dots is represented by so-called nanodots. These objects can be obtained by grafting a different number of two-photon fluorophores on the surface of a dendrimeric platform (Figure 2.6, top and middle panels) and they offer several potential advantages: photoluminescence characteristics can, in principle, be tuned by playing on the nature of the fluorophore, while the dendrimer scaffold can be chosen so as to minimize toxicity effects and control clearance ability. However, implementing a modular approach also requires taking into account interactions between the various molecular building blocks including possible interactions between decorating fluorophores. The confinement of fluorophores within the nanodots imposes close proximity between chromophores which favors interchromophoric interactions: (i) in the ground state with potential effects on the absorption characteristics and (ii) in the excited state with marked effects on fluorescence. Such interactions can sig-

nificantly affect the optical responses and photophysical properties of the nanodots which will then differ from the mere addition of the contributions of isolated fluorophores. Also it has been shown that interactions between chromophores within dimers or aggregates can lead to significant change in TPA responses (Figure 2.6, bottom panel). Such effects are expected to be strongly dependent on the nature of the chromophores, their proximity and relative orientations. In this respect the geometry and symmetry of the dendritic scaffold are expected to play an important role [86]. Nanodots showing competitive two-photon brightness, comparable to the highest reported for QDs, have been reported [87].

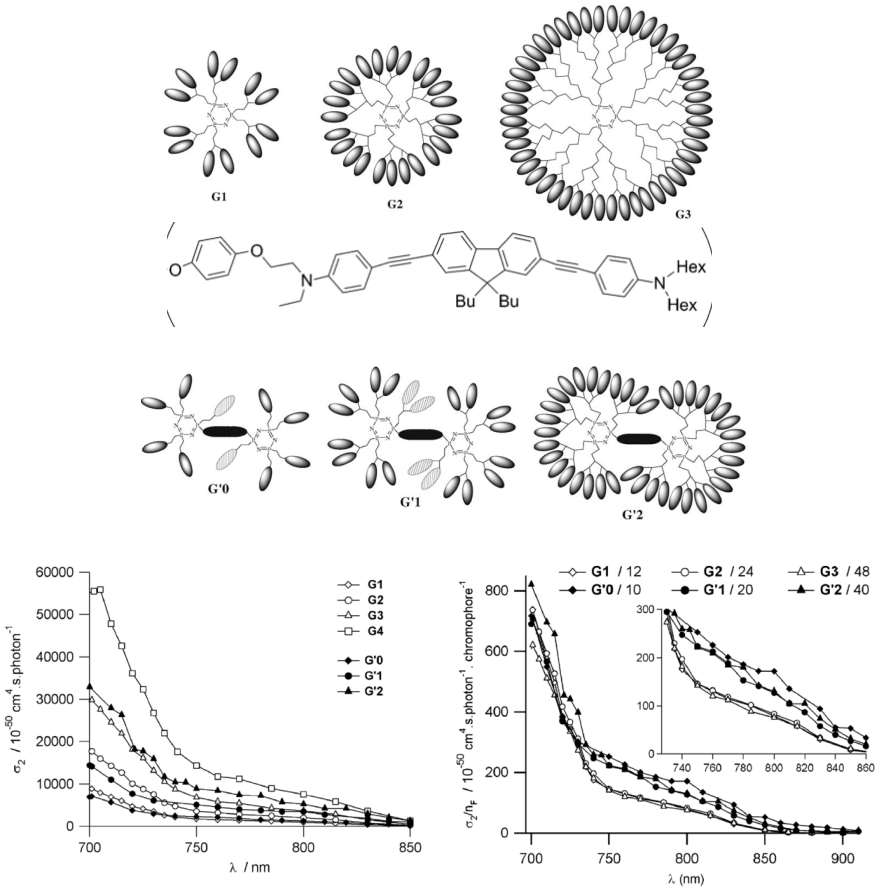


*Figure 2.6: Schematic representation of homochromophoric spherical-type organic nanodots and structure of chromophore (top panel); schematic representation of heterochromophoric dumbbell-like organic nanodots (middle panel); two-photon absorption spectra of G1–G3 and G'0–G'2 dendrimers determined by femtosecond TPEF measurements in toluene (bottom left panel), comparison of the TPA efficiency (normalized by the number of TP fluorophores per nanodot) of nanodots (bottom right panel). From [86].*

#### 2.2.3.2 Organic Nanoparticles

It can be sought that using nanoaggregates or nanocrystals of organic compounds as TPEF probes shall result in new properties, compared to those of the dissolved dyes. For instance, better chemical and photochemical stability can be expected [88]. Moreover, little is known about the behavior of TPEF probes in the solid state and unattended spectroscopic properties can arise, making these nanoparticles particularly useful for subsequent applications. In very recent works organic nanoparticles prepared with different chromophores have been tested for *in vivo* bioimaging. An example of use of organic nanoparticles for detection of tumor site on a mouse is reported in Figure 2.7 [89].

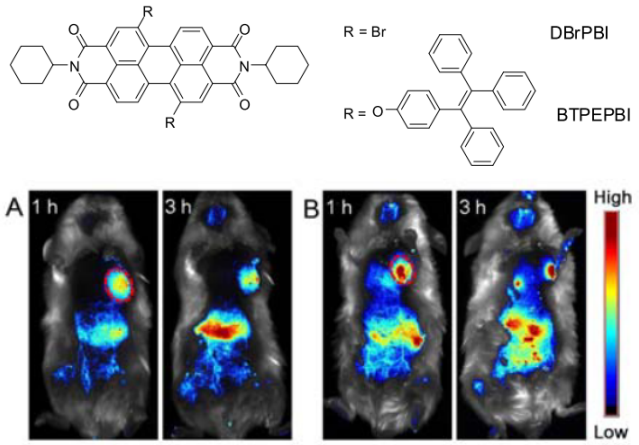


*Figure 2.7: Chemical structure of molecules used for the preparation of organic nanoparticles (top); in vivo imaging of H22 tumor-bearing mice after intravenous injection of organic nanoparticles (bottom). The red circle indicates the tumor site [89].*

## 2.3 Two-Photon Excitation Fluorescence of Triphenylamine-based Organic Nanoparticles

Whatever the excitation process, it is well established that the fluorescence efficiency of solid-state organic compounds is closely related to the various intermolecular interactions that take place in aggregates, or in crystals [90, 91]. In particular, organic dye molecules generally comprise an electron-rich group (D) and an electron-withdrawing group (A) linked through a π-conjugated system. Crystallization of such D-A molecules usually leads to the (centrosymmetric) assembly along the direction of dipole-dipole interaction with the aid of π-π stacking, resulting in strong fluorescence quenching in the solid state. Fortunately, it has been demonstrated that the non-planar propeller-shaped triphenylamine could avoid π-π stacking and facilitate emission in the solid state [92]. That is one of the prime reasons why organic molecular materials based on triphenylamine have been exploited promisingly for application in electroluminescent devices, solid-state lasers, field-effect transistors and nonlinear optical devices. In Chapter 1 (1.4.1) the description of preparation and linear spectroscopic characterization of nanoparticles from two triphenilamine-based chromophores **T1** and **T2** were reported (for molecular structures see also Appendix 1). In this section the study of these nanoparticles used as biphotonic probes is reported [17].

Due to the good fluorescence quantum yield of **T1** and **T2** suspensions, their two-photon excitation fluorescence (TPEF) is investigated. After the formation of nanoaggregates in water/THF mixture, the particle suspensions are subjected to two-photon excitation using the set-up described in Appendix 2. This measurement gives the TPEF action cross section $\sigma_2\Phi$, at different excitation wavelengths, then easily follows the corresponding two-photon absorption (TPA) cross section, $\sigma_2$. For comparison, the TPA spectra of chromophores **T1** and **T2** dissolved in organic solvents of various polarity are also determined.

As shown in Figure 2.8, chromophores **T1** and **T2** exhibit significant

two-photon absorption responses in the whole 700-900 nm region. While **T1** shows TPA maximum between 820 and 830 nm (corresponding to the lowest-energy excited state which is both one- and two-photon allowed), **T2** exhibits a sharp maximum in the 720-730 nm range, arising from the transition to the two-photon allowed (but one-photon forbidden) higher excited state. In addition, a second, less intense maximum is observed around 825 nm, corresponding to the transition to the lowest excited state (both one- and two-photon allowed). The TPA responses of chromophores **T1** and **T2** in solution are strongly dependent on the solvent characteristics (Table 2.1).

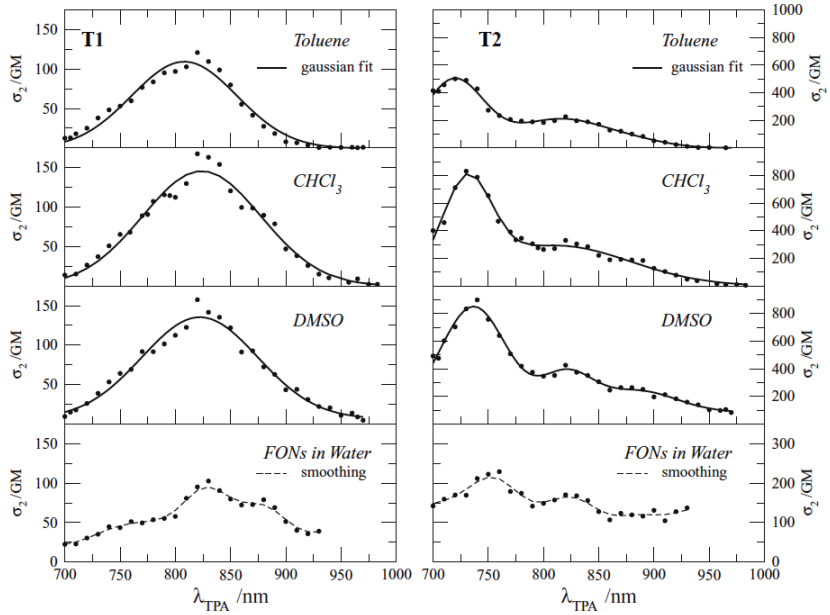


*Figure 2.8: TPA spectra for **T1** (left) and **T2** (right) in toluene, chloroform, dimethylsulfoxide, and FONs in water (from top to bottom). The bold lines indicate the (multi)Gaussian fit and the dashed lines the mean curve of the data points (●). 1 GM = $10^{-50} cm^4 s\, photon^{-1}$. From [17].*

*Table 2.1: Two-photon excitation characteristics of **T1** and **T2** dissolved in different solvents and of their FONs in aqueous suspensions after reprecipitation process in water/THF 98:2 v/v.*

| | Solvent | $\lambda_{TPA}^{max}$ [nm] | $\sigma_2^{max}$ [GM] | $\sigma_2^{max}\Phi$ [GM] |
|---|---|---|---|---|
| T1 | Toluene | 820 | 121 | 107 |
| | Chloroform | 820 | 167 | 137 |
| | Dimethylsulfoxide | 820 | 157 | 39 |
| | FONs | 827 | 100 | 15 |
| T2 | Toluene | 720, 820 | 501, 235 | 341, 160 |
| | Chloroform | 730, 820 | 832, 330 | 524, 208 |
| | Dimethylsulfoxide | 740, 820 | 899, 440 | 90, 44 |
| | FONs | 760, 825 | 230, 170 | 4.6, 3.4 |

In the case of dipolar chromophore **T1**, a broadening and increase in TPA on the red edge of the band are observed (in agreement with inhomogeneous broadening) as well as a 30% increase of the TPA peak intensity on going from apolar toluene to medium-polarity chloroform or high-polarity DMSO. Octupolar chromophore **T2** also shows a broadening of the TPA spectrum as well as a bathochromic and hyperchromic shift of the strongest TPA band with increasing solvent polarity.

Whereas the positions of the TPA maxima are only weakly affected as compared to isolated dyes in solution, the peak magnitudes and the shape of the TPA band(s) of **T1** and **T2** FONs are altered (Table 2.1). A marked broadening of the TPA bands and a decrease of the TPA peak magnitudes with respect to chromophoric molecules dissolved in organic solvents is observed (Figure 2.8). Such modifications of the TPA spectra can be related to through-space interactions between chromophores in the densely packed nanoaggregates. It has been shown earlier in simpler systems (i.e. dimers, trimers and dendrimers) that interchromophoric interactions between close

polar and polarizable chromophores could lead to TPA enhancement or reduction - as well as shift of the TPA band - depending on the relative orientations and distances between the chromophores [93, 94]. The situation is much more complex in this case due to the number of molecules and range of relative orientations/distances between interacting chromophores within the nanoaggregates. In addition, the variation in number of close chromophores (core versus peripheral chromophores in single organic nanoparticles) and possible distribution of relative orientations and distances between chromophores in nanoaggregates might explain the appearance of TPA subbands.

The maximum molecular TPEF action cross sections of **T1** and **T2** FONs, derived using the nominal dye concentration of $2 \times 10^{-5}$M, are found to be 15 and 5 GM, respectively (Table 2.1). This represents a significant reduction as compared to dyes dissolved in an apolar solvent and it results from the combined reduction of the TPA response and fluorescence quantum yield. The markedly different behavior of dyes **T1** and **T2** in nanoaggregates as compared to organic solutions shows that through-space interactions between chromophores in the FONs (depending on the molecular packing) strongly modify their spectroscopic properties. Such differences in the fluorescence and TPA properties have important implications with respect to the use of such nanoparticles in bioimaging.

From the average size of the nanoaggregates, as obtained from TEM, and the calculated density obtained from single-crystal X-ray diffraction studies (Figure 2.9), it is possible to calculate an estimation of the number of chromophores per nanoaggregate (see Table 2.2). The two-photon brightness per unit volume of **T1** and **T2** organic nanoparticles is comparable or even better with respect to CdSe-ZnS water-soluble QDs [96] and fluorescently doped mesoporous nanoparticles [97], while it is more than one order of magnitude better than other purely organic nanoparticles [95].

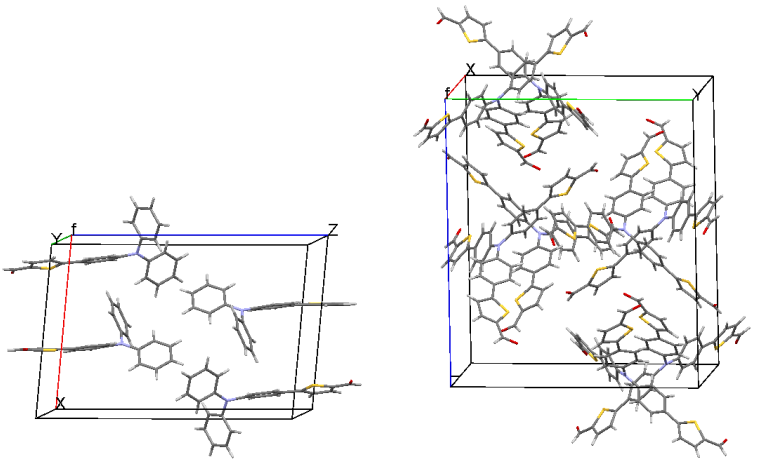


*Figure 2.9: Crystal packing of **T1** (left) and **T2** (right) from single-crystal X-Ray diffraction [17].*

*Table 2.2: Estimation of the number of chromophores per nanoparticle and of the two-photon brightness and peak TPA cross section of a single nanoparticle (FON).*

| | R [nm][a] | Chromophores per FON [x10$^4$][b] | $\sigma_2^{max}$ per FON [10$^6$ GM][c] | $\sigma_2^{max}\Phi$ per FON [10$^5$ GM][d] |
|---|---|---|---|---|
| **T1 FONs** | 17±2 | 5±2 | 5±2 | 8±3 |
| **T2 FONs** | 17±2 | 4±1 | 8±3 | 1.6±0.6 |

*[a] Mean radius of the nanoparticles (estimated by TEM). [b] Mean number of chromophores per nanoparticle, obtained from the mean radius of the nanoparticles (assumed as spherical) and the density of* $1.340\ g/cm^3$ *for **T1** and* $1.438\ g/cm^3$ *for **T2** (from X-Ray structural data). [c] Two-photon absorption cross section per nanoparticle, obtained by multiplying the mean number of molecules per nanoparticle (this Table) times the molecular TPA cross section measured for the FON suspensions (Table 2.1). [d] Two-photon absorption action cross section ($\sigma_2\Phi$) per nanoparticle. $\Phi$ is the fluorescence quantum yield.*

On these bases, gigantic TPA cross sections can be derived for the single nanoparticles, ranging from $3 \times 10^6$ to $7 \times 10^6$ GM for nanoparticles of **T1** and from $5 \times 10^6$ to $11 \times 10^6$ for nanoparticles of **T2**. Very large maximum TPEF action cross sections of about $8 \times 10^5$ GM and $1.6 \times 10^5$ GM can be estimated for single FON of chromophore **T1** and **T2**, respectively [17]. Such large two-photon brightness per nanoparticle makes these FONs of high interest for use as fluorescent markers or tags and make them attractive for bioimaging applications. In particular, the nanometer size suggests their possible use as contrast agents for angiography purpose.

In order to compare the intrinsic two-photon response of various types of luminescent nanoparticles of different composition and/or size for bioimaging purpose, their two-photon brightness per nanoparticle's unit volume has been evaluated (Table 2.3).

*Table 2.3: Two-photon absorption action cross section per nanoparticle and per nanoparticle's unit volume for our **T1** and **T2** FONs and for other nanoparticles of different size and nature from the litterature [95, 96, 97].*

| | R [nm] | $\sigma_2 \Phi$ per nanoparticle [$10^5$ GM] | $\sigma_2 \Phi$/V [GM nm$^{-3}$] |
|---|---|---|---|
| T1 FONs | 17±2[a] | 8.1 | 39±15[a] |
| T2 FONs | 17±2[a] | 1.6 | 8±3[a] |
| Water Soluble QDs | 14; 7[b] | 0.47 | 4; 30[c] |
| Nanoaggregates | 100 | 35 | 1 |
| Doped Silica NPs | 50 | 36 | 7 |

*[a] Gap based on the size uncertainty. [b] Hydrodynamic and dry radius, respectively, according to [96]. [c] Based on the hydrodynamic and dry radius, respectively.*

## 2.4 *In vivo* Two-Photon Microscopy using Organic Nanoparticles as Probes

The nanoaggregates in water suspension as well as the solutions of dyes **T1** and **T2** in DMSO are tested as contrast agents for *in vivo* 3D TPEF imaging on living Xenopus laevis tadpoles. For the biological experiments, two solutions of **T1** and **T2** are prepared: the first ones are composed by the dyes dissolved in DMSO at $2 \times 10^{-5}$M, and the second ones are the aqueous suspensions of FONs at the same total dye concentration.

The TPEF images for the dye solutions and FONs have been firstly registered just 20 min after injection in the vascular system, and then after 90 min. Such a time interval is intended to gain information about the development of molecular aggregation, if any, in the biological environment. In biological conditions, compound **T2** aggregates very rapidly to give 10-30 μm size agglomerates which deposit in the small blood vessels, hindering blood flow and resulting ultimately in the death of the tadpole. It is found that the direct injection of both the suspension of **T2** FONs in water and the solution of **T2** in DMSO induce the formation of such microparticles inside the tadpole vessels (Figure 2.10). At opposite, such phenomenon is not observed with compound **T1**. This suggests a different colloidal stability for the two nanoaggregates in blood, and also a different behavior with respect to the aqueous medium, where the long-term stability of **T2** FONs suspension is better than that of **T1** FONs suspension. The fact that **T1** FONs are instead more stable in blood can be related to the different ionic strength of the biologic medium with respect to water and their stability in blood is long enough (up to hours) to be of high interest in bioimaging applications. As may be noticed from Figure 2.11, with dye **T1** in DMSO a very weak and diffuse fluorescence was observed and no vessels could be imaged in spite of the good TPA cross section of the dye.

This can be ascribed to the fast diffusion of the small dye molecules through the vascular system walls, resulting in low signal. In contrast,

the blood vessels could be easily imaged when the water suspension of **T1** FONs is injected (using the same overall concentration of chromophore **T1** in DMSO). No acute toxicity is noted during and after the experiments. This demonstrates that **T1** FONs are promising fluorescent tracers for two-photon *in vivo* angiography.

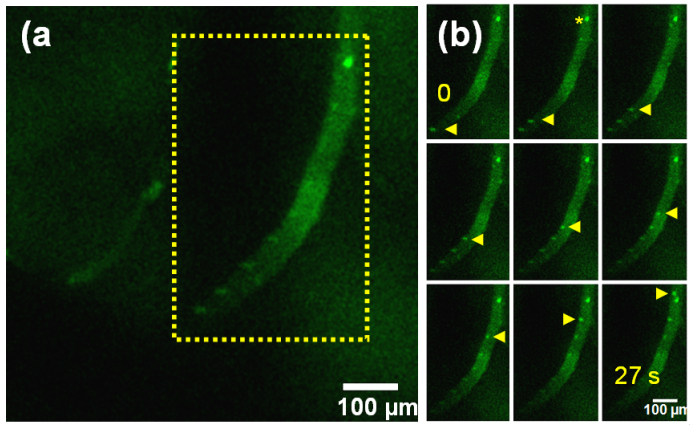


*Figure 2.10: (a) TPEF image of a blood vessel after injection of a **T2** DMSO solution. (b) The cropped portion in (a) is monitored for the motion of the mobile aggregates with respect to a static particle (*) for a duration of 27 s; the delay between frames is 3 s.*

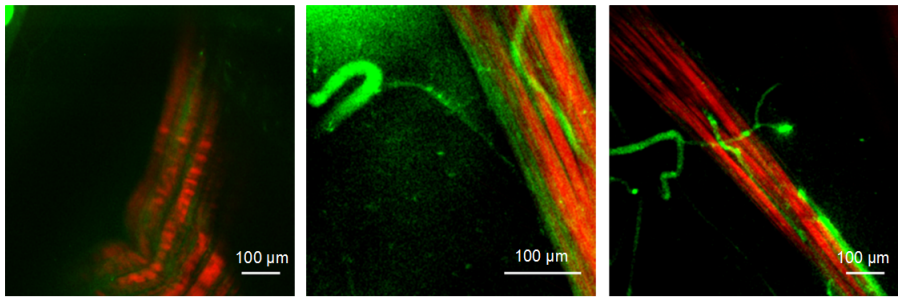


*Figure 2.11: From left to right: 3D projection TPEF and Second Harmonic Generation (SHG) image 20 min after injection of dye* ***T1*** *in DMSO (left); 3D projection TPEF and SHG image 20 min after injection of* ***T1*** *FONs suspension (dye content: $2 \times 10^{-5} M$) (middle) and 90 min after injection (right). For all images, the red color corresponds to the endogenous SHG signal (410 nm) that arises from muscle tissue, while green corresponds to the TPEF signal generated in vivo by the dye (460-590 nm). Scale bar = 100 µm.*

## 2.5 Conclusions

In the first part of this chapter a general description of different types of biphotonic probes (inorganic, inorganic/organic, organic) was reported. In the second part the attention was focused on the experimental results obtained by using fluorescent organic nanoparticles (FONs) obtained from a dipolar (**T1**) and a octupolar (**T2**) triphenylamine-based chromophores as bio-imaging tracers.

The suspensions in water of the FONs have been spectroscopically characterized by linear and nonlinear optical techniques, namely absorption, fluorescence and two-photon induced fluorescence. The fluorescence quantum yields of the nanoparticle suspensions in water are reduced with respect to the chromophore solutions in organic solvents, but stay sizable for FONs of the octupolar chromophore (about 2%) and quite good for FONs of the dipolar chromophore (about 15%). The luminescent properties of these nanoparticle suspensions in water made possible the determination of the two-photon induced action cross section of the FONs. The TPA profile of the FONs in water is broadened with respect to organic solvents, and the peak magnitude is lowered. This effect is much more pronounced for the octupolar compound which shows a maximum TPA response only twice that measured for the FONs of the dipolar analogue. This behavior, together with the higher fluorescence quantum yield of the nanoparticles of **T1** compound, corresponds to a better two-photon brightness for the FONs (of similar size) obtained from the dipolar chromophore, making them better candidates for imaging applications. The TPA cross section per FON of compound **T1** in water amounts to $\sim 5 \times 10^6$ GM, and the corresponding TPEF action cross section (i.e. two-photon brightness) to $\sim 8 \times 10^5$ GM: these are unprecedentedly large values for fluorescent organic nanoparticles of that size in water suspension. Such (non-resonant) gigantic values are larger than those reported earlier for other nanoparticles in water such as quantum dots (QDs) [96] and similar to that reported for bigger (typically 100-200 nm

in diameter) organic nanoaggregates [95] or silica mesoporous nanoparticles doped with organic biphotonic fluorophores [97]. In order to compare the intrinsic two-photon response of various types of luminescent nanoparticles of different composition and/or size, for bioimaging purpose, we evaluate their two-photon brightness per nanoparticle's unit volume (Table 2.3). The two-photon brightness per unit volume of our organic nanoparticles is comparable or even better with respect to CdSe-ZnS water-soluble QDs [97] and fluorescently doped mesoporous nanoparticles [97], while it is more than one order of magnitude better than other purely organic nanoparticles [95]. The gigantic two-photon brightness of the prepared FONs in water suspension has been exploited for two-photon imaging on living Xenopus laevis tadpoles. The results obtained for the FONs of **T1** are extremely good for imaging the blood vessels, in terms of brightness, stability and contrast. Moreover, the use of a water suspension allows for a 98% reduction of injected organic solvent, with the consequence of a reduced toxicity. All of these characteristics make our FONs promising fluorescent tracers for two-photon *in vivo* angiography. Further efforts are required to prevent aggregation of FONs and to improve their colloidal stability such as the use of stabilizers or different preparation processes.

# Chapter 3

# Colloidal Stabilization of Organic Nanoparticles

## 3.1 Classical Methods for Stabilizing Colloids: Overview

The colloidal stability of organic nanoparticles is a challenge for scientists because it is not possible to predict the final size and shape and the occurring of aggregation phenomena from the molecular structure of the dyes. It is indeed well know that the characteristics of the nano-products depend not only on the structure and concentration of the starting compounds, but also on the interchromophoric interactions that take place in the nano-bulk state. Other variables that can largely affect the stability of nanoparticles are the preparation process and the presence of additives and/or polymers.

Colloidal particles (1-1000 nm of diameter) in a dispersion medium always show Brownian motion and hence collide with each other frequently. The stability of colloids is thus determined by the interaction between the particles during such collisions. There are two basic interactions, one being attractive and the other repulsive. When attraction dominates, the particles adhere with each other and finally the entire dispersion may coalesce.

When repulsion dominates, the system will be stable and remain in a dispersed state [98]. In general the surface charge of nanoparticles (i.e. the stability) can be evaluated through zeta-potential values (see below): values lower than -30 mV or higher than +30 mV are indicative of good colloidal stability because of the repulsion forces [99].

Van der Waals forces are the primary source of attraction between colloidal particles. These forces are always present between particles of similar composition. Therefore, a colloidal dispersion is said to be stable only when a sufficiently strong repulsive force counteracts the van der Waals attraction [98]. There are three different possible origins for van der Waals forces: permanent dipole-permanent dipole forces, the permanent dipole-induced dipole interactions and transitory dipole-transitory dipole (London) forces. The first two are very short-range interactions, but the London forces are longer-range attractions. Since only London forces contribute to the long-range attraction between colloidal particles, the magnitude and range of the van der Waals-London (VDWL) attraction are decisive in determining strategies for stabilizing colloid particles. For many colloid systems, the range of significant VDWL attraction is between 5 and 10 nm.

Since there are always strong, long-range attractive forces between similar colloidal particles, it is necessary to provide a long-range repulsion between the particles to improve their stability. This repulsion should be at least as strong as the attractive force and comparable in range to the attractive interaction. Stability can be obtained by surrounding colloidal particles:

- with an electrical double layer (electrostatic or charge stabilization);
- with adsorbed or chemically attached polymeric/additive molecules (steric stabilization);
- with free polymer in the dispersion medium (depletion stabilization).

Combination of the first two stabilization mechanisms lead to electrosteric stabilization. The latter two types of stabilization are often realized by the addition of polymers to stabilize dispersions.

### 3.1.1 Electrostatic Stabilization

When a surface is immersed in aqueous solution, it usually acquires a net electric charge. This can arise from dissociation of surface charged species, accumulation or depletion of electrons at the surface, protonation or deprotonation of charged species onto the surface. In order to preserve the electroneutrality of the system, the surface bound charges are counterbalanced by oppositely charged counter ions that assemble in the bulk close to the interface (called Stern layer). Surrounding the Stern layer is an assembly of counter ions and co-ions, which, due to the thermal agitation in the solution, are distributed in a three-dimensional region called the diffuse layer. Together these two layers define the so-called electric double layer [100] (Figure 1.6). The electric potential within the electric double layer has the maximum value on the particle surface (Stern layer). The potential drops with the increase of distance from the surface and reaches 0 at the boundary of the electric double layer. When a colloidal particle moves in the dispersion medium, a layer of the surrounding liquid remains attached to the particle. The boundary of this layer is called slipping plane (shear plane). The value of the electric potential at the slipping plane is called Zeta potential, which is a very important parameter in the theory of interaction of colloidal particles. In charge stabilization, it is the mutual repulsion of these double layers surrounding particles that provides stability. The thickness of the double layer depends, amongst others, on the ionic strength of the dispersion medium. The ionic strength $I$ ($^{mol}/_{dm^3}$) can be expressed as $I = \frac{1}{2}\sum_i z_i^2 c_i$, where $z_i$ is the valence and $c_i$ the molar concentration of ion $i$. For a given ionic strength, the characteristic decay length of the double layer, the so-called Debye screening length $k^{-1}$, can be calculated according to the equation:

$$k^{-1} = \left[\frac{\varepsilon\varepsilon_0 k_B T}{1000 e^2 N_A 2I}\right]^{\frac{1}{2}}$$

where $\varepsilon$ is the relative permittivity, $\varepsilon_0$ is the vacuum permittivity, $k_B$ is the Boltzman constant, $T$ is the temperature, $e$ is the elementary charge and $N_A$ is the Avogadro number. As seen from the equation, the double-layer thickness increases monotonically with decreasing ionic strength. At low ionic strengths, the thickness of the double layer is about 5-10 nm, which is of the same order as the VDWL attraction. This explains the observation of charge stabilization in dispersion media of low ionic strength. The thickness of the double layer is reduced significantly with increasing the ionic strength. In that case, the range of double layer electrostatic repulsion is sometimes insufficient to counterbalance the VDWL attraction [101]. This is particularly true for metal nanoparticles in which Van der Waals interactions are much larger than in soft matter.

When two nanoparticles approach each other, electrostatic double-layer interactions arise due to overlap of their diffuse double-layers. The overlap gives rise to a repulsive force that increases the closer the particles approach each other and allows to stabilize the suspension. In particular, organic nanoparticles, depending on the molecular structure of the departing chromophores, can show naturally charged surface or the surface can be made charged by the addition of charged additives (Paragraph 1.2).

### 3.1.2 Steric and Depletion Stabilization

Nanoparticles can be straightforwardly stabilized by adsorption of large, bulky molecules, e.g. polymers, onto their surfaces. As the modified particles approach each other, the surface-bound molecules must reorganize or compress due to the size exclusion effect. Thereby, the conformational entropy of the individual molecules decreases, resulting in a net repulsive force between the particles. If the compression also imposes rearrangement of water molecules associated to the particle surfaces, additional hydration forces

may arise [102]. Since the origin of the repulsive force is due to steric restrictions, this technique to stabilize particles is often referred to as *steric stabilization* (Figure 3.1).

*Depletion stabilization* of colloidal particles (Figure 3.1) is imparted by macromolecules that are free in solution. The study of this type of stabilization is still in its initial stage. The combination of depletion and steric stabilization is very common when there are high concentrations of free polymer in the dispersion medium.

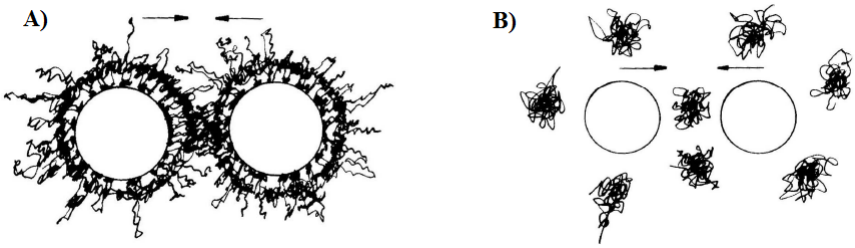


*Figure 3.1: A) Schematics of steric stabilization. B) Schematics of depletion stabilization.*

## 3.2 Stabilization of Organic Nanoparticles using Ultrasounds and Low-Concentration Additives

In principle it is very difficult to control the final morphology of the nanoparticles and their colloidal stability, but some modifications on the synthetic parameters as the initial dye concentration, medium temperature, applied microwaves or ultrasounds irradiation, use of microemulsion and use of additives or polymers as coating agents have been developed for this purpose [103, 104, 105, 106, 107, 108, 109]. However, a comparative study of the properties of nanoparticles prepared by reprecipitation method assisted by sonication with different types of additives and counter ions (at low con-

centrations) has not been reported in the literature yet. In this section the investigation of morphological and spectroscopic characteristics of FONs obtained from the Triphenylamine-based push-pull compound **T1** (described in Section 1.4.1) reprecipitated in aqueous solution under ultrasounds and in presence of different types of additives (anionic, cationic and non-ionic, see Figure 3.2) are reported. We find that the use of ultrasounds during the reprecipitation process probably alters the structure of FONs and increases the colloidal stability. Furthermore, the presence of additives and the nature of their counter ions play a key role on inducing or suppressing aggregation and, consequently, on the spectroscopic properties of the suspensions. In particular we experience that the presence of **Nilered**-based cations in solution even if at very low concentrations (less than $10^{-7}$M), dramatically exalts the formation of agglomerated structures. In addition, the proximity of this chromophore to the nanoparticles is evidenced by the observation of energy transfer from the Triphenylamine-based chromophore (donor) to the **Nilered**-based (acceptor) dye, monitored by steady-state fluorescence of the suspensions.

### 3.2.1 Preparation of Nanoparticles with Ultrasounds and Additives

Nanoparticles of compound **T1** are firstly prepared using the simple reprecipitation method at 5°C as described in Chapter 1 (**FONs-A**). Subsequently all the suspensions are prepared using stirring and ultrasounds. In a bath of ice (bath temperature: 5°C) an amount of 300 µL of a 1 mM stock solution of **T1** in THF is added to 14.700 mL of HPLC-grade water under vigorous stirring, to achieve a final nominal concentration of $2 \times 10^{-5}$M and water/THF ratio of 98:2 v/v. The solution is kept under stirring and sonication for 1.5 h at 5°C. Ultrasounds are generated in the solution using a VibraCell 1300W ultrasonic processor with a probe of 6 mm of diameter, an amplitude of 20% and a pulse time of 1 s (**FONs-B**).

The preparation with additives follows the same procedure described

above, but in this case an amount of 300 μL of a 1 mM stock solution of **T1** in THF is added to 14.700 mL of a $1\times10^{-7}$M aqueous solution of additive. The obtained suspensions are called **FONs-C** (CTAB as additive), **FONs-D** (SDS as additive), **FONs-E** (Brij30 as additive), **FONs-F** (choline chloride as additive) and **FONs-G** (choline methylsulfate as additive). Finally, two suspensions with different amounts of choline methylsulfate and **Nilered**-methylsulfate ($9\times10^{-8}$M and $1\times10^{-8}$M respectively for **FONs-G1**, and $5\times10^{-8}$M and $5\times10^{-8}$M respectively for **FONs-G2**) have been prepared, thus maintaining the total additive concentration at $1\times10^{-7}$M. The molecular structures of additives are reported in Figure 3.2.

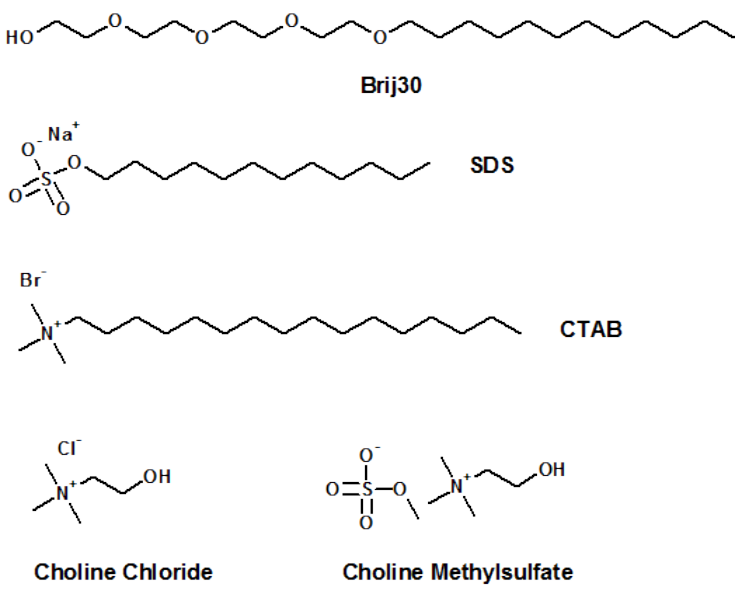


*Figure 3.2: Additives used for the preparation of nanoparticles.*

### 3.2.2 Morphological Characterization

To gain information on the morphology and size of nanoparticles, transmission electron microscopy (TEM) has been achieved after the precipitation process and after three weeks (Figure 3.3). The statistical analysis from TEM images is reported in Figure 3.4 and the average diameters of nanoparticles calculated from this analysis are reported in Table 3.1.

TEM images reveal that the freshly prepared nanoparticles have a quite narrow size-dispersion in all the cases, but shape and colloidal stability change by varying the type of additive and preparation. Nanoparticles with a diameter of about 25 nm are obtained using the classical reprecipitation method at 5°C (**FONs-A**), which is the same result obtained for the synthesis at 20°C, as reported in Chapter 1. After three weeks these nanoparticles show tendency to agglomerate and precipitate, so only the supernatant can be investigated. This is an evidence that, for **T1** dye, the classical preparation strategy (stirring without ultrasounds) generates nanoparticles with tendency to grow, agglomerate and precipitate after some weeks, independently of the reprecipitation temperature. Preparation with the aid of ultrasounds reduces mainly the aggregation but also the growth of diameter of nanoparticles during time. Statistical analysis on TEM images of **FONs-B** indicates that after 3 weeks there is a little increase of diameter (Figure 3.4): the percentage of particles with diameter between 20-25 nm undergoes a growth at the expense of the particles with diameter shorter than 15 nm. This could probably be a consequence of the effect known as Ostwald ripening, largely observed for **T1** nanoparticles (Chapter 1, Figure 1.11). TEM images of 3-weeks-aged nanoparticles reveal also the presence of nanometric aggregates of FONs that do not exceed 100 nm of width, which are the cause of the percentage of nanoparticles with a diameter greater than 40 nm. Anyway, because of the better stability of nanoparticles obtained with the preparation performed under ultrasounds, all the other samples (with additives) are prepared in this manner. The same trend described

above is also observed for **FONs-C**, **FONs-D**, **FONs-E** and **FONs-F**: in all the cases a little growth of the nanoparticles diameter and the formation of nanometric aggregates are observed after some weeks, even if these effects are much more reduced than the effects observed for **FONs-A** (Figure 3.3).

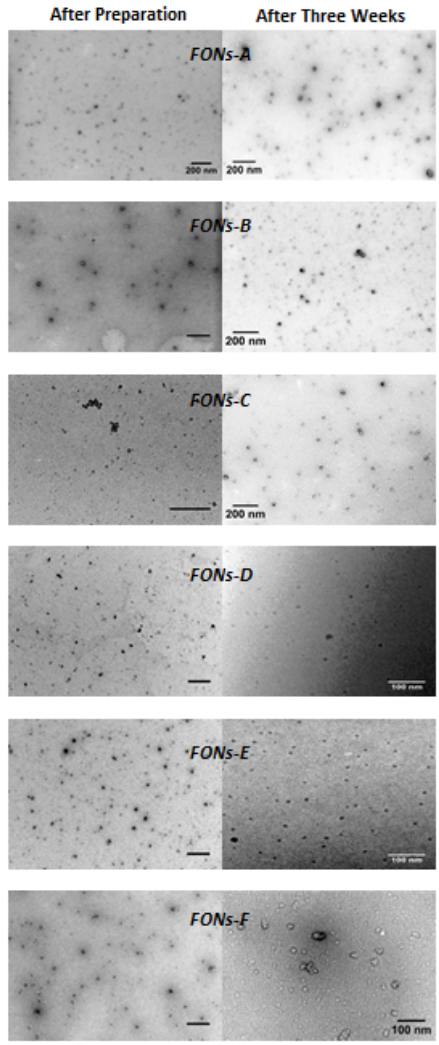


*Figure 3.3: TEM images of nanoparticles after preparation (left column) and after three weeks (right column). Scale bar (where not set) = 200 nm. For* ***FONs-A*** *the image after three weeks is referred to the supernatant. For* ***FONs-D*** *and* ***FONs-E*** *particles are very difficult to detect: no aggregates or big structures are present, and particles look like dissolved. It is possible to detect some nanometric round structures, but it is very difficult to establish their exact nature. For this reason no statistical analysis has been performed on these samples.*

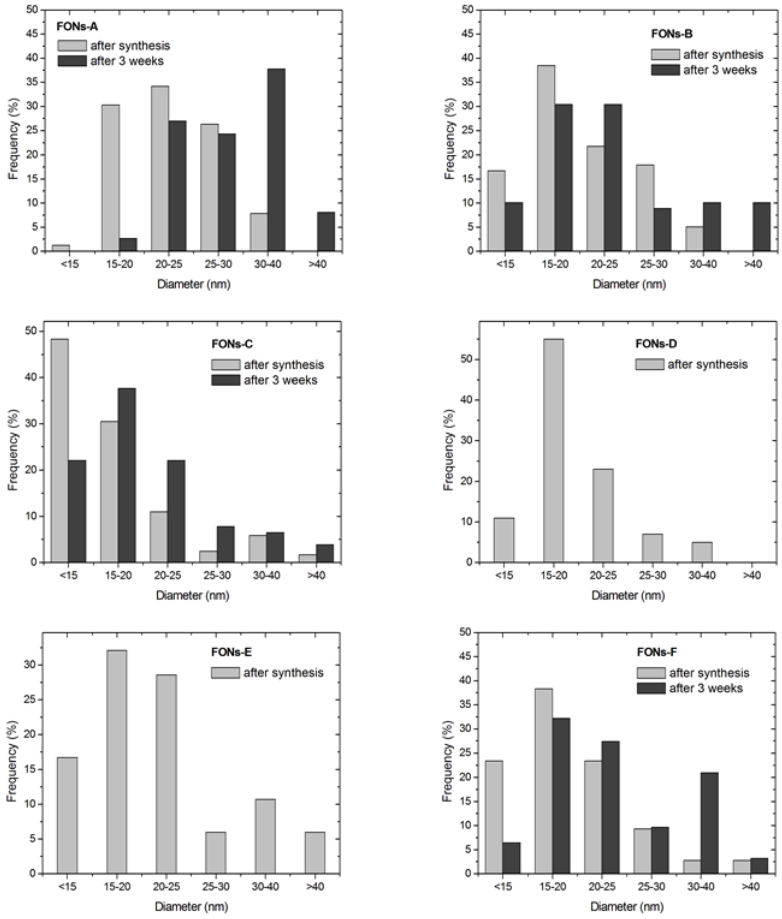


*Figure 3.4: Statistical analysis of nanoparticle sizes from TEM images.*

In particular:

- *FONS-A* : TEM images after preparation and after 3 weeks reveal that nanoparticles aggregate into micrometric structures. These structures are also visible to the naked eyes. Statistical analysis on supernatant indicates that after 3 weeks there is also an increase of particle size: the distribution of diameter shifts toward bigger values.

- *FONs-B* : Statistical analysis of TEM images indicates that after 3 weeks there is a little increase of particle diameter: the percentage of particles with diameter between 20-25 nm is growing at the expense of the particles with diameter less than 15 nm. Furthermore the increase of particles with diameter greater than 40 nm is due to the presence of nanoaggregates that do not exceed 100 nm.

- *FONs-C* : After preparation nanoparticles are more regular in shape and dimension than **FONs-B**. Statistical analysis of TEM images after 3 weeks indicates that the size of particles grows: after synthesis about 50% of particles have a diameter less than 15 nm, after 3 weeks this percentage is reduced to 20% and there is a significant increase of particles with diameter between 15-20 and 20-25 nm. Nevertheless the percentage of particles/aggregates with diameter greater than 40 nm does not change very much, this indicates that only very little aggregation takes place during time.

- *FONs-D* : After preparation nanoparticles are regular in shape and dimension, but after 3 weeks it is not possible to properly detect the nanocompounds.

- *FONs-E* : After preparation nanoparticles are regular in shape and dimension, but after 3 weeks it is not possible to properly detect the nanocompounds.

- *FONs-F* : Statistical analysis of TEM images after 3 weeks indicates that there is a little increase of particle size: after synthesis about 20% of particles have a diameter less than 15 nm, but after 3 weeks this percentage decreases to 5% and the number of particles with a diameter between 20 and 25 nm grows. The percentage of particles with a diameter between 30 and 40 nm also grows: this is due to the presence of nanoaggregates of this size.

- *FONs-G* : After preparation nanoparticles are irregular in shape and dimension (average diameter of about 25 nm) and they aggregate and precipitate quite rapidly (after few days).

These results suggest that the use of ultrasounds and additives drastically decreases nanoparticle aggregation but does not totally suppress Ostwald ripening. Interestingly, the nanoparticles prepared with choline methylsulfate (**FONs-G**) are bigger, than those synthesized with choline chloride (**FONs-F**) and aggregate quite rapidly. This is an evidence that the nature of the counter ion, and therefore the ionic strength of the solution, play a key role on the nucleation stage and, consequently, on the final nanoparticle size and shape. Surprisingly, by adding another molecule ($Nilered^+ - Methylsulfate$ Figure 3.5, hereafter called $Nilered^+$ for simplicity) to choline methylsulfate while leaving unchanged the total concentration of additives ($1 \times 10^{-7}$M) a dramatic augmentation of aggregation and a change of shape of FONs are observed (Figure 3.6).

The increasing of the $Nilered^+/Choline$ ratio (**FONs-G1** and **FONs-G2**) promotes a greater aggregation of molecules than in the other cases and a drastic change on the shape, that becomes more and more irregular (Figure 3.6). Moreover, complete precipitation of the compound just after synthesis is observed if $Nilered^+$ is used as unique additive (at $1 \times 10^{-7}$M). TEM results suggest that the conditions of preparation (with or without ultrasounds) but also the presence of additives and, in particular, the nature of their counter-ions dramatically affect nucleation and colloidal stability of the nanoparticles.

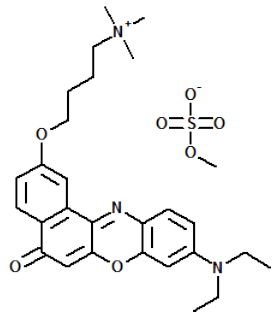

*Figure 3.5: Molecular structure of* $Nilered^{+} - Methylsulfate$.

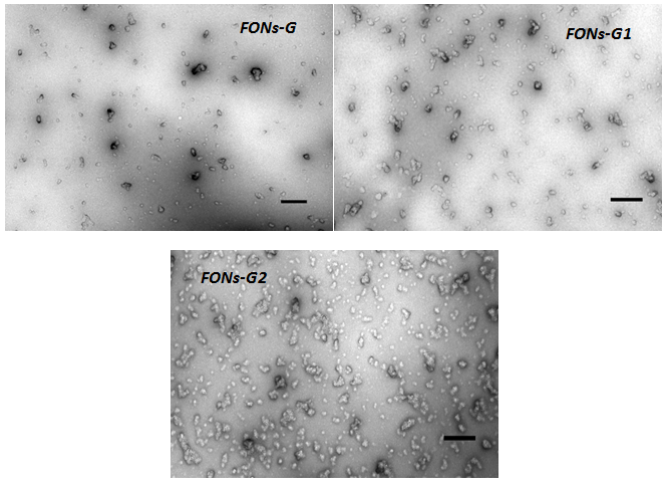


*Figure 3.6: TEM images of* ***FONs-G***, ***FONs-G1*** *and* ***FONs-G2*** *after preparation. Scale bar = 200 nm.*

### 3.2.3 Spectroscopic Characterization

All the spectra have been recorded for the dye suspensions in the native aqueous mixture, at the end of the reprecipitation process. Absorption spectra are measured using a spectrofluorimeter equipped with an integrating

sphere. Absorption and emission spectra of compound **T1** dissolved in different organic solvents and its FONs obtained using reprecipitation without additives and sonication (**FONs-A**) are reported in Chapter 1. Compound **T1** dissolved in organic solvents displays an intense absorption band in the violet region (400 - 410 nm), while the absorption spectrum of **FONs-A** in water is red-shifted with respect to that of **T1** dissolved in organic solvents (including polar dimethylsulfoxide, DMSO). Instead, for all the nanoparticles prepared with ultrasounds (with or without additives) the absorption spectrum is generally blue shifted (maximum at about 380 nm) and broadened compared to the spectra of compound **T1** in organic solvents and of **FONs-A** (Figure 3.7). The fluorescence spectrum of nanoparticles prepared with ultrasounds (**FONs-B**) is structured and is blue-shifted compared to **FONs-A**, falling in the green region with maximum at 516 nm (Table 3.1). It is noteworthy that the shape of the emission spectrum is very similar to that of the solid state (while this is not the case for **FONs-A**), except for the presence of a shoulder at about 455 nm: this suggests that the packing of molecules in the nanoparticles prepared with ultrasounds could be similar to that in the solid state (Figure 3.8). The differences on emission between **FONs-A** and **FONs-B** can also be observed under UV-lamp (inset of Figure 3.8). No essential changes are observed on emission spectrum of **FONs-B** after 3 weeks, only a little growing of the shoulders at about 455 nm and 470 nm. On the contrary, massive aggregation is observed in **FONs-A** suspension (Figure 3.9 and inset).

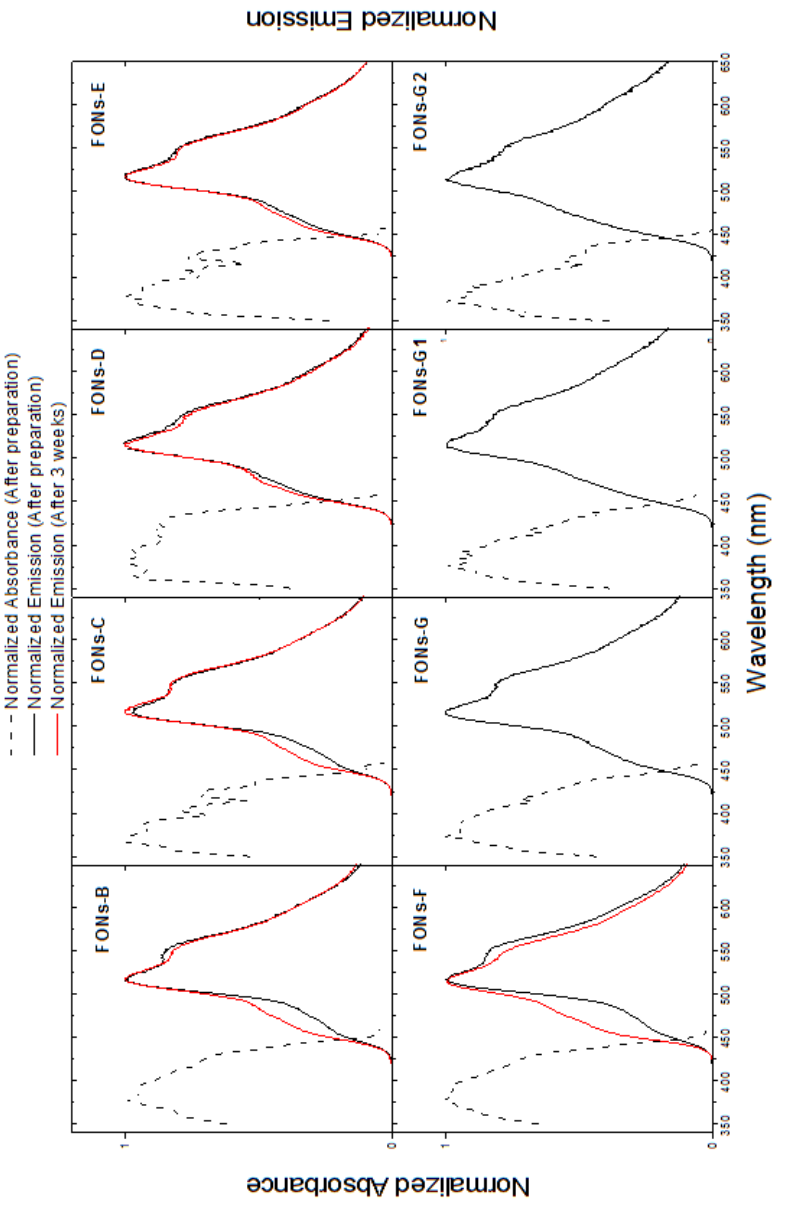


*Figure 3.7: Absorption and emission spectra of the nanoparticles suspensions.*

*Table 3.1: Spectroscopic characteristics and average diameter of FONs after preparation.*

| | Additive | $\lambda_{em}$ [nm] | τ [ns] [a] | Φ [b] | $k_r$ [$\times 10^8\ s^{-1}$] [c] | $k_{nr}$ [$\times 10^8\ s^{-1}$] [c] | Ø [d] |
|---|---|---|---|---|---|---|---|
| **FONs-A** | no | 537 | 0.95 (43%)<br>3.33 (57%) | 15% | 0.94 | 5.30 | 25 |
| **FONs-B** | no<br>(sonication) | 516 | 3.60<br>(100%) | 22% | 0.61 | 2.17 | 20 |
| **FONs-C** | CTAB | 516 | 1.07 (17%)<br>4.12 (83%) | 18% | 0.65 | 2.95 | 17 |
| **FONs-D** | SDS | 517 | 1.10 (26%)<br>3.70 (74%) | 30% | 1.31 | 3.05 | 20 |
| **FONs-E** | Brij30 | 517 | 0.87 (36%)<br>3.64 (64%) | 25% | 1.48 | 4.42 | 25 |
| **FONs-F** | Choline chloride | 516 | 3.77<br>(100%) | 21% | 0.56 | 2.09 | 21 |
| **FONs-G** | Choline methylsulfate | 516 | 0.54 (38%)<br>3.60 (61%) | 16% | 1.39 | 7.34 | 25 |
| **FONs-G1** | Choline methylsulfate<br>+ $NR^+$ methylsulfate | 516 | 0.56 (49%)<br>3.60 (51%) | 13% | 1.32 | 8.85 | 28 |
| **FONs-G2** | Choline methylsulfate<br>+ $NR^+$ methylsulfate | 516 | 0.61 (55%)<br>3.32 (45%) | 14% | 1.45 | 8.92 | 28 |

*[a] Fluorescence lifetime(s) obtained through mono- or bi-exponential reconvolution fit (taking into account the instrument response function) of the fluorescence decay. The fitting decays are judged through the reduced $\chi^2$ values (fit are accepted for $\chi^2 < 1.1$). The fraction of the corresponding fluorescence decay ($\eta$) is reported in brackets. [b] Fluorescence Quantum Yield, measured using integrating sphere in center mount sample holder configuration. [c] Calculated as: $k_r = \Phi \sum_i \frac{\eta_i}{\tau_i}$ ; $k_{nr} = \sum_i \frac{\eta_i}{\tau_i} - k_r$ where $\eta_i$ is the fraction of fluorescence decay. [d] Mean diameter of the nanoparticles (estimated by the analysis of TEM images).*

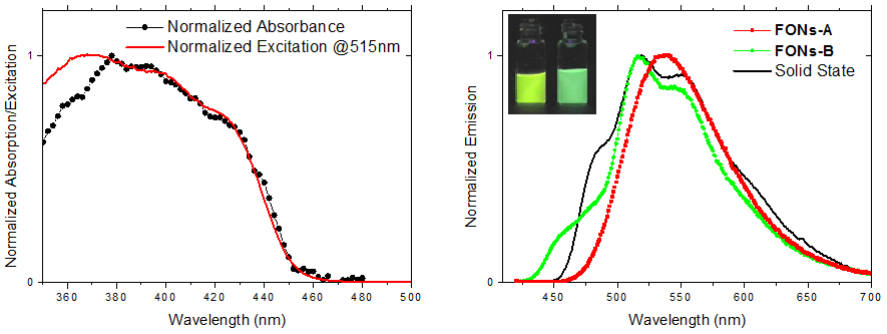


*Figure 3.8: Absorption (left) and emission (right) spectra of **FONs-A** and **FONs-B** after preparation. For comparison, the emission spectrum of solid state of compound **T1** is reported (solid black line). Inset: images of **FONs-A** (left) and **FONs-B** (right) suspensions observed under UV-lamp ($\lambda_{ex}$ = 360 nm).*

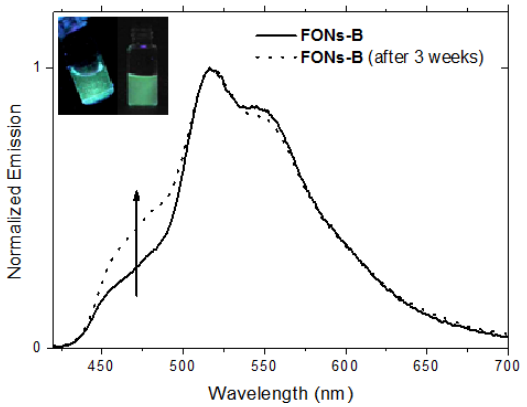


*Figure 3.9: Emission spectra of **FONs-B** after synthesis (solid line) and after 3 weeks (dotted line). Inset: images of **FONs-A** (left) and **FONs-B** (right) 3 weeks old observed under UV-lamp (λex = 360 nm). Micro-aggregates on the aged **FONs-A** suspension are well detectable to the naked eyes.*

A similar behavior is also observed for **FONs-C**, **FONs-D**, **FONs-E** and **FONs-F** suspensions: after preparation all the samples show almost identical structured emission spectra and after 3 weeks a little growth of shoulders at 455 nm and 470 nm is observed (Figure 3.7). The origin of this growth could be related to the aggregation of nanoparticles or to the presence of crystalline domains. Both "aged" and freshly prepared suspensions with particular additives (methylsulfate as anion) that show a grater aggregation than other samples, display also a remarkably increase of the bands described above.

**FONs-G**, **FONs-G1** and **FONs-G2** behaviors are slightly different. **FONs-G** display the same structured emission spectrum of **FONs-B** just after reprecipitation, but it is not possible to register the spectrum after some weeks because of the complete precipitation of the aggregated nanoparticles which takes place in few days. Just prepared **FONs-G1** and **FONs-G2** exhibit similar structured emission spectra observed in the previous samples with, in addition, a growth of the shoulders at 455 nm and 470 nm but, for the first time, a growth on the shoulder at about 600 nm can be observed (Figure 3.10).

By the subtraction of the emission spectrum of **FONs-G** from **FONs-G1** it is possible to detect a new weak band, that displays a maximum at about 610-620 nm: this value is very similar to that of $Nilered^+$ in THF (600 nm) as shown in the inset of Figure 3.10. This effect is probably caused by the energy transfer process (described in Section 4.1.1) between the molecules of compound **T1** (donor) and $Nilered^+$ molecules (acceptor), linked to the nanoparticle surface through weak interactions (Figure 3.11).

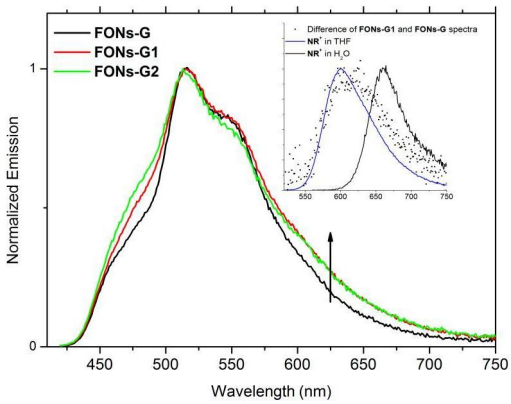


*Figure 3.10: Emission spectra of* ***FONs-G*** *(choline methylsulfate at* $1 \times 10^{-7} M$ *as additive, black line),* ***FONs-G1*** *(choline methylsulfate at* $9 \times 10^{-8} M$ *and at* $Nilered^{+}$ *at* $1 \times 10^{-8} M$ *as additives, red line) and* ***FONs-G2*** *(choline methylsulfate at* $5 \times 10^{-8} M$ *and* $Nilered^{+}$ *at* $5 \times 10^{-8} M$ *as additives, green line). A new shoulder in the range of 550-700 nm appears with the addition of* $Nilered^{+}$*, even if at very low concentrations. Inset: The difference between* ***FONs-G1*** *and* ***FONs-G*** *spectra (dot) is very close to the emission spectrum of* $Nilered^{+}$ *in THF (blue line).*

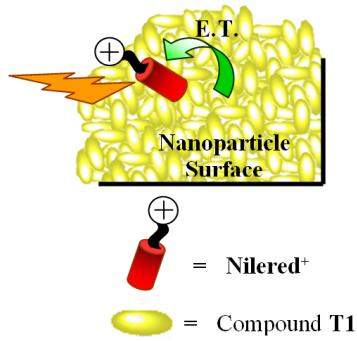


*Figure 3.11: Energy transfer between molecules of compound* ***T1*** *and* $Nilered^{+}$*, probably displaced at the nanoparticle surface.*

This hypothesis is supported by the fact that the fluorescence of $Nilered^+$ in water at the same concentration ($1 \times 10^{-8}$M) cannot be detected using identical instrumental conditions. The blue displacement of the new $Nilered^+$ band emission, compared to that in water, could be attributed to the proximity of molecules to the nanoparticle surface, that makes the environment less polar than water and more similar to THF. The growth of the emission signal of molecules used as dopant for organic nanoparticles is an occurrence that has been reported in some recent articles [110, 111, 112].

The fluorescence quantum yield after the preparation is found to be maximum for **FONs-D** (0.30) and minimum for **FONs-G1** (0.13), but for most of the samples it is close to 0.20. These values are lower than those of the dyes dissolved in chloroform but similar to those obtained in more polar organic solvents, such as DMSO, in which the quantum yield is found to be 0.25. The fluorescence decays are found to be bi-exponential for most of samples, except for **FONs-B** and **FONs-F** that are mono-exponential. Using the quantum yields and fluorescence lifetime values, the radiative ($k_r$) and non-radiative ($k_{nr}$) deactivation constants are calculated (Table 3.1).

## 3.3 Stabilization of Organic Nanoparticles by "Molecular Design"

The problem of colloidal stability of organic nanoparticles can also be dealt with another approach, here called "Molecular Design". From an empirical point of view the stability of nanoparticles is related to the molecular structure even if the mechanism has not been well understood yet. For sure the change of chemical structure can affect the solubility in water and consequently the nucleation rate, but may also have effects on the molecular packing in the nano-bulk and on the charge surface, leading to an increased (or decreased) stability.

In Ref. [95] Ishow an co-workes report stable nanoparticles based on triphenylamine compounds with different polarity. In particular, their chromophores have bulky substituted biphenyl groups attached to the amine group, in contrast to our **T1** chromophore which only bears a simple phenyl group linked to the amine center. Probably the biphenyl group, thanks to its typically twisted conformation, without substantially altering the spectroscopic properties of the chromophore, plays a key role in stabilizing nanoparticles of triphenylamine molecules. Based on this idea, we designed, prepared and characterized new chromophores (named **TW1** and **TW3**, Figure 3.12) modifying **T1** and **T3** chromophores, as to bear the bulky substituted biphenyl groups.

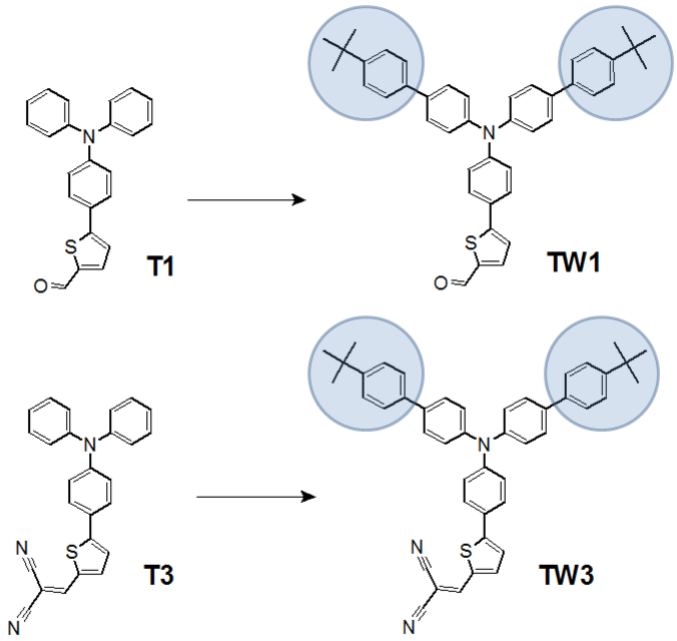


*Figure 3.12:* ***TW1*** *and* ***TW3*** *bulky chromophores.*

### 3.3.1 Synthesis of Chromophores

The synthesis of chromophores **TW1** and **TW3** has been performed by Blanchard-Desce's group following a multistep synthetic scheme (Figure 3.13). Bromination of the starting aldehyde is performed following an experimental protocol reported by Ref. [113]. A double Sonogashira reaction is then used to introduce two bulky side groups on aldehyde 3, yielding chromophore **TW1**, that can be further converted into chromophore **TW3** using a simple Knoevenagel condensation.

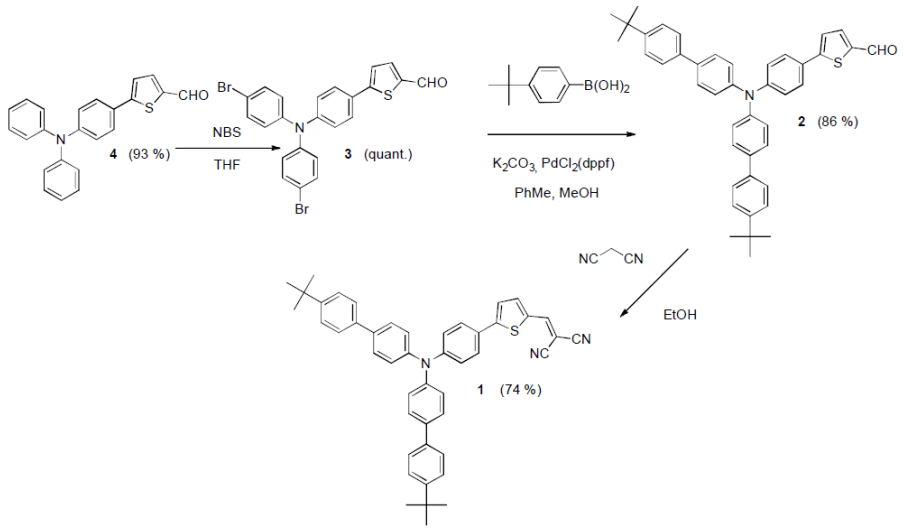


*Figure 3.13: Synthetic scheme of chromophores **TW3** (1) and **TW1** (2).*

### 3.3.2 Spectroscopic Characterization

Nanoparticles of **TW1** and **TW3** dyes are prepared using the reprecipitation method at a final nominal concentration of $2 \times 10^{-5}$M. Absorption and emission spectra of push-pull compounds **TW1** and **TW3** are very similar to those of **T1** and **T3** (Chapter 1), as expected. The results related to the chromophores in organic solvents of different polarity and FONs are summarized in Table 3.2 and the spectra are reported in Figure 3.14. **TW1** and **TW3** dissolved in organic solvents show an intense localized absorption band in the ultraviolet region (about 340 nm) and an intramolecular charge-transfer (CT) band at about 410 nm and 520 nm, respectively. Their emission band is strongly dependent on solvent polarity: it shifts towards red wavelengths when the environment polarity increases. The absorption spectra of both type of nanoparticles in water display a marked hypochromic effect, a red-shift and a broadening of the CT absorption band as compared

to dyes dissolved in organic solvents. The emission spectra of **TW1** and **TW3** FONs fall in the same region of the spectra of compounds dissolved in tetrahydrofuran (THF), i.e. in the green spectral region and in the red spectral region, respectively, with a fluorescence quantum yield of 0.07 and 0.06, respectively. The quantum yield of **TW1** FONs is lower than that of the dye dissolved in THF (0.67), while quantum yield of **TW2** FONs is quite similar to that of the compound in THF (0.07). The fluorescence decays of all the samples dissolved in organic solvents are found to be essentially monoexponential with fluorescence lifetimes in the nanosecond range. On the contrary, the fluorescence decays are found to be three-exponential for nanoaggregates (Table 3.2).

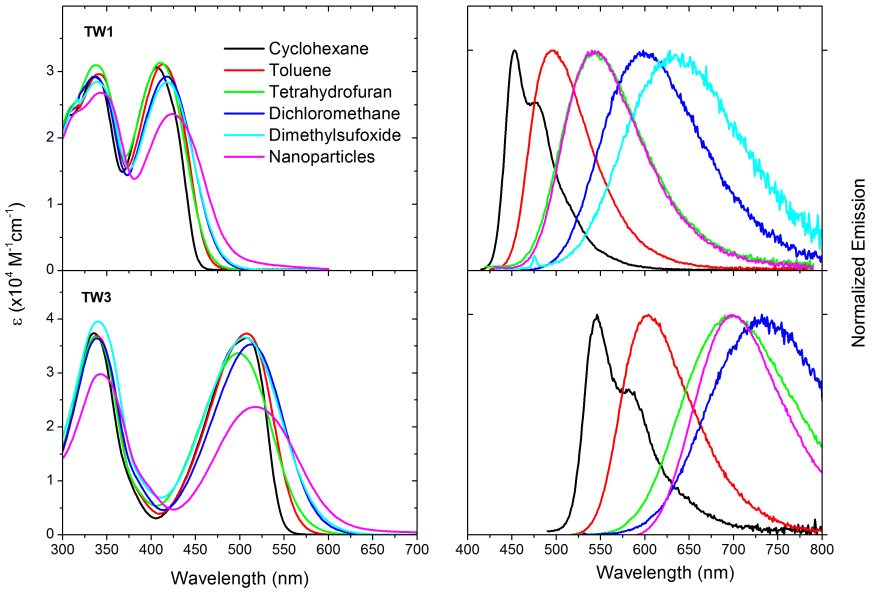


*Figure 3.14: Absorption and fluorescence solvatochromic behavior of chromophores **TW1** and **TW3** and corresponding nanoparticles.*

*Table 3.2: Photophysical properties of **TW1** and **TW3** in different solvents and of related FONs. Lifetimes are collected at the emission maximum using excitation wavelength of 405 nm for **TW1** samples and 460 nm for **TW3** samples.*

| | Solvent | $\lambda_{abs}^{max}$ [nm] | $\lambda_{em}^{max}$ [nm] | ε [$\times 10^4 M^{-1}cm^{-1}$] | $\Phi^a$ | τ [ns]$^b$ |
|---|---|---|---|---|---|---|
| TW1 | Cyclohexane | 406 | 453 | 3.07 | 0.63 | <0.5 (0.01); 1.86 (0.90) |
| | Toluene | 413 | 494 | 3.10 | 0.79 | 2.70 |
| | Tetrahydrofuran | 410 | 543 | 3.13 | 0.65 | 4.15 |
| | Dichloromethane | 417 | 598 | 2.92 | 0.39 | 3.06 |
| | Dimethylsulfoxide | 417 | 630 | 2.84 | 0.04 | <0.5 |
| | **FONs** | 424 | 552 | 2.43$^c$ | 0.09 | <0.5 (0.24); 1.48 (0.48); 4.19 (0.28) |
| TW3 | Cyclohexane | 509 | 546 | 3.65 | 0.13 | < 0.5 |
| | Toluene | 507 | 604 | 3.73 | 0.44 | 1.76 |
| | Tetrahydrofuran | 498 | 698 | 3.37 | 0.07 | <0.5 |
| | Dichloromethane | 513 | 730 | 3.53 | 0.02 | - |
| | Dimethylsulfoxide | 506 | - | 3.66 | <0.01 | - |
| | **FONs** | 517 | 700 | 2.37$^c$ | 0.07 | 0.72 (0.10); 3.56 (0.73); 8.29 (0.17) |

*[a] Fluorescence quantum yield estimated using Fluorescein as reference ($\phi = 0.90$). [b] Fluorescence lifetimes and, in parentheses, corresponding fraction of the fluorescence decay. [c] Referring to total dye concentration.*

Reprecipitation of nanoparticles of **TW1** and **TW3** has been monitored by UV-Vis spectroscopy (Figure 3.15). The process takes place within few seconds for both compounds, indeed no alteration on absorption spectra can be detected after this time. This result is very different from that obtained for **T1** compound in which reprecipitation was completed after about two hours. The different behavior probably depends on the slightly different solubility of the compounds in water. Even if **T1** is not directly soluble in water the constant of solubility is probably higher than that of **TW1**. This allows a lower level of supersaturation for **TW1** compound and a faster

process of nucleation. No aggregation of the obtained suspensions is observed during time even after some weeks, so the colloidal stability is reached.

Another confirmation of good colloidal stability is obtained from the zeta-potentials analysis of **TW1** and **TW3** suspensions. This technique allows the determination of the electrokinetic potential between the particle surface and the bulk solution, which is related to the surface charge density of the nanomaterial. Both nanoparticles have negatively charged surfaces, with zeta-potential values lower than -30 mV, indicative of good colloidal stability: -46 mV for **TW1** FONs and -36 mV for **TW3** FONs. .

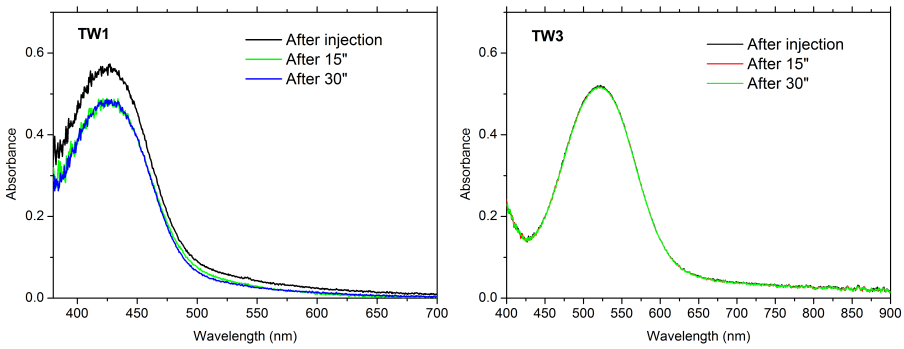


*Figure 3.15: Evolution of the UV/Vis absorption spectra of **TW1** (left) and **TW3** (right) during the reprecipitation process.*

## 3.4 Conclusions

At the beginning of the chapter the classical methods of stabilization of nanoparticles reported in the literature, as the electrostatic and steric stabilization, were described.

In the second part of the chapter we focused the attention on the experimental results obtained by reprecipitating the nanoparticles with ultrasounds and with low amounts ($1 \times 10^{-7}$M) of different types of additives. An improvement of colloidal stability is obtained using different preparative procedures, e.g. ultrasounds and stirring instead of only stirring. Furthermore, depending on the nature of the additive (anionic, cationic, non-ionic) and, in particular, the type of counter-ion, we obtained different results. FONs treated with CTAB, SDS, Brij30 and choline chloride show better colloidal stability than FONs without additives, as demonstrated by TEM images registered after preparation and after three weeks. The presence of additives, probably located on the surface of nanoparticles, play a key role in changing their surface charge and, consequently, in enhancing the electrostatic repulsions and reducing aggregation phenomena during time. However, also the type of counter-ion affects the aggregation process: it has been demonstrated that by using methylsulfate as counter-ion of choline a slight aggregation of nanoparticles is induced. This process is strongly enhanced by introducing $Nilered^{+} - Methylsulfate$ ions. The presence of $Nilered^{+}$ upon nanoparticles surface is demonstrated by the detection of its emission spectrum: the excited chromophores of nanoparticles transfer their energy (through excitation energy transfer mechanism) to the nearest **Nilered** molecules and the result is an increasing of **Nilered** fluorescence. Due to the proximity of **Nilered** to the surface, the emission is blue-shifted compared to the emission of **Nilered** in water because of the lower polarity of the environment.

In the third part of the chapter we introduced another way for nanoparticle stabilization, called "Molecular Design". Two substitutes biphenyl bulky

groups are linked to the amine moiety instead of simple phenyl groups. This change of molecular structure allows to obtain very fast reprecipitation processes (few seconds) and good colloidal stability, as demonstrated by zeta-potential analysis. In this case nanoparticle suspensions are stable during weeks without the use of any additive.

# Chapter 4

# Organic Nanoassemblies for Energy and Electron Transfer

## 4.1 Introduction

Organic nanoassemblies are totally organic nanostructures composed by two or more types of molecules or polymers. They reached a growing attention in very recent years due to the possibility to combine functional properties of different compounds and to lead unique optical properties. The synergistic use of different chromophores (or polymers) permit to combine the opto-electronic characteristics of the single compounds, but also to obtain new properties through physical processes that can take place between molecules, such as excitation energy transfer (EET) or photoinduced electron transfer (PET). Some bi-component organic nanostructures called doped nanoparticles or nanowires, in which one compound acts as host and the other one as guest, able to show efficient energy transfer or electron transfer between the two dyes have been recently reported [114, 115, 116, 117, 118, 119]. In particular, these types of nanoparticles can be used in many different fields such as biological applications (contrasting agents for bioimaging), organic photovoltaic materials, luminescent materials, organic light emitting diodes

or organic waveguides.

Up to now, many different types of core@shell nanostructures have been prepared and studied including inorganic/inorganic [120, 121], inorganic-organic [122], organic-polymer [123] and polymer-polymer structures [124]. However, only few works report successful synthesis of core@shell nanostructures from two kinds of organic small molecules [125, 126, 127, 128]. The optical and electronic properties of this kind of new nanoassemblies are the object of intense research because of their distinctive differences from their inorganic counterpart, due to the different type of interactions that take place in soft matter.

This chapter is divided into two big parts: the first part is dedicated to the theoretical description of excitation energy transfer (EET) and photoinduced electron transfer (PET) mechanisms, while the second part focuses on the design, preparation and characterization of organic nanoassemblies engineered in order to exploit these two types of processes.

### 4.1.1 Excitation Energy Transfer

Excitation energy transfer (EET) is a phenomenon playing a key role in some natural processes such as photosynthesis, allowing for light harvesting and energy funneling towards the reaction center, or bioluminescence processes for the production of light [129, 130].

Exctitation energy transfer involves the transfer of energy from an excited molecule (called energy donor D) to a ground state molecule (called acceptor A) according to the expression:

$$D^* + A \rightarrow D + A^* \tag{4.1}$$

where the symbol * indicates the excited state of the molecule. The process can follow a radiative or non-radiative mechanism. The radiative mechanism is a two-step process in which one photon, emitted by the donor D, is

absorbed by the acceptor A:

$$D^* \rightarrow D + hv$$

$$hv + A \rightarrow A^* \tag{4.2}$$

Radiative energy transfer occurs when the distance between D and A is larger than the wavelength of the emitted photon, i.e. in the far field. Radiative transfer does not require any interaction between D and A, but it only depends on the spectral overlap between the emission spectrum of D and the absorption spectrum of A. Indeed, the consequences of this phenomenon include the quenching (in concentrated or thick samples) of donor emission in the region of the spectral overlap, with consequent distorsion of the emission spectrum due the inner filter caused by the absorption by the acceptor.

On the contrary, non-radiative energy transfer can occur only in presence of interactions between the donor and acceptor molecules and depends on their relative distance (discussed below). This second type of process also requires the spectral overlap between donor emission and acceptor absorption, but it is an one-step process in which a virtual photon is transferred between D* and A, occurring when the intermolecular distances are smaller than the wavelength of the virtual exchanged photon, i.e. in the near field. It must be pointed out that there are different types of interactions responsible for transfer, according to the distance between D and A molecules. At very short distances (smaller than about 10 Å) the interactions arise from intermolecular orbital overlap, and transfer occurs via an electron exchange mechanism also known as Dexter mechanism or charge resonance [131, 132]. When the distances are larger (10 - 100 Å), the Dexter mechanism can be neglected and Coulombic interactions become responsible for EET.

Förster proposed a simple model for the description of Coulombic EET at the end of the Fifties and for this reason the process is often named after "Förster resonance energy transfer" (FRET) [133, 134, 135, 136]. In this model, which is considered as a milestone in the field of energy transfer,

Coulombic intermolecular interactions are described in terms of the dipolar approximation. In particular, the interaction between the transition dipole moments of donor and acceptor is responsible for the transfer process, whose rate is defined by the Fermi Golden Rule:

$$k_{EET} = \frac{1}{\hbar^2 c} | < \psi_D^* \psi_A | V | \psi_D^* \psi_A > |^2 \delta \left( \widetilde{v}_D - \tilde{v}_A \right) \tag{4.3}$$

where $\hbar$ is the Plank constant divided by $2\pi$, $c$ is the speed of light, $\psi_A$ and $\psi_D$ are the ground-state wavefunctions, while $\psi_A^*$ and $\psi_D^*$ are the excited-state wavefunctions of the acceptor and the donor, respectively. $V$ is the interaction potential and the term $\delta \left( \widetilde{v}_D - \tilde{v}_A \right)$ accounts for the energy conservation. This last condition is satisfied when the emission spectrum of the donor overlaps the absorption spectrum of the acceptor as shown in Figure 4.1. If the term $V$ is described adopting dipolar approximation, the rate of the process reads [SI units]:

$$k_{EET} = \frac{1}{16\pi^2 \varepsilon_0^2 \hbar^2} \left( \frac{\mu_D^t \mu_A^t}{n^2 r^3} k \right)^2 \delta \left( \widetilde{v}_D - \tilde{v}_A \right) \tag{4.4}$$

where $\mu_A^t$ and $\mu_D^t$ are the transition dipole moments of the acceptor (absorption process) and donor (emission process) respectively, $\varepsilon_0$ is the vacuum permittivity, $r$ is the D-A distance, $n$ is the refractive index of the medium (screening the interactions between transition dipole moments) and $k$ is an orientational factor, that accounts for the mutual orientation of the transition dipole moments:

$$k = cos\theta_{DA} - 3cos\theta_D cos\theta_A \tag{4.5}$$

Angles $\theta_{DA}$, $\theta_D$ and $\theta_A$ are described in Figure 4.2. When energy transfer is measured is liquid or non-viscous solvents, where donor and acceptor are free to reorient more rapidly than the transfer occurs, the orientational value is found to be $k^2 = 2/3$, while if the molecules are randomly oriented in a

matrix where their rotations are hindered, such as frozen solvents or amorphous materials, the value of the orientational parameter is $k^2 = 0.476$. The transition dipole moment expressions for donor and acceptor are connected to the donor emission spectrum and the acceptor absorption spectrum [SI units, but if otherwise specified] [137]:

$$\left(\mu_D^t\right)^2 = \frac{3\varepsilon_0 \hbar \phi_D^0}{8\pi\tau_D^0} \int_0^\infty \frac{I_D(\tilde{v})}{\tilde{v}^3} d\tilde{v} \tag{4.6}$$

$$\left(\mu_A^t\right)^2 = \frac{3\ln 10 \hbar c \varepsilon_0}{10\pi N_A} \int_0^\infty \frac{\epsilon_A(\tilde{v})}{\tilde{v}} d\tilde{v} \tag{4.7}$$

where $\phi_D^0$ and $\tau_D^0$ are the fluorescence quantum yield and the lifetime of the donor in the absence of transfer, $I_D(\tilde{v})$ is the fluorescence spectrum of the donor normalized to get unit area, $\epsilon_A(\tilde{v})$ is the molar extinction coefficient of the acceptor [in units of $M^{-1}cm^{-1}$], $N_A$ is the Avogadro's number and $\tilde{v}$ is the wavenumber in units of $cm^{-1}$. The expression for EET rate, originally proposed by Förster [133] using these units reads:

$$k_{EET} = \frac{9 \times 10^{52} \ln 10}{1280\pi^5 N_A n^4} \frac{k^2 \phi_D^0}{\tau_D^0 r^6} \int_0^\infty \frac{\epsilon_A(\tilde{v})\, I_D(\tilde{v})}{\tilde{v}^4} d\tilde{v} \tag{4.8}$$

where $r$ is expressed in units of Å.

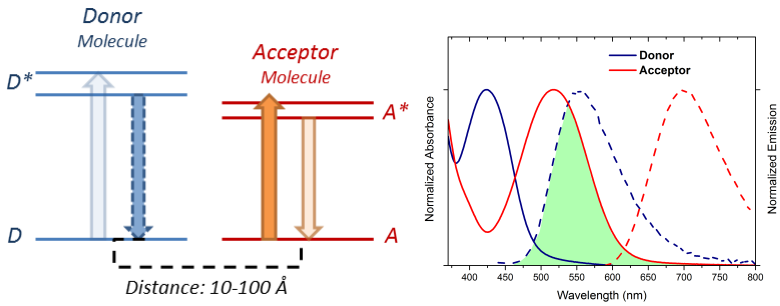


*Figure 4.1: Left panel: Energy level scheme of the donor D and acceptor A molecules showing resonant energy transfer (the emission of the donor is resonant with the absorption of the acceptor). Right panel: Spectral overlap between the emission spectrum of the donor and the absorption spectrum of the acceptor.*

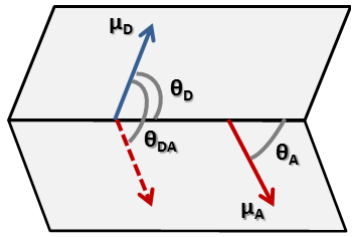


*Figure 4.2: Angles for the calculation of the orientational factor k.*

The Forster radius, $r_0$, is defined as the distance between donor and acceptor at which the transfer has an efficiency of 50% (transfer and spontaneous decay of the excited donor are equally probable $k_{EET} = 1/\tau_D^0$), is given (in Å) by:

$$(r_0)^6 = \frac{9 \times 10^{52} \ln 10 k^2 \phi_D^0}{1280 \pi^5 N_A n^4} \int_0^\infty \frac{\epsilon_A(\tilde{v})\, I_D(\tilde{v})}{\tilde{v}^4} d\tilde{v} \tag{4.9}$$

The transfer efficiency is defined as:

$$\phi_{EET} = \frac{k_{EET}}{k_{EET} + (\tau_D^0)^{-1}} = \frac{1}{1 + (r/r_0)^6} \tag{4.10}$$

For a D-A couple at fixed distance, the transfer efficiency can be experimentally evaluated in different manners by steady-state or time-resolved measurements [131] as reported below.

1. **Decrease of donor fluorescence.** The EET from donor to acceptor causes the decrease of the fluorescence quantum yield (or intensity) of the donor:

   $$\phi_{EET} = 1 - \frac{\phi_D}{\phi_D^0} \tag{4.11}$$

   where $\phi_D$ and $\phi_D^0$ are the fluorescence quantum yields of the donor in presence and absence of the acceptor, respectively.

2. **Comparison between absorption and excitation spectra.** This method is based on the comparison between absorption and excitation spectra when transfer takes place. The excitation spectrum is collected detecting only the emission of the acceptor. After normalization of the excitation band of the acceptor to the absorption spectrum, the transfer efficiency is estimated as:

   $$\phi_{EET} = \frac{I(\lambda_D)}{A(\lambda_D)} \tag{4.12}$$

   where $I(\lambda_D)$ is the maximum intensity of the excitation band related to the donor and $A(\lambda_D)$ is the absorbance at the same wavelength. In the case of total transfer ($\phi_{EET} = 1$) it is clear that the absorption spectrum coincides with the excitation profile.

3. **Enhancement in acceptor fluorescence**. The emission of the acceptor increases in presence of EET. The transfer efficiency can be

evaluated as:

$$\phi_{EET} = \frac{A_A(\lambda_{ex})}{A_D(\lambda_{ex})} \left( \frac{I_A}{I_A^0} - 1 \right) \tag{4.13}$$

where $A_A(\lambda_{ex})$ and $A_D(\lambda_{ex})$ are the absorbance of the acceptor (A) and of the donor (D) at the excitation wavelengths, respectively and $I_A$ and $I_A^0$ are the fluorescence intensities of the acceptor in presence and absence of the donor, respectively.

4. **Decrease of donor lifetime.** The most efficient method to determine the efficiency of EET is based on the decay of donor fluorescence and it can be estimated from the decay time (or the average of decay times) of the donor in absence and in presence of the acceptor:

$$\phi_{EET} = 1 - \frac{< \tau_D >}{< \tau_D^0 >} \tag{4.14}$$

### 4.1.2 Photoinduced Electron Transfer

Electron transfer is one of the most important and studied mechanisms in photosynthesis, organic reactivity and optoelectronic devices. An electron transfer process involves the transfer of an electron from a donor to an acceptor. The transfer can take place between two different parts of a molecule linked by a bridge (intramolecular) or between two different compounds (intermolecular). The process can be activated thermally or photochemically; in this last case is named photoinduced electron transfer (PET).

An electron donor is typically a molecular material with a small electron affinity (p-type), while the electron acceptor is topically a material with high electron affinity (n-type). PET involves firstly the absorption of a photon in the region of UV or visible light to create the excited donor species $D^*$ able to initiate the electron transfer to the electron acceptor (A). A general

PET reaction is given by:

$$\begin{cases} D + h\nu \rightarrow D^* \\ D + A \rightarrow D^+ + A^- \end{cases} \tag{4.15}$$

where $D^*$ is the photo-excited donor and $D^+$, $A^-$ the charged species.

Subsequent to the electron transfer, a charge transfer state is created consisting of the radical cation of the donor and the radical anion of the acceptor bound by Coulombic interactions, also called exciton (equation 4.15). After the formation of the charge transfer state, a process suitable for optoelectronic devices, such as photovoltaic cells, is the separation of charges and charge transport towards the electrodes. Unfortunately, a very common process that can follow the formation of excitons is charge recombination, leading back to the initial condition.

## 4.2 Organic Nanoassemblies for Excitation Energy Transfer

Inorganic and hybrid semiconductor- or metallic-based nanomaterials have been object of intense research in the last decades due to their unique photonic and electronic properties and related applications [138, 139, 140, 141, 142]. In such particles, surface effects [143], as well as morphology [144], play a major role and are exploited to tune and enhance photoluminescence, and more generally improve optical and electronic properties [145, 146].

On the other hand, the study on organic nanoassemblies is a very recent field of research which has reached a growing attention only in the last years. Indeed, fluorescent organic nanoparticles may present several advantages (ease of preparation, reduced cost and toxicity, versatility, degradability...) in comparison to the inorganic counterpart and, for these reasons, have motivated many studies for lighting and imaging purposes [147, 148, 149, 17].

### 4.2.1 Doped Binary Nanostructures

Excitation energy transfer in doped (host-guest) organic nanostructures has been observed in literature in different systems [114, 115, 116, 117]. In these complex nanostructures there are the sinergetic effects of the EET and solid-state solvatation that both allow to tune the luminescence of the nanoparticles towards longer wavelengths and increase the luminescence of the acceptor. Since in doped nanoparticles the guest acceptor molecule is found to be in a "frozen" environment composed by donor host molecules, the polarity of the medium in the environment of the guest is determined by the polarity of donor molecules or the mix of donor/acceptor molecules. When the acceptor guest is a push-pull chromophore, its emission wavelengths can vary in accordance to the average polarity of its environment, in particular the emission typically shifts towards red wavelengths by increasing medium polarity.

In this section some example of different doped binary nanostructures are reported:

1. **TW1** nanoparticles doped with compound **TW3**;
2. **T1** nanoparticles doped with **Nilered**;
3. **T5** nanoparticles doped with compound **T4**.

The couples are chosen because of the good overlap between the emission spectrum of the energy donor (host compound) and the absorption spectrum of the energy acceptor (guest compound), as reported in Figure 4.3, in order to obtain a good EET rate. The chemical structures of the compounds **T1**, **T4**, **Nilered**, and the properties of their nanoparticles are reported in Chapter 1, while the chemical structures and properties of compounds **TW1** and **TW3** are reported in Chapter 3 (all the molecular structures are also resumed in Appendix 1). The characteristics of **T5** chromophore [95] are reported in Appendix 3.

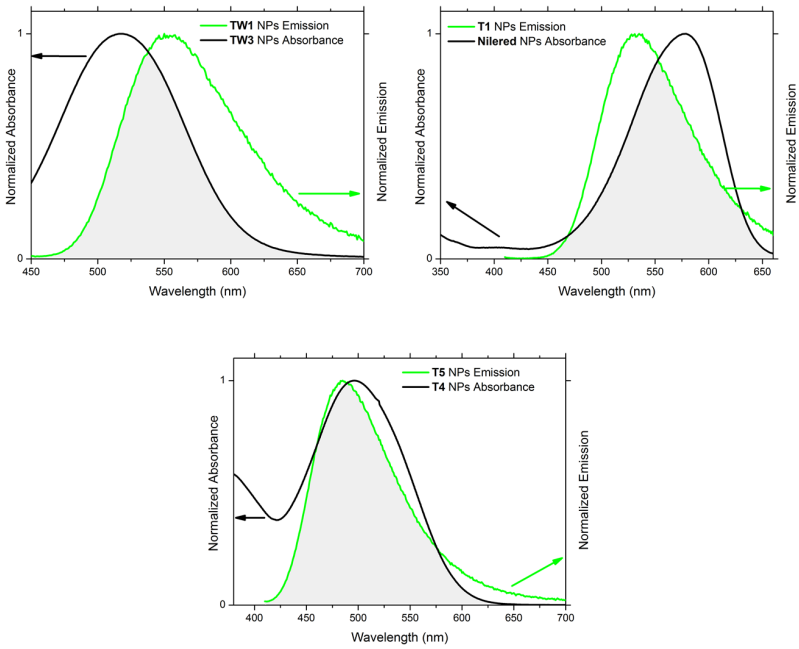


*Figure 4.3: Absorption spectra of host NPs (black lines) and emission spectra of guest NPs (red lines), and corresponding overlaps (grey areas).*

#### 4.2.1.1 Preparation of Doped Nanoparticles: "one step" Process

Doped nanoparticles are prepared through the classical reprecipitation method in a "one step" process. Stock solutions of host and guest molecules (in THF) are mixed together. A known amount of the obtained solution is added to a defined quantity of distilled water under vigorous stirring at room temperature. When no changes are detected any more in the UV-Vis spectrum of the system the reprecipitation can be considered as terminated. The method is called "one step" because the stock solutions of the two chromophores are mixed together before the addition in water, so that both molecules are present at the same time in the solution during the reprecipitation process .

#### 4.2.1.2 TW3-doped TW1 nanoparticles

**TW1** and **TW3** are push-pull dipolar chromophores designed in order to achieve stable colloidal nanoparticles (as reported in Chapter 3). Doped nanoparticles are obtained using **TW1** as host (energy donor) and **TW3** as guest (energy acceptor) with doping percentages of 1%, 2% and 4%. The emission spectra of the suspensions obtained by exciting at 420 nm are reported in Figure 4.4, panel A. Because of the very efficient energy transfer between the two molecules, doped nanoparticles display a very good fluorescence in the region of the acceptor emission when the donor (**TW1**) is excited at 420 nm. The residual donor fluorescence (maximum at about 550 nm) is very low for 1%-doped NPs and it is almost completely quenched for 4%-doped NPs. The observed red-shift of emission, from 624 nm to 639 nm for 1%-doped and 4%-doped respectively, is due to the slight change of the polarity of the environment. In fact by varying the concentration of **TW3**, which is more polar than **TW1**, the polarity of the medium around acceptor molecules increases and, consequently, its emission red-shifts. A very similar behavior is observed when the acceptor is directly excited (at 520 nm). This is an evidence of the uniformity of the medium around the acceptor molecules. The increase of luminescence observed in this case for increasing doping percentage is simply due to the increased acceptor amount.

These nanoparticles are stable in water for weeks (no precipitation or aggregation takes place).

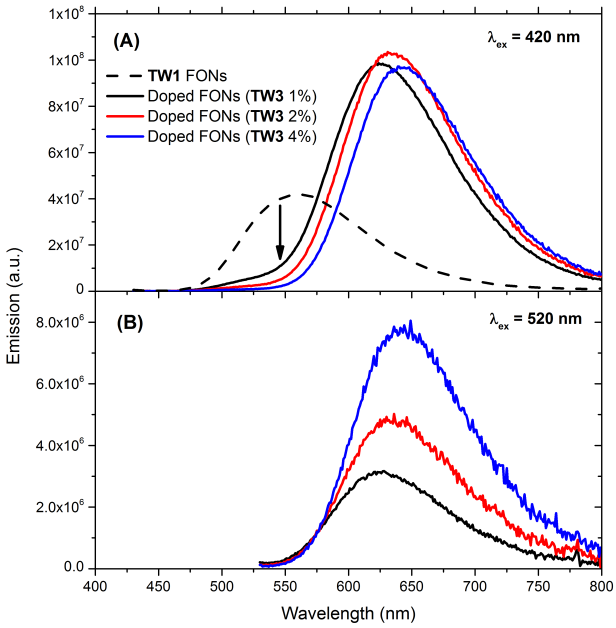


*Figure 4.4: Emission spectra from freshly prepared doped nanoparticles (**TW1** host and **TW3** guest) excited at 420 nm (panel A) and excited at 520 nm (panel B).*

#### 4.2.1.3 Nilered-doped T1 Nanoparticles

In Chapter 1 we reported the preparation of nanoparticles from **Nilered** and, in particular, we focused the attention on their extremely low colloidal stability (few minutes). Accordingly to these results, it is not possible to obtain pure **Nilered** nanoparticles from simple reprecipitation process. Furthermore, the luminescence of pure **Nilered** NPs is very low (quantum yield $<1\%$). In Chapter 1 the morphological and spectroscopic characterizations of **T1** nanoparticles were also reported.

Doped nanoparticles obtained using **T1** as host (energy donor) and **Nilered** as guest (energy acceptor) with three different percentages (0.5%, 1.0% and 10% respectively) of guest chromophore are prepared using the "one step" process described above. The emission spectra of the obtained nanostructures are reported in Figure 4.5. The fluorescence spectra of doped nanoparticles show a decrease on donor emission (**T1**), for increasing **Nilered** concentration, in agreement whit an efficient EET taking place between the two chromophores. **Nilered** emission appears as a intense band at about 600 nm and its emission shifts towards longer wavelengths in accordance to the increase of environment polarity: as the **Nilered** concentration grows also the medium polarity grows (because **Nilered** is more polar than **T1**). For increasing **Nilered** concentration a quenching of fluorescence intensity is observed probably because of the presence of non-radiative decays pathways induced by $\pi$-$\pi$ stacking. This last result is also in accordance with the fact that **Nilered** NPs have very low fluorescence quantum yield. It has been observed that these doped nanoassemblies have about the same colloidal stability as pure **T1** nanoparticles (few days).

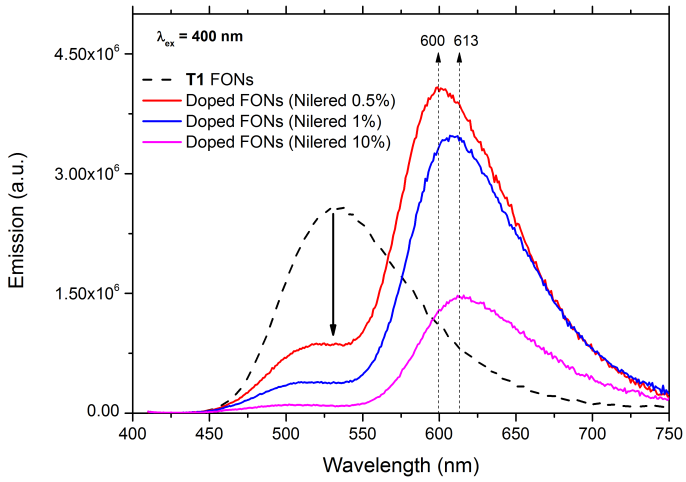


*Figure 4.5: Emission spectra from doped nanoparticles (**T1** host and **Nilered** guest compounds) after preparation, excited at 400 nm.*

#### 4.2.1.4 T4-Doped T5 Nanoparticles

Another example of EET between host and guest molecules in binary nanostructures is given by the doped nanostructures composed by the dipolar chromophore **T5** [95] and the octupolar chromophore **T4** (described in Chapter 1). Doped nanoparticles are obtained using **T5** as host (energy donor) and **T4** as guest (energy acceptor) whit a percentage of 1%. The emission spectra of suspensions obtained by exciting at 400 nm are reported in Figure 4.6. The donor emission decreases of about 50%, while the acceptor emission increases and shifts towards shorter wavelengths (maximum at about 600 nm) compared to the emission of **T4** FONs (maximum at about 700 nm). This behavior can be ascribed to solid-state solvation: the environment around guest molecules in doped nanostructures is less polar compared to the environment around molecules in **T4** FONs because of the different polarity of **T4** and **T5** compounds. The effect of polarity of the medium explains the acceptor blue-shift and the presence of efficient EET gives account of the fluorescence quenching of donor and the fluorescence enhancement of acceptor. Another evidence that efficient energy transfer takes place between the two chromophores is the fluorescence excitation spectrum of the system registered collecting the emission signal of the suspension at 610 nm (where the fluorescence of **T5** is negligible compared to that of **T4**) whose shape is very close to the absorption profile (Figure 4.7).

Transmission electron microscopy images of doped nanostructures, collected at the end of the reprecipitation process and using uranyl acetate as contrasting agent, reveal that they are not regular in shape and quite aggregated; the average diameter is about 30 nm with a quite high polidispersity (Figure 4.8).

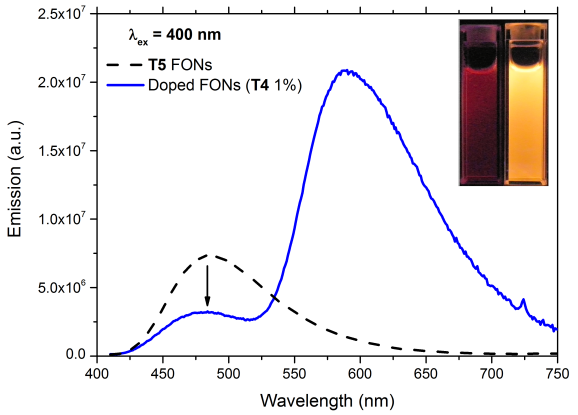


*Figure 4.6: Emission spectra from freshly prepared doped nanoparticles (**T5** host and **T4** guest compounds) excited at 400 nm. Inset: image of **T4** FONs suspension (left) and doped FONs suspension (right) under UV lamp (excitation wavelength: 380 nm).*

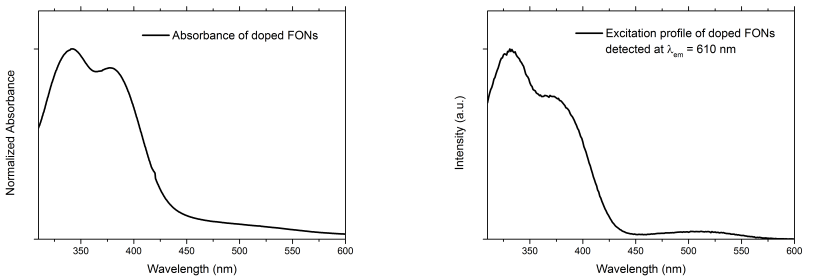


*Figure 4.7: Absorption (left) and excitation (right) spectra of 1% doped FONs. The fluorescence signal is collected at 610 nm. The difference in shape between the two spectra can be attributed (at least in part) to the effect of scattering, clearly visible in red-wavelengths region of the absorption spectrum. The similarity between excitation and absorption spectra is a clear evidence of efficient energy transfer between the two compounds (**T4** and **T5**).*

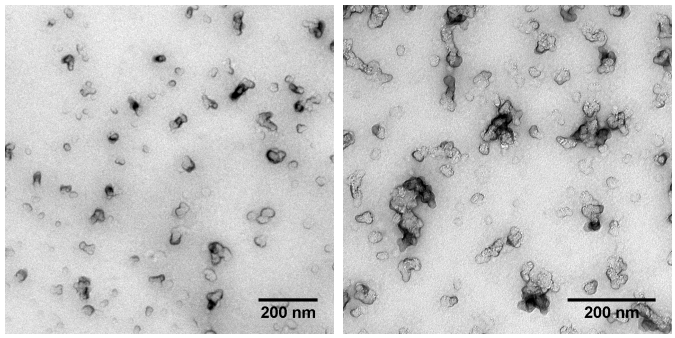


*Figure 4.8: TEM images of **T4**-doped **T5** nanoparticles.*

### 4.2.2 Core@Shell Binary-Nanostructures

Very recent works focus on excitation energy transfer in hybrid organic-inorganic core@shell silica nanostructures [150, 151] and the microemulsion synthesis of core@shell organometallic-organic nanoparticles has been reported, using an Iridium complex as core and perylene molecules as shell [152]. EET has also been demonstrated in polymer-based [153, 154] or amphiphile nanoparticles [155], as well as in organic core/diffuse-shell nanorods [156]. However, the study of organic core@shell nanoassemblies composed only by two organic molecules is a totally new field of research [18]. In this section, the preparation and the morphological and spectroscopic characterization of some molecular-based core@shell nanostructures are reported. In particular, we focus the attention on the luminescence-enhancement from chromophores caused by the spatial confinement of luminescence in a special boundary region where large local fields are created at the interface between core and shell sections, where the EET process takes place. In fact, when the starting chromophores are polar or polarizable, they are liable to generate significant electric fields in their close proximity, so that sizable local fields may be expected at the surface of the nanoparticles and, even more importantly (due to the lower dielectric constant of organic materials compared to water), at the interface between nanomaterials.

In this section some examples of different core@shell nanoassemblies obtained using the same chromophores as for doped-nanostructures are reported:

1. **TW3@TW1** nanoparticles;
2. **Nilered@T1** nanoparticles;
3. **T5@T4** nanoparticles.

#### 4.2.2.1 Preparation of Core@Shell Nanoparticles: "multi step" Process

Core@shell nanoparticles are prepared through a "two-step" reprecipitation method: first core nanoparticles are precipitated in water by adding a known amount of a 1 mM THF solution of the first chromophore to bidistilled water under vigorous stirring; subsequently a know amount of a 1 mM THF solution of the second chromophore is added to core-NPs aqueous suspension under stirring, to create a shell of the second dye on top of the core.

The formation of core@shell nanoparticles follows the same rules of standard nucleation: when a stock solution of the shell compound is added to the core suspension the supersaturation is reached for the shell compound and cores act as seeds of growth. Simply driven by hydrophobic interactions, the shell molecules will settle on the surface of the core nanoparticles allowing the formation of a small layer, called shell layer [18].

#### 4.2.2.2 TW3@TW1 Core@Shell Nanoparticles

**TW1@TW3** nanoparticles are prepared using **TW3** compound as core (energy acceptor) and **TW1** as shell (energy donor) to obtain a final nominal concentration of $1 \times 10^{-5}$M for both compounds. To gain additional information, we also investigate "composite" nanoparticles obtained in a one-step procedure from a common solution of the two chromophores: stock solutions of compounds **TW1** and **TW3** in THF are mixed together and a small amount of the mixed solution is added to bidistilled water under vigorous stirring (the final nominal concentration of dyes are the same of core@shell structures, i.e. $1 \times 10^{-5}$M). The spectroscopic and morphological properties of obtained suspension are reported in Table 4.1 and in Figures 4.9 and 4.10.

*Table 4.1: Spectroscopic properties and zeta-potential values for the prepared **TW1/TW3** nanostructures in water suspension.*

| | $\lambda_{abs}^{max}$ [nm] | $\lambda_{em}^{max}$ ($\lambda_{ex}$=420 nm) [nm] | $\lambda_{em}^{max}$ ($\lambda_{ex}$=520 nm) [nm] | $\Phi^{a}$ ($\lambda_{ex}$=420 nm) | $\Phi^{a}$ ($\lambda_{ex}$=520 nm) | Zeta-Potential [mV] |
|---|---|---|---|---|---|---|
| **TW3 FONs** | 517 | 697 | 697 | 0.06 | 0.06 | - 36 ± 3 |
| **TW1 FONs** | 424 | 552 | - | 0.07 | - | - 46 ± 1 |
| **Composite TW1/TW3 FONs** | 429, 523 | 684 | 684 | 0.11 | 0.11 | - 45 ± 2 |
| **Core@shell TW3@TW1 FONs** | 419, 517 | 631 | 696 | 0.20 | 0.07 | - 46 ± 2 |

*[a] Fluorescence quantum yield measured using an integrating sphere in center-mount sample holder configuration*

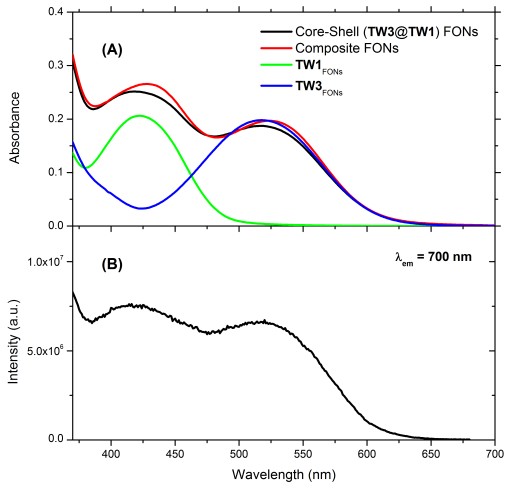


*Figure 4.9: Panel A: Absorption spectra of aqueous suspensions of **TW3** FONs (blue line), **TW1** FONs (green line), composite FONs (red line) and core@shell **TW3@TW1** FONs (black line). Panel B: Fluorescence excitation spectrum of the core@shell **TW3@TW1** FONs for detection at 700 nm.*

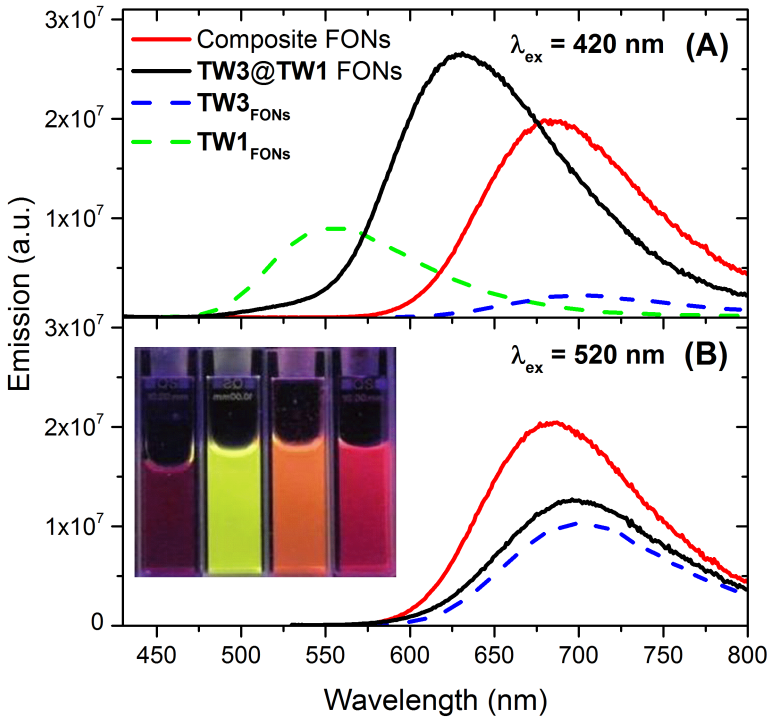


*Figure 4.10: Photoluminescence spectra of all the **TW1/TW3** nanoparticles for excitation at 420 nm (A) and at 520 nm (B). Inset: from left to right: **TW3** FONs, **TW1** FONs, core@shell **TW3@TW1** FONs and composite FONs suspensions observed under UV-lamp ($\lambda_{ex}$ = 340 nm) [18] .*

The shape and dimension of the nanoparticles are investigated by transmission electron microscopy using uranyl acetate as staining agent, and by dynamic light scattering (DLS). Figure 4.11 reports the TEM images of **TW3**, core@shell and composite FONs and their distribution analyses. All types of nanoparticles are round in shape and fairly polydispersed. DLS measurements reveal that the average diameter is about 70 nm for **TW3** FONs,

65 nm for composite nanoparticles, and 80 nm for core@shell nanoparticles (Table 4.2).

The average diameter of core@shell FONs, larger than that of pure **TW3** FONs, is a first hint that the two-step precipitation process promotes the formation of an external layer of **TW1** (about 5 nm thick) on top of the firstly precipitated core of **TW3** FONs. In order to evaluate if a fraction of **TW3** FONs remains uncovered during the deposition step of the layer of **TW1**, zeta-potential analysis has been performed. In our case, all the nanoparticles have negatively charged surfaces (Table 4.1), with values lower than -30 mV, indicative of good colloidal stability [157]. Indeed, all nanoparticle suspensions are stable over weeks without aggregation neither precipitation taking place. Pure **TW1** and core@shell FONs show about the same zeta-potential (-46 mV), sensibly different from the zeta-potential value measured for pure **TW3** FONs (-36 mV). This is a strong confirmation that the surface of the nanoparticles prepared by the two-step process is mostly composed of molecules **TW1**, i.e. the structure is likely to be of core@shell type (**TW3@TW1**).

Additional confirmation of the core@shell structure is provided by the investigation of the luminescence properties. Absorption spectra of the binary nanoparticles correspond quite well to the sum of the absorption spectra of **TW3** FONs and **TW1** FONs (Figure 4.9, panel A). Binary nanoparticles show quite interesting luminescence characteristics. When exciting composite nanoparticles at 520 nm (where only **TW3** absorbs, see Figure 4.9), the luminescence spectrum is blue-shifted by 13 nm with respect to that of **TW3** FONs (Table 4.1). This shift indicates that **TW3** molecules in the composite nanoparticles experience a different environment (i.e. less polar) than in pure **TW3** FONs, providing evidence of the presence of **TW1** molecules (having lower dipole moment and polarizability than **TW3**). In addition, a significant (almost twofold) enhancement of the fluorescence quantum yield is observed in such composite nanoparticles.

In contrast, in the case of binary nanoparticles prepared via the two-

step procedure, the emission spectrum excited at 520 nm (direct excitation of **TW3**) and the corresponding quantum yield are quite similar to that of pure **TW3** FONs. This is an additional evidence of the core@shell nature of these nanoparticles, where **TW3** molecules constitute the core.

When exciting the two types of binary nanoparticles at 420 nm (where mainly chromophore **TW1** absorbs, Figure 4.9), the emission of **TW1** centered at 550 nm is almost completely quenched, while the emission band in the red region is strongly enhanced (Figure 4.10, panel A). This is a clear confirmation of the intimate bicomponent nature of both types of FONs, as well as the signature of efficient EET within the nanoparticles, chromophore **TW1** acting as the energy donor and chromophore **TW3** as the energy acceptor. The fluorescence excitation spectrum measured when detecting the luminescence at 700 nm (Figure 4.9B) gives a definite proof of the (highly efficient) EET from **TW1** to **TW3**: the excitation profile is characterized by two bands, corresponding to the absorption band of the acceptor (centered at 525 nm) and of the donor (centered at 425 nm), and is practically superimposable to the absorption spectrum of the core@shell nanoparticles.

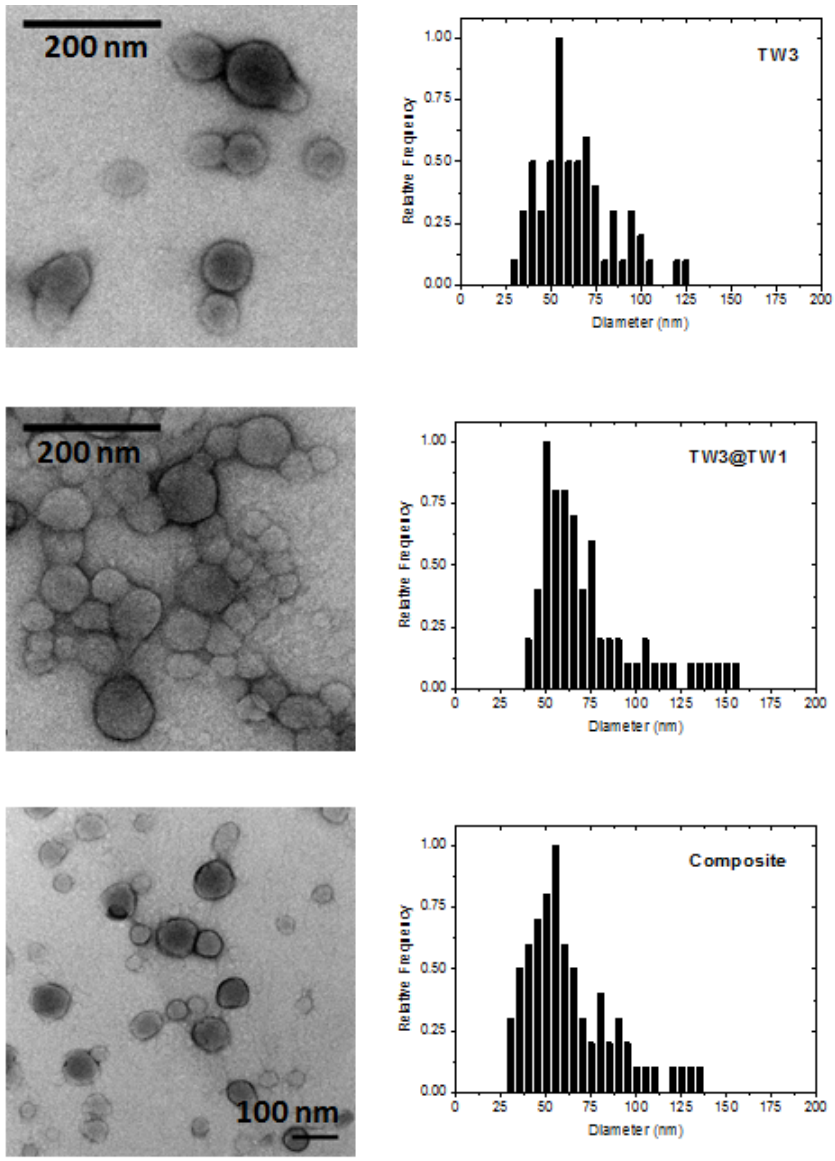


*Figure 4.11: TEM images of* ***TW3@TW1*** *freshly prepared nanoparticles (left) and corresponding distribution analyses (right).*

*Table 4.2: Average diameter of the different FONs based on **TW1** and **TW3** as obtained via DLS and TEM.*

| | Average diameter from DLS [nm] | Average diameter from TEM [nm] |
|---|---|---|
| TW3 FONs | 70.3 | 64 |
| TW1 FONs | 64.1 | 55 |
| Composite TW1/TW3 FONs | 79.8 | 70 |
| Core@shell TW3@TW1 FONs | 65.0 | 60 |

Strikingly, whereas the photoluminescence characteristics of composite nanoparticles remain unchanged with respect to what observed when directly exciting acceptor **TW3** at 520 nm, the photoluminescence maximum of the core@shell **TW3@TW1** nanoparticles (631 nm) is significantly blue-shifted (65 nm). This behavior can be explained based on a directional EET process in connection with the layered structure of the core@shell nanoparticles (Figure 4.12).

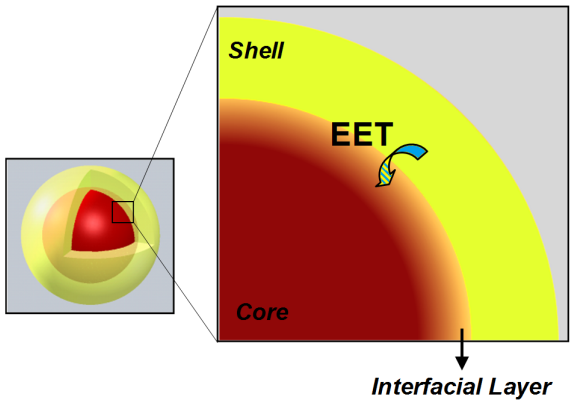


*Figure 4.12: A sketch of the core@shell structure and (zoom) of the proposed mechanism of energy transfer at the shell-to-core nanointerface [18].*

In fact, the core, prepared in the first step of synthesis, is composed by **TW3** molecules, while **TW1** molecules, added during the second step, form a shell around the core. When the binary **TW3@TW1** nanoparticles are irradiated at 420 nm, the excited donor molecules in the shell transfer their excitation energy to acceptor molecules in the core. The probability of the EET transfer increases as the inverse sixth power of the donor-acceptor distance, so that it is maximized at the shell-to-core interface, where chromophores are closer. The emission observed when exciting at 420 nm is mainly confined to **TW3** molecules lying at the nanointerface with the shell: this justifies the different emission as compared to direct excitation of core chromophores. Indeed, when irradiating at 520 nm, all core molecules can be excited, so that all of them may emit and the emission of **TW3** FONs is basically recovered. The specific nature of the emitting zone of the core@shell nanoparticles is responsible for the marked blue shift and the strong enhancement of the acceptor emission, both with respect to **TW3** FONs and composite FONs (Table 4.1). Indeed the luminescence quantum yield increases from 0.06 in **TW3** FONs to 0.11 in composite FONs to 0.20 in core@shell nanoparticles (i.e. a more than threefold increase). This remarkable effect is thus directly related to the nanointerface between **TW3** and **TW1** in core@shell FONs. Most probably, sizable local electric fields (alike interface potentials) are generated at the interface between the core and shell which, in turn, are responsible for luminescence enhancement [158, 159, 160].

To further confirm the spatial confinement of the excitation transferred by EET in the core@shell nanoparticles, different donor/acceptor ratios are investigated: corresponding emission spectra are reported in Figure 4.13.

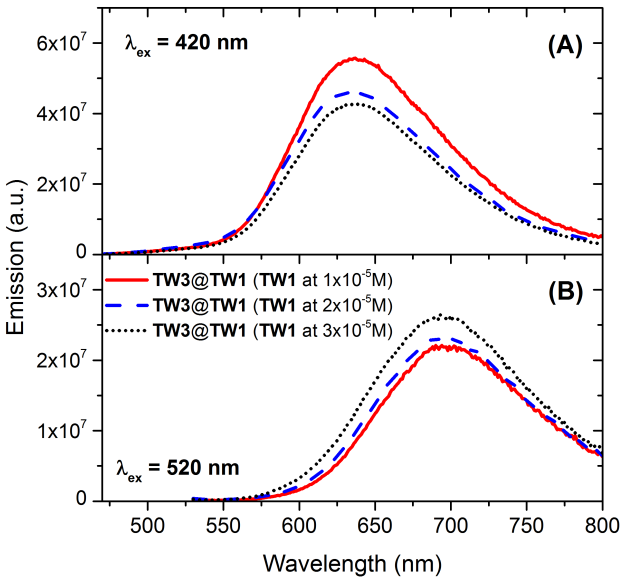


*Figure 4.13: Emission spectra of core@shell nanoparticles with constant concentration of acceptor (core chromophore **TW3**, $1 \times 10^{-5} M$) and different concentrations of donor (shell chromophore **TW1**, see legend). Panel A: Emission spectra for excitation at 420 nm. Panel B: emission spectra for excitation at 520 nm. The raw emission spectra have been divided by the corresponding absorbance measured at the excitation wavelength [18].*

In particular, **TW3@TW1** nanoparticles with a fixed concentration of **TW3** and a variable concentration of **TW1** are prepared. In that way the average dimension of the core (constituted by the acceptor **TW3** molecules) is expected to be the same for all of the samples, independently of the donor amount: only the thickness of the shell is expected to change. Therefore, the core-to-shell interface (and interface area) is expected to be the same independently of the donor/acceptor ratio, so that the energy-transfer mechanism and efficiency are expected to be virtually independent of the

donor amount (shell thickness). As a matter of fact, spectra reported in Figure 4.13 (raw intensities divided by the corresponding absorbance at the excitation wavelength) show that not only emission spectra measured upon direct excitation of the acceptor, but also the emission spectra obtained by excitation of the donor and subsequent EET are almost independent on the donor/acceptor ratio. The very small variations observed in the intensities can safely be ascribed to increasing inner-filter effects for increasing shell thickness.

To fully characterize EET, the photoluminescence dynamics is investigated. The fluorescence decays are found to be three-exponential for all nanoparticles, whatever the excitation or emission wavelengths (Table 4.3).

*Table 4.3: Fluorescence lifetimes of the prepared nanoparticles based on **TW1** and **TW3** in water suspensions and, in parentheses, corresponding fractions of the fluorescence decays. ND = not detectable (the emission signal is too weak to be detected).*

| | For $\lambda_{ex}$ = 405 nm | | | | | |
|---|---|---|---|---|---|---|
| | $\lambda_{em}$ = 525 nm | | | $\lambda_{em}$ = 700 nm | | |
| | $\tau_1$ [ns] | $\tau_2$ [ns] | $\tau_3$ [ns] | $\tau_1$ [ns] | $\tau_2$ [ns] | $\tau_3$ [ns] |
| TW3 FONs | - | - | - | 0.77 (0.23) | 2.87 (0.69) | 8.38 (0.08) |
| TW1 FONs | 0.35 (0.37) | 1.28 (0.43) | 3.62 (0.20) | 0.91 (0.28) | 3.78 (0.56) | 9.20 (0.16) |
| Composite TW1/TW3 FONs | ND | ND | ND | 1.10 (0.14) | 4.00 (0.72) | 10.70 (0.14) |
| Core@shell TW3@TW1 FONs | 0.21 (0.60) | 1.00 (0.32) | 4.00 (0.08) | 2.24 (0.22) | 6.43 (0.68) | 20.72 (0.10) |

We have selected two excitation wavelengths, 405 and 560 nm, corresponding to (quasi)selective excitation of donor (**TW1**) or acceptor (**TW3**), respectively. When binary nanostructures are excited at 560 nm and fluorescence decays measured at 700 nm (corresponding to direct excitation and emission of **TW3**), the lifetime of the core@shell nanoparticles remains almost unchanged with respect to **TW3** FONs (further confirming their core

nature). In contrast, the photoluminescence lifetime increases in composite nanoparticles, in relation with the less polar environment experienced by **TW3** chromophores in composite nanoparticles. When exciting at 405 nm (where mainly **TW1** absorbs), we selected two different detection wavelengths, 525 and 700 nm, corresponding to donor and acceptor emission maxima, respectively. The average donor lifetime (detection at 525 nm) decreases by about 50% for core@shell nanoparticles with respect to **TW1** FONs, and could not be estimated for composite nanostructures because the corresponding emission was too weak to be reliably detected. On the other hand, when detecting at 700 nm, an increase of the average acceptor lifetime is observed both for composite and core@shell nanoparticles (about 1.6 and 2 times, respectively). The marked shortening of the donor luminescence lifetime and concomitant lengthening of the acceptor luminescence lifetime in both composite and core@shell nanoparticles provide nice confirmation of the efficient EET between **TW1** and **TW3** in the binary nanostructures.

From the point of view of stability, no significant changes are detected on core@shell nanoparticles morphology after five weeks. The suspension is still transparent to the naked eyes and no aggregates can be detected, as confirmed by TEM images collected after five weeks (Figure 4.14). The average diameter of "aged" nanoparticles is still 70 nm, that is the same value found for freshly prepared nanoassemblies.

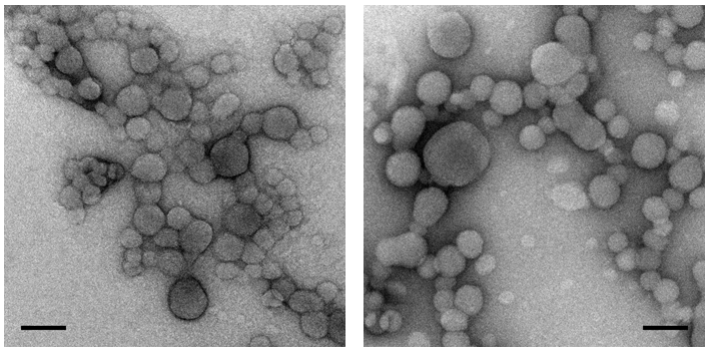

*Figure 4.14: Images by TEM of core@shell **TW3@TW1** nanoparticles after preparation (left) and after 5 weeks (right). Scale bar = 200 nm.*

A further confirmation of the proximity of **TW3** and **TW1** in core@shell assembly is provided by the mix of **TW1** and **TW3** nanoparticles suspensions. As expected, no EET is observed when suspensions of **TW1** FONs and **TW3** FONs are mixed together (Figure 4.15) due to the large mean distance between nanoparticles in the mixed suspension.

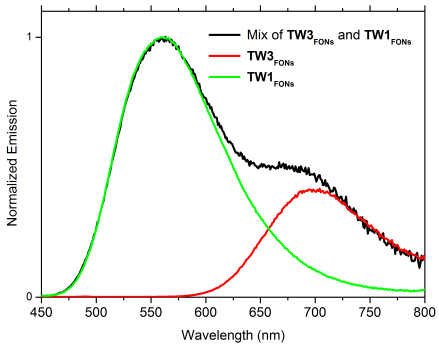


*Figure 4.15: Emission spectra of **TW3** FONs (red line), **TW1** FONs (green line) and of the mix of the two suspensions (black line), at the same nominal concentration, for excitation at 420 nm [18].*

#### 4.2.2.3 Nilered@T1 Core@Shell Nanoparticles.

**Nilered@T1** nanoparticles are prepared using the same preparation method described above. The results obtained from this couple are qualitatively very similar to those obtained using chromophores **TW1** and **TW3**. The spectroscopic properties of the obtained suspensions are reported in Figure 4.16 and Table 4.4.

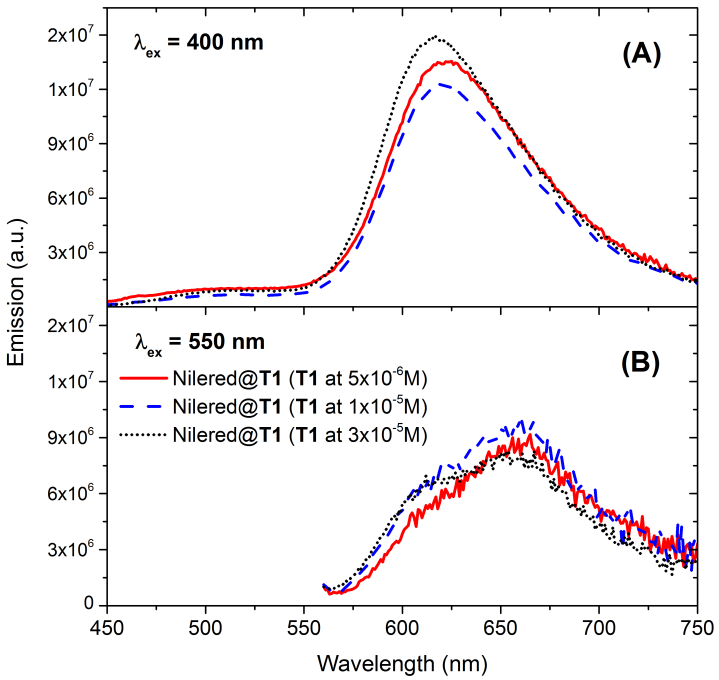


Figure 4.16: *Emission spectra of core@shell nanoparticles with constant concentration of acceptor (core chromophore* ***Nilered****,* $1 \times 10^{-5} M$*) and different concentrations of donor (shell chromophore* ***T1****, see legend). Panel A: Emission spectra for excitation at 400 nm. Panel B: emission spectra for excitation at 550 nm. The raw emission spectra have been divided by the corresponding absorbance measured at the excitation wavelength.*

*Table 4.4: Spectroscopic properties for the prepared nanostructures based on **T1** and **Nilered** in water suspension.*

| | $\lambda_{abs}^{max}$ [nm] | $\lambda_{em}^{max}$ [nm] ($\lambda_{ex}$=400 nm) | $\lambda_{em}^{max}$ [nm] ($\lambda_{ex}$=500 nm) |
|---|---|---|---|
| Nilered FONs | 578 | ~ 660 | ~ 660 |
| T1 FONs | 418 | 538 | 538 |
| Nilered@T1 FONs (T1 at $5x10^{-6}$ M) | ~ 410 | 623 | ~ 660 |
| Nilered@T1 FONs (T1 at $1x10^{-5}$ M) | ~ 410 | 619 | ~ 660 |
| Nilered@T1 FONs (T1 at $3x10^{-5}$ M) | ~ 410 | 617 | ~ 660 |

The emission signal of the donor (**T1**) is strongly quenched in the binary core@shell nanosystem, while the emission signal of the acceptor (**Nilered**) is enhanced because of the efficient EET process that takes place at the interface of core@shell nanostructures. In particular, as already evidenced for **TW1** and **TW3** nanoassemblies, it is possible to observe that the emission maximum (from **Nilered**) is practically independent of the donor concentration when the acceptor concentration is kept fixed. As the concentration of acceptor does not change, the average core dimension also does not change, so that the interfacial surface (which is the site where EET occurs) remains the same independently of donor concentration, i.e. of the final diameter of core@shell nanoassemblies. This is the reason why neither the emission wavelength nor the intensity significantly change with the concentration of donor, confirming what already reported.

However it must be pointed out that core@shell **Nilered@T1**, unlike **TW3@TW1**, are not stable during time. After some days nanoparticles precipitate: as expected, their colloidal behavior is very similar to that of **T1** nanoparticles.

#### 4.2.2.4 T4@T5 Core@Shell Nanoparticles.

**T4@T5** nanoparticles are prepared using **T4** dye for core (energy acceptor), which is an octupolar large molecule, and **T5** chromophore (energy donor) using the same preparation method described above. The final nominal concentration of both compounds is $2 \times 10^{-5}$M. The spectroscopic and morphological properties of the obtained suspensions are reported in Table 4.5 and in Figures 4.17 and 4.18.

The emission spectrum of the **T4@T5** system (when excitation wavelength is fixed at 400 nm) shows a strong quenching of donor fluorescence compared to the fluorescence spectrum of **T5** FONs at the same concentration (Figure 4.18, panel A), while the acceptor emission is blue-shifted and its intensity is enhanced (Table 4.5). The quantum yield ($\Phi$) of **T4@T5** suspension is 0.15, which is more than twice of quantum yield of **T4** FONs and five folds that of **T5** FONs. This clearly indicates that the energy transfer in these type of nanoassemblies promotes the enhancement of emission intensity. If the core@shell suspension is excited at 500 nm (where only **T5** absorbs) the observed emission has about the same maximum wavelength as **T5** FONs. The excitation profile of the core@shell FONs, measured when detecting the luminescence at 640 nm (at this wavelength the emission comes mostly from **T5**, Figure 4.17, panel B), is characterized by a very similar profile as the absorption spectrum; this gives another evidence of very efficient EET from **T5** to **T4**.

*Table 4.5: Spectroscopic properties of the prepared nanostructures based on **T4** and **T5** in water suspension.*

| | $\lambda_{abs}^{max}$ [nm] | $\lambda_{em}^{max}$ ($\lambda_{ex}$=400 nm) [nm] | $\lambda_{em}^{max}$ ($\lambda_{ex}$=500 nm) [nm] | $\Phi^a$ ($\lambda_{ex}$=400 nm) | $\Phi^a$ ($\lambda_{ex}$=500 nm) |
|---|---|---|---|---|---|
| **T4 FONs** | 329; 374 | 484 | - | 0.06 | 0.06 |
| **T5 FONs** | 495 | 686 | 686 | 0.03 | 0.03 |
| **Core@shell T4@T5 FONs** | 339; 494 | 605 | 683 | 0.15 | 0.04 |

*[a]Fluorescence quantum yield measured using an integrating sphere in center-mount sample holder configuration*

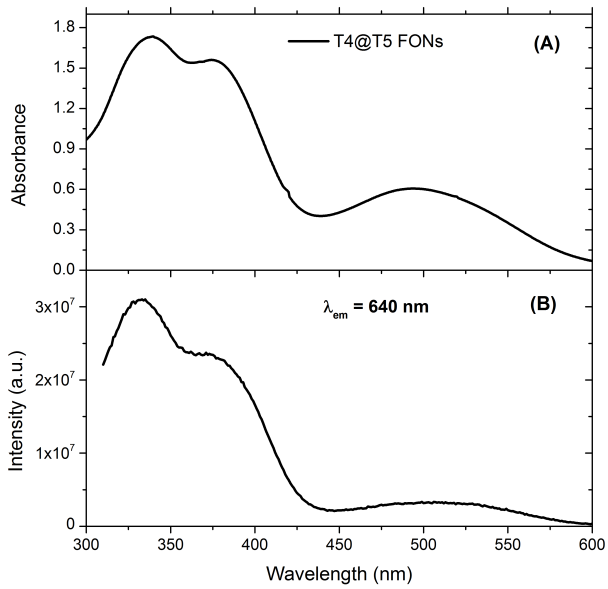


*Figure 4.17: Panel A: Absorption spectra of aqueous suspensions of **T4@T5** FONs. Panel B: Fluorescence excitation spectrum of the **T4@T5** FONs for detection at 640 nm.*

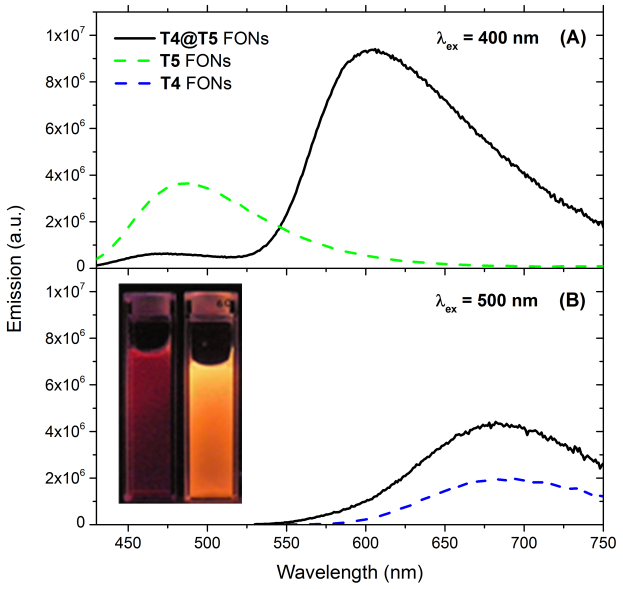


*Figure 4.18: Photoluminescence spectra of the nanoparticles based on* ***T4*** *and* ***T5*** *for excitation at 400 nm (A) and at 500 nm (B). Inset: on the left* ***T5*** *and on the right* ***T5*****@*****T4*** *FONs suspensions observed under UV-lamp* ($\lambda_{ex}$ = *340 nm).*

The shape and dimension of the nanoparticles are investigated by transmission electron microscopy using uranyl acetate as staining agent (Figure 4.19). Nanoparticles are round in shape and quite polydispersed. The average diameter calculated from TEM images is about 30 nm while the average diameter of pure **T4** nanoparticles is about 25 nm. These data indicate that the shell thickness is about 2.5 nm.

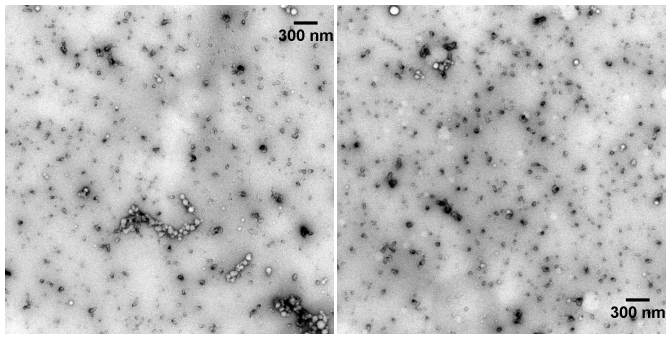


*Figure 4.19: Images of **T5@T4** nanoparticles by TEM. The average diameter of nanoparticles is about 30 nm.*

### 4.2.3 Multi Shell Nanostructures

In principle, following the preparation method described above (multi-step preparation), it is possible to prepare multi shell nanoassemblies able to achieve efficient EET cascade from the molecules that compose the first shell to the molecules of the core (on backwards), as resumed in Figure 4.20.

In this section we describe the preparation and characterization of ternary core@shell@shell nanostructures and, in particular, we focus the attention on the study of their stability and spectroscopic properties during time with and without the use of **PMMA** (Poly-methyl methacrylate) as a stabilizing dopant.

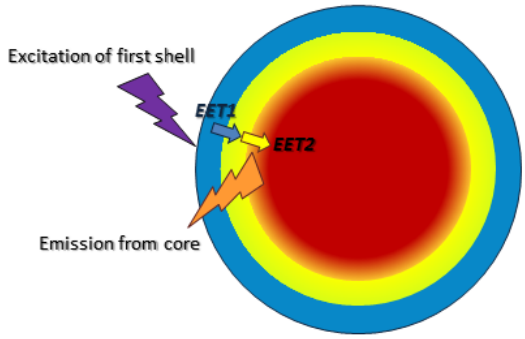


*Figure 4.20: A sketch of the proposed mechanism of energy transfer in core@shell@shell nanostructures. EET process takes place from the first to the second shell (EET1) and from the second shell to the core (EET2).*

Three complementary fluorescent triphenylamine-based chromophores have been chosen for preparing ternary nanosystems because of the good overlap of the emission spectrum of FONs from fluorophore **TW0** (**TW0** FONs) and the absorption spectrum of FONs from fluorophore **TW1** (**TW1** FONs) and for the good overlap between the spectra of **TW1** FONs and **TW3** FONs, as reported in Figure 4.21. The characteristics of **TW0** molecule [95] are reported in Appendix 3.

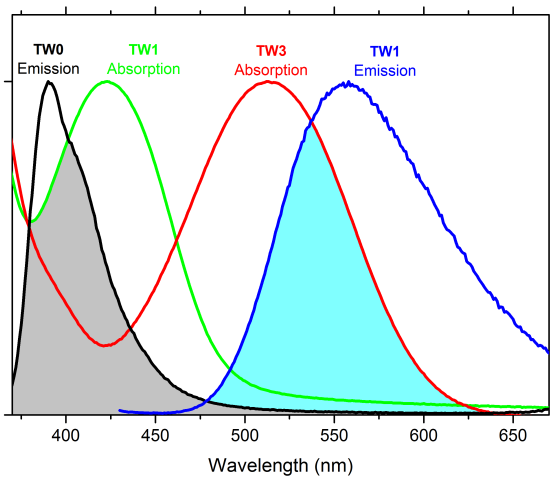


*Figure 4.21: Emission spectra of FONs that act as donors (**TW0** and **TW1**) and absorption spectra of FONs that act as acceptors (**TW1** and **TW3**), and corresponding overlaps (grey and cyan areas).*

Core@Shell@Shell (**TW3**@**TW1**@**TW0**) nanoparticles are obtained using a three-step reprecipitation method: first **TW3** FONs are precipitated in water under vigorous stirring, subsequently an amount of a THF solution of **TW1** is added to the aqueous suspension of **TW3** FONs, as to cover **TW3** FONs with a layer of fluorophore **TW1**, finally an amount of THF solution of **TW0** is added to the obtained **TW3**@**TW1** FONs suspension to create a third layer composed of dye **TW0**. The final nominal concentration is $1 \times 10^{-5}$M for all the dyes.

Core@Shell@Shell **PMMA**-doped nanoparticles are also obtained using a three-step reprecipitation process. First **PMMA**-doped **TW3** FONs are prepared by reprecipitation in water: **TW3** and **PMMA** solutions in THF are mixed together and a small amount of this common solution is added to a known amount of bidistilled water. Then an amount of a common **TW1** and **PMMA** THF solution is added to the obtained **PMMA**-doped **TW3** FONs suspension to obtain **PMMA**-doped **TW3**@**TW1** FONs. Finally an

amount of a THF solution of **TW0** and **PMMA** is added to the binary suspension, to give **TW3@TW1@TW0 PMMA**-doped nanostructures. The final nominal concentration is of $1 \times 10^{-5}$M for all the three chromophores and $3 \times 10^{-7}$M for **PMMA**.

Absorption and fluorescence spectra of core@shell@shell nanostructures are recorded for the dye suspensions in the native aqueous mixture at the end of the reprecipitation process and during time up to eleven weeks (Figure 4.22 and Figure 4.23). The spectroscopic characteristics of aqueous suspensions are summarized in Table 4.6.

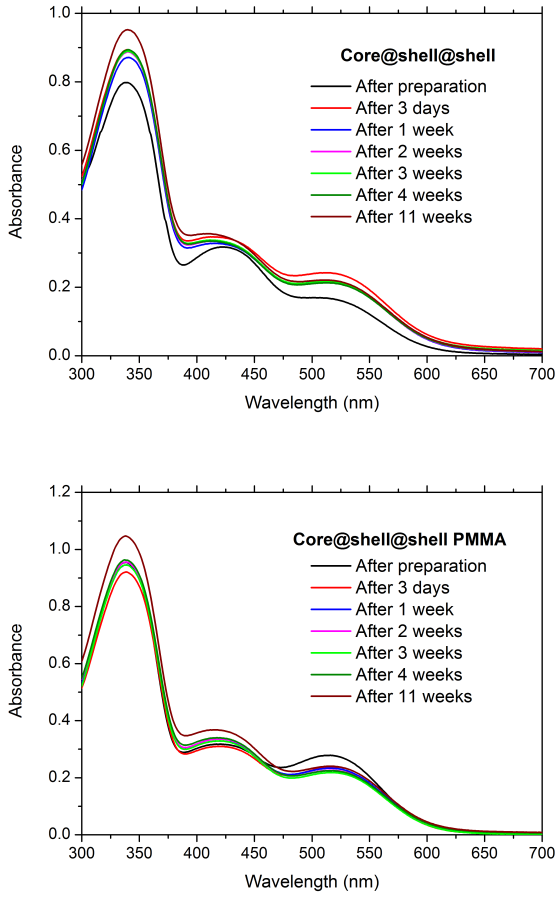


*Figure 4.22: Absorption spectra of* ***TW3@TW1@TW0*** *core@shell@shell nanoparticles suspensions without and with PMMA recorded during eleven weeks.*

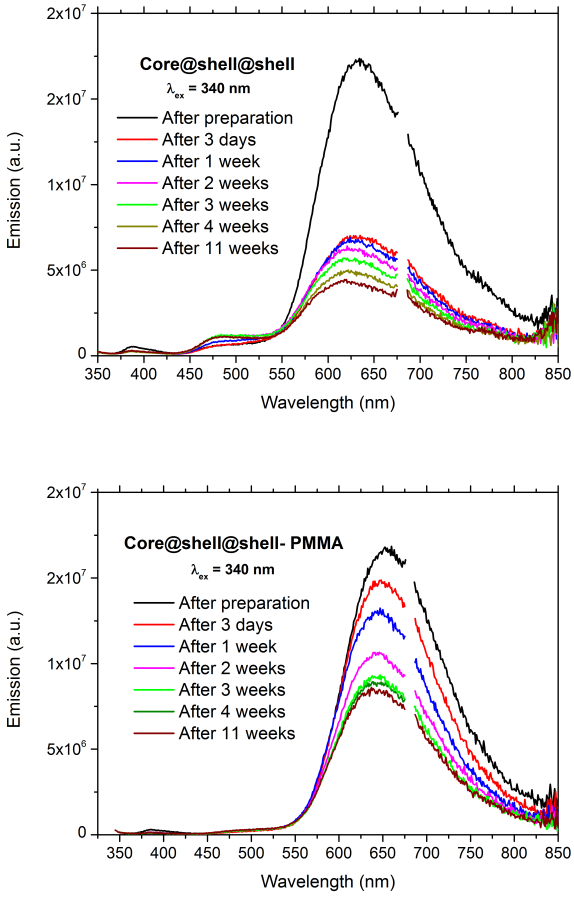


*Figure 4.23: The evolution of emission spectra of* ***TW3@TW1@TW0*** *core@shell@shell nanoparticles suspensions without and with PMMA. Excitation wavelength is fixed at 340 nm.*

*Table 4.6: Spectroscopic properties and zeta-potentials of **TW3@TW1@TW0** nanoassemblies (without and with **PMMA**) after preparation.*

| | | $\lambda_{ex}$ = 340 nm | $\lambda_{ex}$ = 420 nm | $\lambda_{ex}$ = 520 nm | | |
|---|---|---|---|---|---|---|
| | $\lambda_{abs}^{max}$ [nm] | $\lambda_{em}^{max}$ [nm][a] | $\lambda_{em}^{max}$ [nm] | $\lambda_{em}^{max}$ [nm] | $\Phi^{a}$ | Z-pot (mV) |
| $TW0_{FONs}$ | 331 | 390 | - | - | 0.08 | -42±2 |
| $TW1_{FONs}$ | 342; 422 | 552 | 552 | - | 0.07 | -46±1 |
| $TW3_{FONs}$ | 340; 515 | 697 | 697 | 697 | 0.06 | -36±3 |
| TW3@TW1@TW0 FONs | 338; 423; 514 | 623 | 625 | 692 | 0.20 | -44±2 |
| $TW0_{FONs}$ - PMMA | 331 | 391 | - | - | 0.13 | -41.6±1.5 |
| $TW1_{FONs}$ - PMMA | 341; 422 | 546 | 546 | - | 0.09 | -42.8±2.0 |
| $TW3_{FONs}$ - PMMA | 340; 514 | ~ 690 | ~ 690 | ~ 690 | 0.07 | -30.3±1.5 |
| TW3@TW1@TW0 FONs - PMMA | 338; 421; 516 | 652 | 648 | 687 | 0.15 | -40.0±1.5 |

*[a] Fluorescence quantum yield measured using fluorescein as reference ($\phi = 0.90$)*

The absorption spectra show three major bands due to the superposition of the absorption spectra of the three dyes. The absorption spectra of core@shell@shell nanoparticles with and without **PMMA** are quite stable during time. The slight growth observed after eleven weeks could be ascribed to a small variation of the concentration (evaporation of water). The suspensions are transparent to the naked eyes and there is no formation of visible aggregates in both types of nanosystems (no scattering is detectable in absorption spectra even after eleven weeks). When ternary nanoparticles (with and without **PMMA**) are excited at 340 nm (mainly excitation of chromophore **TW0**) the emission of **TW0** and **TW1** molecules is almost completely quenched while the emission of **TW3** in the red region is strongly enhanced. The emission maximum is found at about 625 nm for nanoassemblies without **PMMA** and about 650 nm for nanoparticles with **PMMA**.

The fluorescence quenching of the donors in the ternary nanostructures is an evidence of the efficient EET cascade from the first shell layer down to the core. When nanostructures (with and without **PMMA**) are excited at 520 nm (where only **TW3** absorbs) the obtained spectra are very similar to those of **TW3** FONs (Figure 4.24) as already observed for **TW3@TW1** binary nanostructures.

This behavior can be explained taking into account the layered structure of the nanoparticles: in core@shell@shell nanoassembly a EET cascade towards the core takes place.

To fully characterize the transfer process we have investigated the photoluminescence dynamics of the nanosystems (Table 4.7).

The fluorescence decays are found to be three-exponential for all nanoparticles, whatever the excitation wavelength. The selected excitation wavelength, 340 nm, corresponds to an almost selective excitation of donor **TW0**, that is located in the first shell. When the fluorescence decays are measured at 620 nm (corresponding to the emission of the core **TW3**) an increase (about fourfold) of the energy-acceptor lifetime is detected in core@shell@shell nanostructures, without and with **PMMA**. Instead, if the fluorescence decays are measured at 400 and 525 nm (the emitting regions of **TW0** FONs and **TW1** FONs, respectively) a strong decrease of the lifetimes are registered for ternary assemblies with or without **PMMA**. The marked shortening of the donors luminescence lifetimes and the lengthening of the acceptor luminescence lifetime in ternary structures provide nice confirmation of the efficient energy cascade **TW0**→**TW1**→**TW3**.

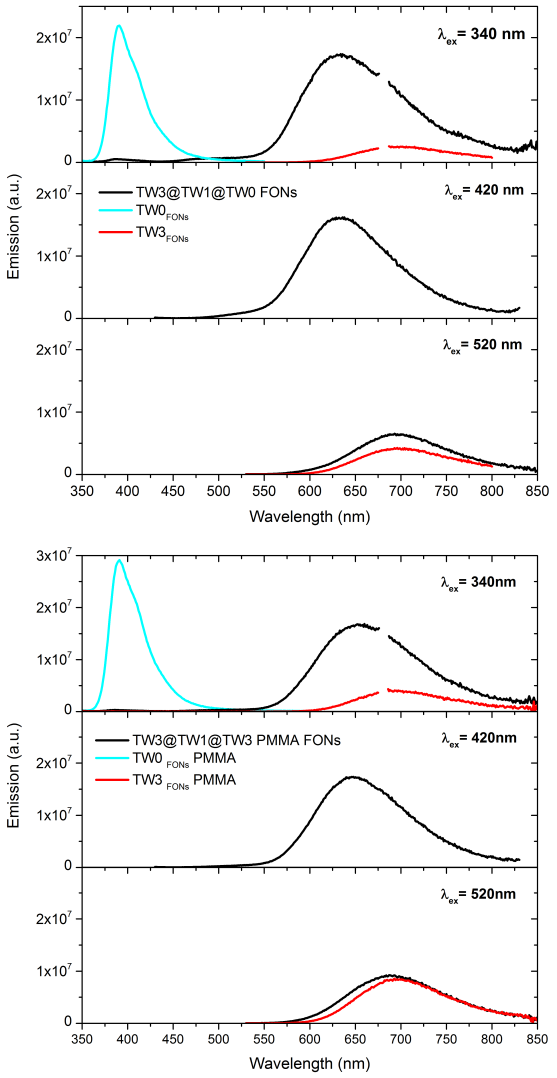


*Figure 4.24: Emission spectra of freshly prepared nanoparticles without* ***PMMA*** *(top panels) and with* ***PMMA*** *(bottom panels) for different excitation wavelengths.*

*Table 4.7: Lifetimes of nanosuspensions based on **TW0**, **TW1** and **TW3** (excitation at 340 nm) after preparation.*

| $\lambda_{ex}$ = 340 nm | | | | | | | | | |
|---|---|---|---|---|---|---|---|---|---|
| | $\lambda_{em}$ = 400 nm | | | $\lambda_{em}$ = 525 nm | | | $\lambda_{em}$ = 620 nm | | |
| | $\tau_1$ [ns] | $\tau_2$ [ns] | $\tau_3$ [ns] | $\tau_1$ [ns] | $\tau_2$ [ns] | $\tau_3$ [ns] | $\tau_1$ [ns] | $\tau_2$ [ns] | $\tau_3$ [ns] |
| $TW0_{FONs}$ | 0.48 (0.98) | 2.26 (0.02) | - | - | - | - | - | - | - |
| $TW1_{FONs}$ | - | - | - | 0.40 (0.40) | 1.48 (0.43) | 3.93 (0.17) | - | - | - |
| $TW3_{FONs}$ | - | - | - | - | - | - | 0.73 (0.23) | 2.64 (0.54) | 5.83 (0.23) |
| TW3@TW1@TW0 FONs | <0.4 | - | - | 0.35 (0.64) | 1.48 (0.30) | 6.71 (0.06) | 2.60 (0.26) | 7.51 (0.60) | 25.80 (0.14) |
| $TW0_{FONs}$ - PMMA | 0.28 (0.28) | 0.62 (0.71) | 3.59 (0.01) | - | - | - | - | - | - |
| $TW1_{FONs}$ - PMMA | - | - | - | 0.32 (0.38) | 1.29 (0.46) | 3.70 (0.16) | - | - | - |
| $TW3_{FONs}$ - PMMA | - | - | - | - | - | - | 0.48 (0.23) | 2.92 (0.49) | 6.97 (0.28) |
| TW3@TW1@TW0 FONs - PMMA | ND | ND | ND | 0.34 (0.82) | 1.60 (0.12) | 6.66 (0.06) | 1.05 (0.14) | 4.62 (0.61) | 13.35 (0.25) |

From the point of view of stability, emission spectra of core@shell@shell nanoparticles without **PMMA** dramatically decrease after three days and after eleven weeks no significant changes are detected any more. Instead, emission spectra of ternary nanoassemblies with **PMMA** decrease systematically during weeks, but the initial decrease is less pronounced than for suspensions without **PMMA** (Figure 4.23). The quantum yields ($\Phi$) of core@shell@shell without and with **PMMA** after preparation are 0.20 and 0.15, respectively. The ratio between the emission maximum and the absorbance at the excitation wavelength (proportional to the quantum yield) is reported in Figure 4.25 as a function of time.

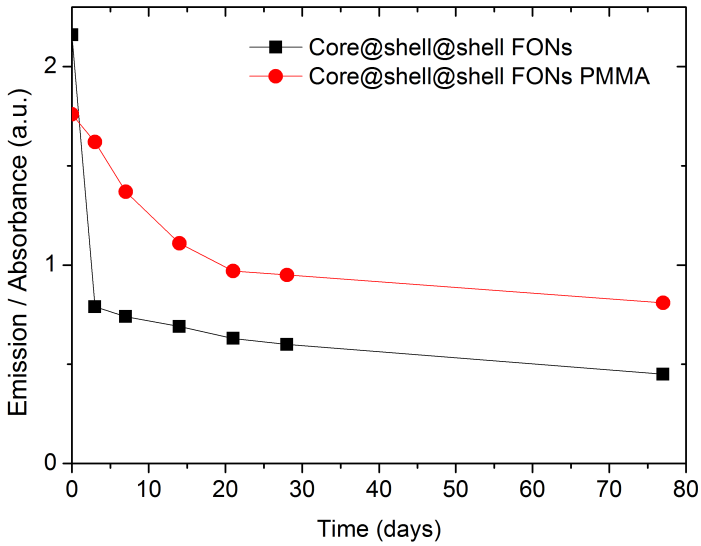


*Figure 4.25: Ratio of the intensity of emission spectra (at the maximum) and absorbance (at the excitation wavelength) of* ***TW3@TW1@TW0*** *nanosuspensions with and without* ***PMMA****.*

This ratio (and hence the quantum yield) decreases in both types of nanoassemblies (without and with **PMMA**), but the slope is steeper in systems without **PMMA** and their quantum yield stays always lower than for systems with **PMMA**. As there there is no significant variation of the absorption spectra (that means that no massive aggregation takes place, see Figure 4.22), the variation of emission spectra (and consequently the lowering of the quantum yields) can be ascribed to the slow rearrangement of molecules inside the nanoparticles, promoting for example π-π stacking and/or the interactions between nanoparticles and water. The presence of **PMMA** plays a key role in reducing these effects: probably the polymer chains screen the interchromophore interactions inside nanoparticles reducing π-π stacking, and could also reduce the chromophore-water interaction resulting in a bigger quantum yield after days or weeks.

Another confirmation of efficient cascade energy transfer comes from two-photon excitation fluorescence (TPEF, set-up described in Appendix 2). Briefly, the set-up allows for the recording of corrected fluorescence emission spectra under multiphoton excitation at variable excitation powers and wavelengths.

With our TPEF setup it was impossible to selectively two-photon excite **TW0** (i.e. the external shell), because the laser source does not deliver wavelengths $< 700$ nm. We thus decided to two-photon excite at 840 nm (i.e. twice the one-photon absorption wavelength of **TW1**). When exciting **TW1** nanoparticles, a very weak TPEF signal is detected (dashed blue line in Figure 4.26, top panel). When exciting the core@shell@shell nanoparticle suspension at 840 nm, chromophores composing the inner shell (**TW1**) are selectively excited. As already observed in one-photon fluorescence spectra, the two-photon excited fluorescence can clearly be ascribed to the emission from **TW3** molecules (located in the core), as reported in Figure 4.26, top panel. This is a clear evidence of the occurring of very efficient EET from the inner shell (**TW1**) to the core (**TW3**). Very interesting is the comparison with the TPEF spectrum of TW3 nanoparticles (obtained by two-photon excitation at 1040 nm, i.e. twice the one-photon absorption wavelength of **TW3**): no significant TPEF signal is detected (see Figure 4.26, bottom panel). This means that exploiting EET in multi-component nanostructures is a very efficient way to enhance the two-photon emission signal. This result is particularly important for bioimaging applications, where water-dispersed TPEF probes efficiently emitting at red or NIR wavelengths are sought (see Chapter 2).

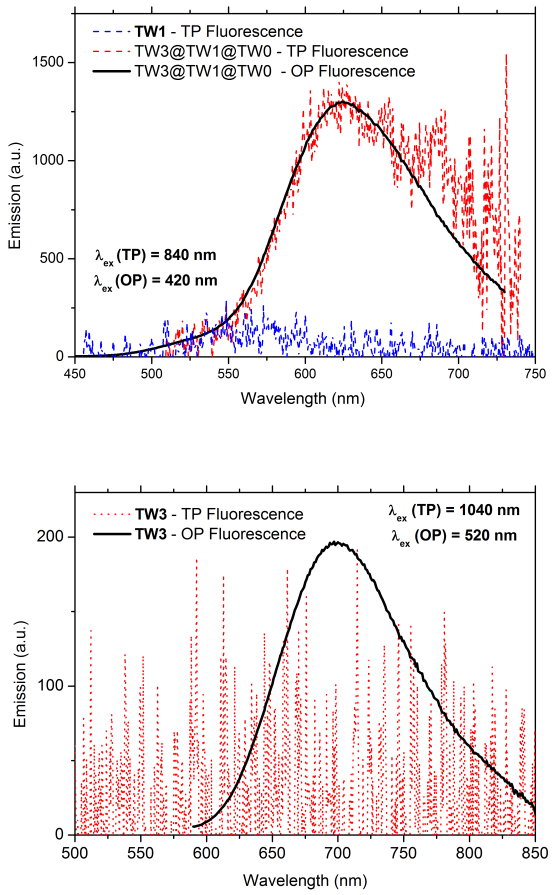


*Figure 4.26: Top: two-photon excited fluorescence spectra of* ***TW3@TW1@TW0*** *FONs (red dotted line) and of* ***TW1*** *FONs (blue dotted line). One-photon excitation fluorescence of* ***TW3@TW1@TW0*** *FONs (black line). Bottom: two-photon (red dotted line) and one-photon (black line) excitation fluorescence of* ***TW3*** *FONs.*

From the point of view of colloidal stability it must be pointed out that the suspensions are expected to be stable during time because zeta-potential

analysis performed after the reprecipitation process gives values lower than -30 mV, which are indicative of good colloidal stability (Table 4.6). The suspensions are indeed transparent to the naked eyes even after several weeks and no aggregates or precipitates are detected. The suspension stability is confirmed by both the absorbance spectra and TEM images. In absorbance spectra collected after weeks no scattering is observed (Figure 4.22). Furthermore, TEM images and statistical analysis on average diameters confirm the stability of the nanoassemblies: nanoparticles without **PMMA** display only a little growth of average diameter after eleven weeks (from 42 nm for freshly prepared to 56 nm for aged particles), while nanoparticles with **PMMA** display about the same diameter (42 nm for freshly prepared to 47 nm for aged particles) and distribution, as reported in Figures 4.27 and 4.28.

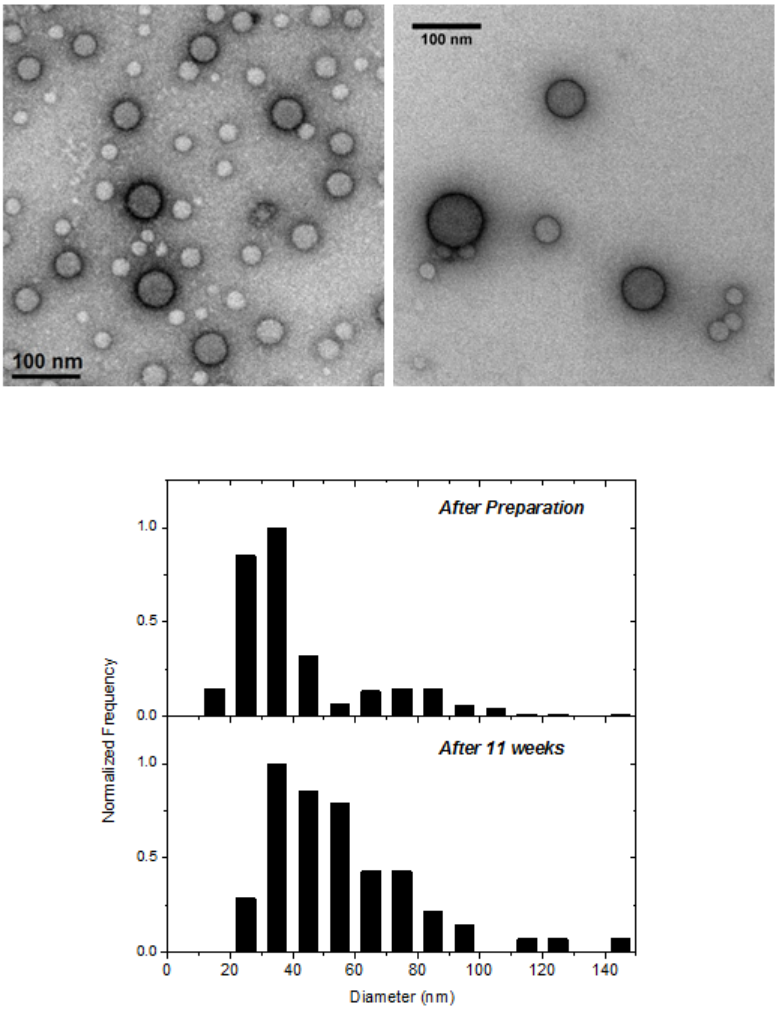


*Figure 4.27: Top: observation by TEM of* ***TW3@TW1@TW0*** *nanoparticles without* ***PMMA*** *freshly prepared (left) and after eleven weeks (right). Scale bar = 100 nm. Bottom: Statistical analysis of nanoparticle size after preparation and after eleven weeks.*

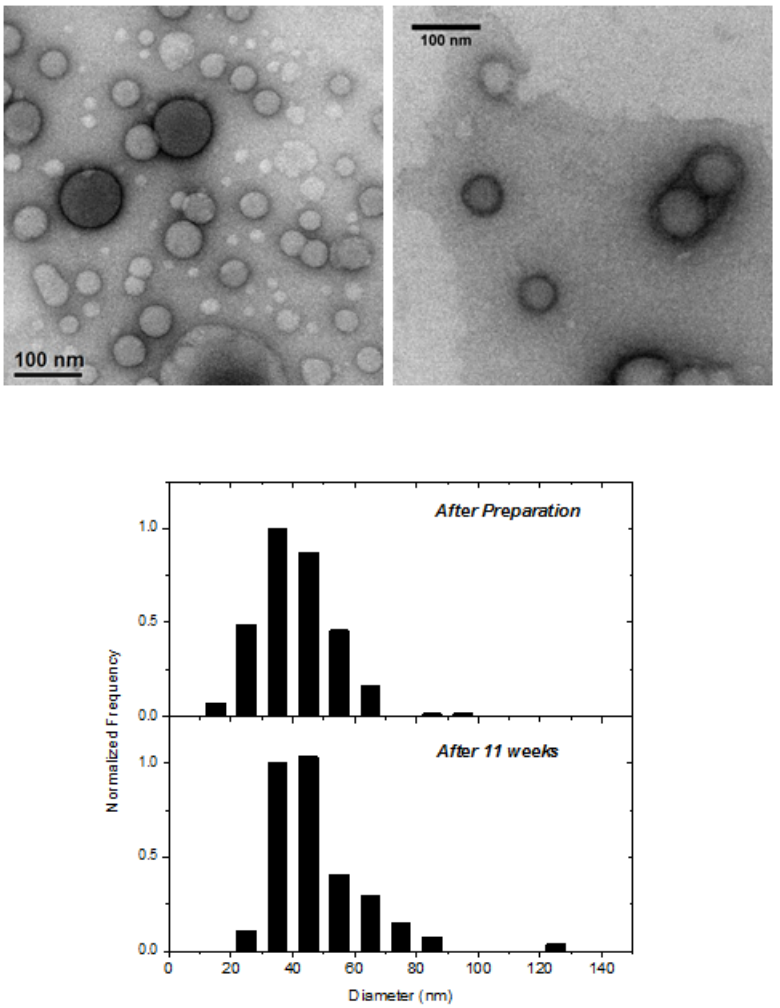


*Figure 4.28: Top: observation by TEM of* ***TW3@TW1@TW0*** *nanoparticles with* ***PMMA*** *freshly prepared (left) and after eleven weeks (right). Scale bar = 100 nm. Bottom: Statistical analysis of nanoparticle size after preparation and after eleven weeks.*

## 4.3 Organic Nanoassemblies for Electron Transfer

Organic nanoassemblies can be considered as new promising materials for organic bulk heterojunction solar cells because of the low cost of departing materials and the easy way of preparation. In general, bulk heterojunctions are prepared by mixing p- and n-type materials. Because holes are transported by the p-type semiconductor and electrons by the n-type material, these materials should be preferably mixed into a bicontinous, interpenetrating network. The name bulk-heterojunction solar cell has been chosen because the interface between two different components (heterojunction) is all over the bulk, in contrast to the classical (bi-layer) junction. Control of morphology is not only required for a large charge-generating interface and suppression of exciton loss, but also to ensure percolation pathways for both electron and hole transport to the collecting electrodes. The energy levels of the involved compounds and the scheme of a bulk heterojunction solar cell are reported in Figure 4.29.

A necessary condition to have charge separation is that both the LUMO and the HOMO levels of the electron donor are higher than those of the electron acceptor. This condition is necessary but not sufficient. For charge separation to occur, the differences in electron affinities and ionization potentials must overcome the exciton binding energy. In some cases excitation energy transfer competes with electron transfer to hinder the charge separation.

In this section we report the study of the HOMO and LUMO levels of two organic molecules, **TW3** and **DiMe-PTCDI** (Figure 4.30). **PTCDI** is a typical electron-acceptor molecule for organic solar cells.

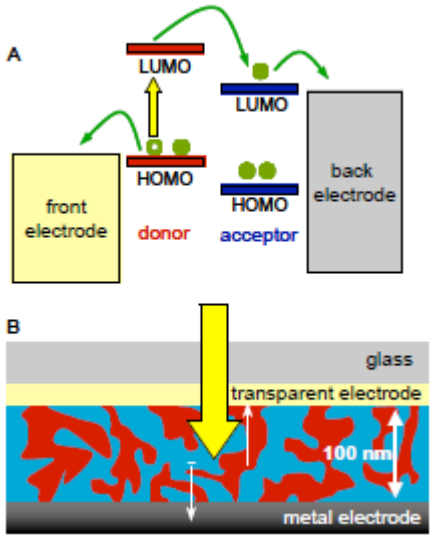


*Figure 4.29: The bulk-heterojunction concept. After absorption of light by the polymer or dye, fast charge transfer occurs due to the nanoscopic mixing of the donor and acceptor materials. Subsequently, the photogenerated charges are transported and collected at the electrodes.*

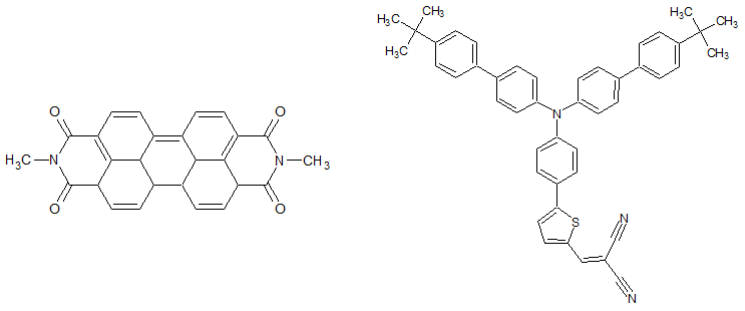

*Figure 4.30: Chemical structures of **DiMe-PTCDI** (left) and **TW3** (right).*

The molecular geometry optimizations are performed with the Gamess

software package by using DFT methods with B3LYP hybrid exchange-correlation functional. The 6-31G basis set has been used for calculations on the investigated systems. The obtained energy levels are reported in Table 4.8 and in Figure 4.31.

*Table 4.8: Calculated HOMO and LUMO levels for **TW3** and **DiMe-PTCDI**. *The values reported for **PTCDI** are from Ref. [161]*

| | HOMO [eV] | LUMO [eV] | Δ [eV] | Dipole Moment (D) |
|---|---|---|---|---|
| **TW3** | -5.279 | -2.902 | 2.376 | 11.72 |
| **DiMe-PTDCI** | -6.137 | -3.642 | 2.495 | 0 |
| ***PTDCI**** | *-6.11* | *-3.57* | *2.54* | - |

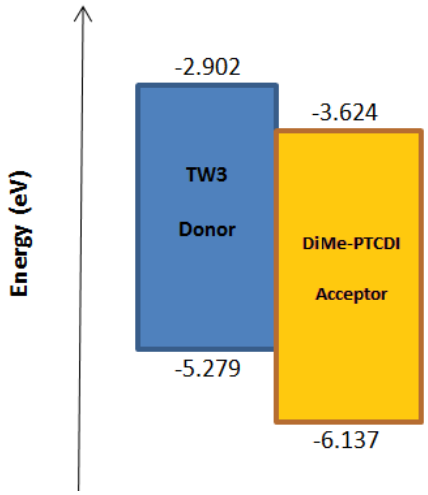


*Figure 4.31: Energy diagram of **TW3** and **DiMe-PTCDI** molecules.*

From a theoretical point of view the HOMO and LUMO energy levels of the donor and acceptor are in the right configuration to obtain electron

transfer. For this reason core@shell nanoparticles composed by **TW3** as core and **DiMe-PTCDI** as shell have been prepared and spectroscopically characterized.

### 4.3.1 Preparation of TW3@DiMe-PTCDI Nanoparticles

**TW3@DiMe-PTCDI** nanoparticles are prepared using a "modified" multi-step reprecipitation method. **TW3** nanoparticles are firstly prepared by adding 100 µL of **TW3** stock solution ($1\times10^{-3}$ M in THF) to 10 mL of water under vigorous stirring to obtain a final nominal concentration of $1 \times 10^{-5}$ M. Since the solubility of **DiMe-PTCDI** in THF is low (it is not possible to obtain a $1\times10^{-3}$ M solution in THF because of the very low solubility) a $6.44\times10^{-5}$ M stock solution has been prepared. An amount of 400 µL of this **DiMe-PTCDI** stock solution is added to the prepared **TW3** nanoparticle suspension under vigorous stirring. After the addition, THF is evaporated under vacuum (rotovapor, with bath at 35°C). The addition/evaporation step has been repeated 4 times to obtain a final nominal concentration of **TW3** and **DiMe-PTCDI** of $1\times10^{-5}$ M for both compounds (sample name: **CS1:1**).

**DiMe-PTCDI** nanoparticles at $1\times10^{-5}$ M are prepared with the same method, while **TW3** nanoparticles at $1 \times 10^{-5}$ M are prepared using the classical reprecipitation process.

### 4.3.2 Spectroscopic Characterization of TW3@DiMe-PTCDI Nanoparticles

Absorption spectra of **TW3** and **DiMe-PTCDI** nanoparticles are reported in Figure 4.32. It must be noticed that the overlap between the emission spectrum of the electron donor (**TW3**) and the absorption spectrum of the electron acceptor (**PTCDI)** is small: excitation energy transfer is expected to be negligible in this system not only because of the HOMO-LUMO alignment.

The absorption spectrum of the core@shell system corresponds well to the sum of the spectra of **TW3** and **DiMe-PTCDI** nanoparticles: this result confirms that the method used to prepare core@shell and **DiMe-PTCDI** NPs is accurate and reproducible despite the subsequent additions (Figure 4.33).

The emission spectra of the prepared nanoparticles excited at 520 nm is reported in Figure 4.34.

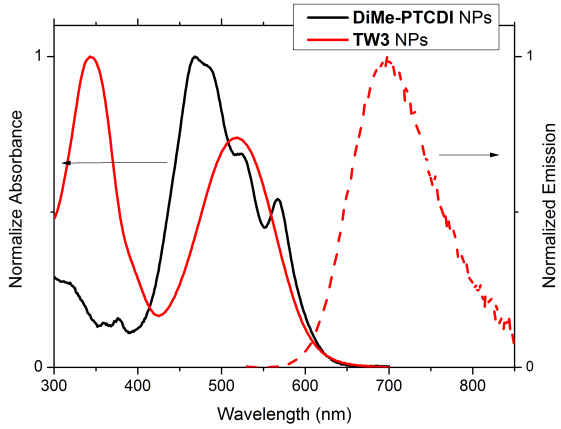


*Figure 4.32: Absorption spectra of **TW3** (full red line) and **DiMe-PTCDI** (full black line) NP suspensions. Emission spectrum of **TW3** NP suspension (dotted red line).*

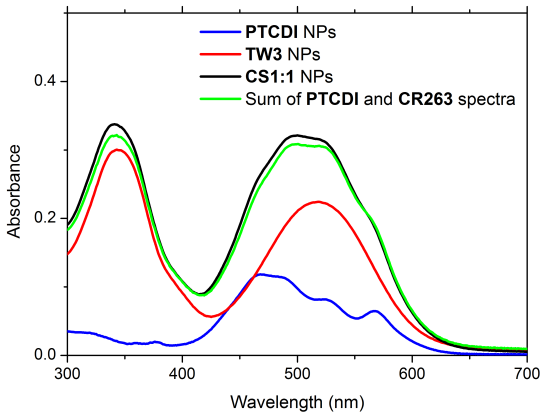


*Figure 4.33: Absorption spectra of **TW3**, **DiMe-PTCDI**, **CS1:1** nanoparticles. The sum of **TW3** and **DiMe-PTCDI** spectra is almost superimposable to the spectrum of **CS1:1** nanoparticles.*

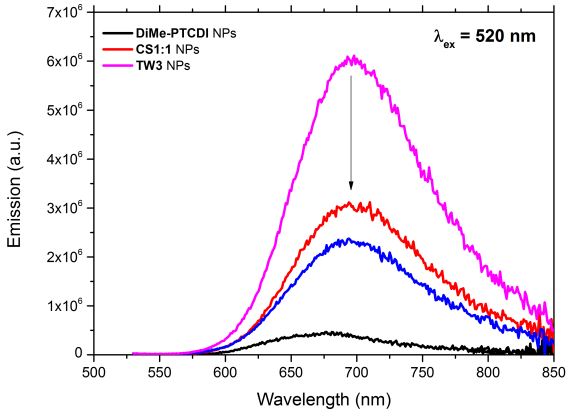


*Figure 4.34: Emission spectra of **DiMe-PTCDI**, **CS1:1** and **TW3** NP suspensions excited at 520 nm. **TW3** emission is partially quenched in core@shell systems.*

It can be noticed that when the core@shell nanoassembly is excited at

520 nm the emission of **TW3** decreases of about 50% compared to the emission spectrum of isolated **TW3** nanoparticles. Due to the HOMO-LUMO configuration and the fact that the overlap between **TW3** emission and **DiMe-PTCDI** absorption is very low, the decrease can be tentatively ascribed to the electron transfer process, which would take place between the two compounds at the core@shell interface. Furthermore, the fluorescence excitation profiles of core@shell suspensions (Figure 4.35) registered when collecting fluorescence at 675 nm (where the emission of **DiMe-PTCDI** is negligible compared to the emission of **TW3**), reveal that the excitation spectra of core@shell nanoassembly and **TW3** are almost superimposable. This means that in both cases the fluorescence signal is only from **TW3** and energy transfer does not probably take place between the two compounds.

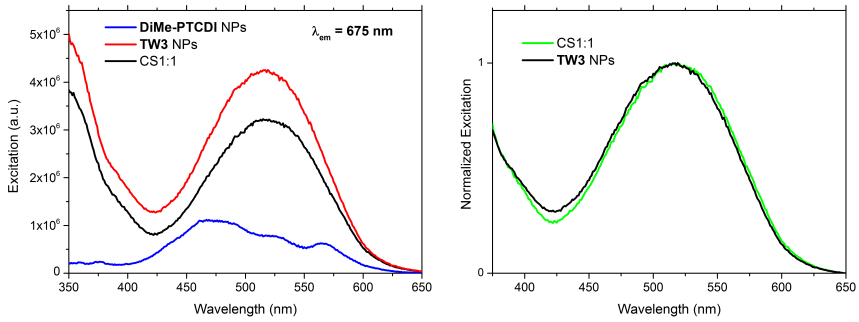


*Figure 4.35: Excitation spectra of **DiMe-PTCDI**, **CS1:1** and **TW3** NPs (left) detecting fluorescence at 675 nm (on the maximum of **DiMe-PTDCI** emission); normalized excitation spectra of core@shell systems and **TW3** NPs (right). The excitation spectra of core@shell and isolated **TW3** nanoparticles have the same shape: for **CS1:1** nanosystems no fluorescence from **DiMe-PTDCI** is detected.*

To definitively prove the occurring of electron transfer time-resolved ex-

periments are currently under study[1].

[1]Collaboration with Prof. Cerullo, Politecnico di Milano

## 4.4 Conclusions

In this chapter the preparation and characterization of modulable-emission nanoparticles by excitation energy transfer are reported. In doped nanoparticles a little amount of guest compound (energy acceptor) is integrated into a host matrix (energy donor): accordingly to the guest concentration the emission can be tuned over a quite large wavelength region. Then core@shell nanoassemblies are prepared using the acceptor compound as core and the donor as shell. We have demonstrated that novel fully organic and molecular-based core@shell nanoparticles promoting highly efficient directional EET from the shell to the core can be prepared in a simple way by a stepwise reprecipitation process in water. The resulting red emission is shown to stem only from acceptor molecules at the nanointerface between core and shell, resulting in a striking luminescence enhancement with respect to both single-component nanoparticles and composite nanoparticles. This intriguing and appealing phenomenon opens a new arena for tuning and enhancing luminescence properties of organic nanostructures by engineering nanointerfaces between polar/polarizable chromophores. In addition, it paves the way for the design of "smart" multi-shell organic nanostructures taking advantage of both directional EET and interfacial phenomena, as demonstrated by the study of core@shell@shell nanoparticles. Such fully organic molecular-based nanosystems could find important applications in several fields, including bioimaging and photovoltaics.

Furthermore, core@shell nanoparticles for electron transfer have been prepared and are now under study.

# Conclusions and Perspectives

This thesis presents an extensive study on fluorescent organic nanoparticles and fluorescent organic binary and ternary nanoassemblies for biological and optoelectronic applications. The study is focused on the preparation processes and spectroscopic and morphological characterization of these types of new fully organic nanostructures.

The work dealt at the beginning with the preparation of fluorescent organic nanostructures (FONs) starting from different types of chromophores. This study allowed to define some basic rules that must be followed to generate fluorescent organic nanoparticles in water, such as the chromophore fluorescence in the solid state, the non-solubility in water and the final recommended concentration. However, these simple rules cannot reliably predict the stability of the suspensions. In fact, there are plenty of parameters that can affect the stability: molecular structure, polarizability, solubility in water, temperature, concentration and it is very hard to find safe general rules to obtain stable fluorescent organic nanoparticles in water: for these systems the only method to evaluate the stability is still "trial and error".

The second part focused on the description of different types of biphotonic probes and the use of fluorescent organic nanoparticles for multiphoton microscopy. In particular, two different types of chromophores have been used to prepare FONs suspensions in water. These suspensions have been spectroscopically characterized by linear and nonlinear optical techniques, namely absorption, fluorescence and two-photon induced fluorescence. The

obtained gigantic two-photon brightness has been exploited for *in vivo* two-photon imaging. Some of the FONs are extremely good for imaging the blood vessels, in terms of brightness, stability and contrast. All of these characteristics make our FONs promising fluorescent tracers for two-photon *in vivo* angiography.

The third part of the work focused on the colloidal stabilization of nanoparticle suspensions. In particular, we prepared nanoparticles using ultrasounds and different types of additives at low concentration, obtaining an improvement of the colloidal stability during time. The presence of additives, probably located on the surface of nanoparticles, plays a key role in changing their surface charge and, consequently, in enhancing the electrostatic repulsions and reducing aggregation phenomena during time. A second and "indirect" way of stabilization that was described is the so-called "Molecular Design". A small modification of the molecular structures of the starting materials can allow to obtain very fast reprecipitation processes (few seconds) and good colloidal stability of the nanoparticle suspensions (weeks or months).

In the last part of the thesis the preparation and characterization of modulable-emission nanoparticles by excitation energy transfer were reported. In particular novel binary core@shell nanoassemblies were prepared using the energy acceptor compound as core and the energy donor as shell. We have demonstrated that these fully organic and molecular-based core@shell nanoparticles promote highly efficient directional energy transfer from the shell to the core, together with a striking luminescence enhancement with respect to both single-component nanoparticles. This intriguing and appealing phenomenon, reported here for the first time, opens a new arena for tuning and enhancing luminescence properties of organic nanostructures by engineering nanointerfaces between polar/polarizable chromophores. In addition, it paves the way for the design of "smart" multi-shell organic nanostructures taking advantage of both directional energy transfer and interfacial phenomena, as demonstrated by the study of core@shell@shell nanoparticles.

Furthermore, core@shell nanoparticles for electron transfer have been prepared and are currently under study through ultrafast transient spectroscopy.

# Appendix 1

## Chemical Structures of Chromophores used for Nanoparticles Preparation

### Commercial Compounds

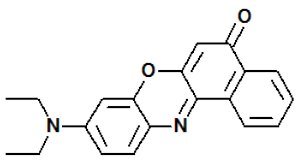


Nilered

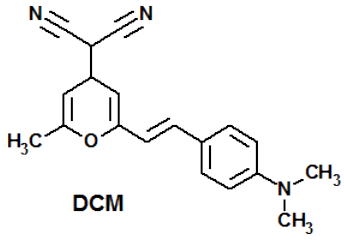


DCM

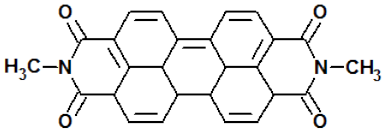


DiMe-PTCDI

## Bodipy Compound

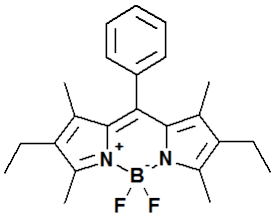


MB

## Thiophene-based Compounds

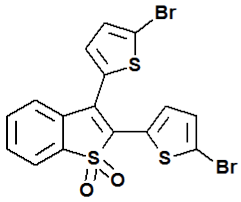


TP1

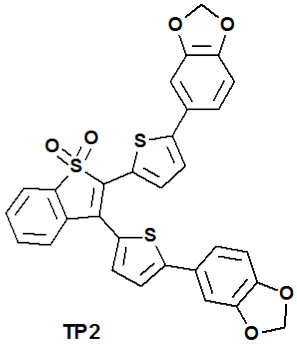


TP2

## Triphenylamine-based Compounds

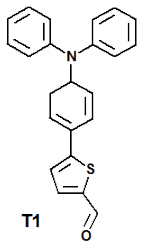


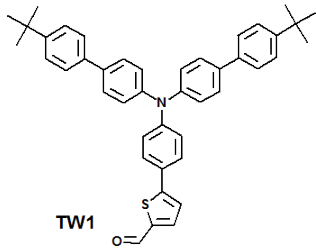


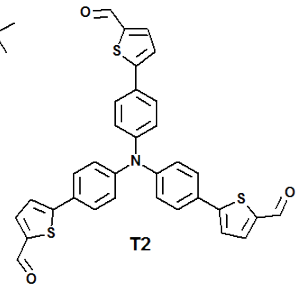


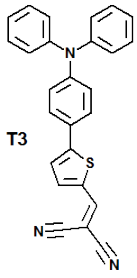


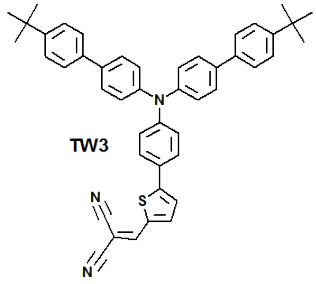


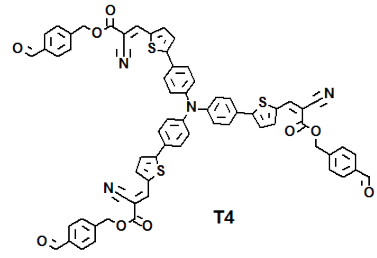


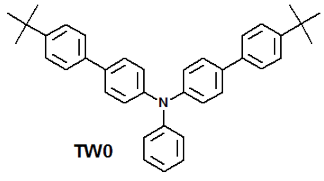


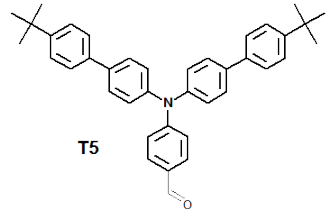

# Appendix 2

## Two-photon excited Fluorescence

Two-photon absorption is a third-order nonlinear process in which two photons generated from a coherent laser source are absorbed simultaneously by the sample. The two-photon absorption cross section data reported in Chapter 2 and the two-photon excited fluorescence reported in Chapter 4 (Figure 4.26) were measured using the two-photon excited fluorescence (TPEF) technique. The TPEF technique measures the fluorescence signal induced by the simultaneous absorption of two photons. The two-photon absorption cross section, $\sigma_2(\lambda)$, is derived by comparison to a reference compound and by the fluorescence quantum yield ($\phi$) of the sample. Assuming that $\phi$ is the same when the sample is excited by one or two photons, the fluorescence signal $F$ induced by two-photon absorption is:

$$F \propto \frac{cP^2 f \sigma_2(\lambda)\phi}{n^2} \tag{4.16}$$

where $c$ is the concentration of the absorbing chromophore, $P$ is the incident power and $f$ is a correction factor depending on the instrumental conditions and $n$ is the refractive index of the medium.

The values of $\sigma_2(\lambda)$ of the sample are evaluated by comparing the two-photon induced fluorescence intensity from the sample with the fluorescence signal of a reference compound ($R$) for each two-photon excitation wave-

length:

$$\sigma_2(\lambda) = \frac{[\sigma_2(\lambda)\phi]_R}{\phi}\frac{f_R}{f}\frac{F}{P^2}\left(\frac{F_R}{P_R^2}\right)^{-1} \tag{4.17}$$

The output signals are represented by the ratio $F/P^2$ for the sample and for the reference compound. The power $P$ is varied almost 3 times for every wavelength (by varying the transmittance of an optical filter placed on the laser pathway): the obtained $F/P^2$ values must be constant, i.e. the fluorescence signals must have a quadratic dependence on the incident power to rule out the occurrence of photodegradation or saturation phenomena. The units commonly adopted for $\sigma_2$ are the Göppert-Mayer (GM) defined as $1\text{GM} = 10^{-50}\text{cm}^4 \cdot \text{s} \cdot \text{photon}^{-1}$.

According to the spectral region, two different reference compounds are used: fluorescein in 0.01 NaOH from 700 to 980 nm, and **Nilered** in EtOH from 980 to 1200 nm. Measurements were performed adopting the experimental protocol proposed by Xu and Webb [162].

The excitation source is a Ti:sapphire femtosecond laser system, delivering pulses of ca 150 fs duration and 76 MHz repetition rate. This laser supplies photons in the 700-980 nm spectral range. At University of Rennes 1, to extend the spectral region up to 1200 nm, an optical parametric oscillator is used (OPO). The incident power on the sample is on the order of a few mW. The laser beam is focused onto the quartz cell holding the sample and the fluorescence signal is collect in the backward direction with respect to excitation (epifluorescence geometry).

# Appendix 3

## TW0 and T5 Nanoparticles

**TW0** and **T5** chromophores (molecular structures in Figure A3.1), used for the preparation of binary and ternary nanostructures described in Chapter 4, have been firstly synthesized and characterized by Ishow and co-workes [95].

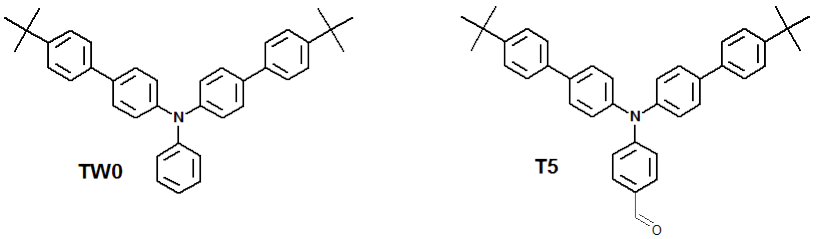


Figure A3.1 *Chemical structures of* ***TW0*** *and* ***TW5*** *compounds.*

In Figure A3.2 we report the emission spectra of nanoparticle suspensions obtained from the two molecules using the classical reprecipitation method, together with the solid state emission spectra.

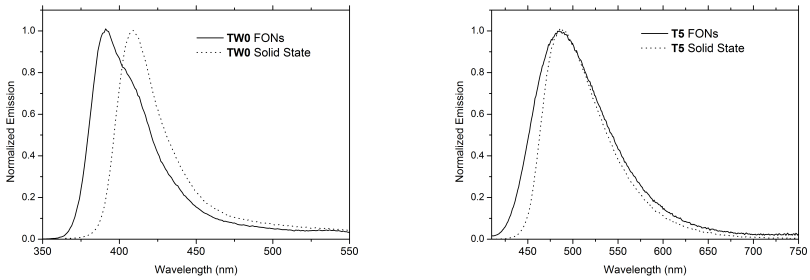


Figure A3.2 *Emission spectra of* ***TW0*** *(left) and* ***T5*** *(right) FONs suspensions and of the chromophores in the solid state.*

# Acknowledgments

I wish to express my deep gratitude to my supervisors, Prof. Francesca Terenziani and Prof. Mireille Blanchard-Desce, for their constant presence, guidance and support during this PhD training.

I also thank people of Università degli Studi di Parma and Université Rennes1 for interesting and useful discussion: Prof. A. Painelli, Prof. Olivier Mongin, Ph.D. C. Sissa.

I wish to thank all people I have collaborated with:

- Prof. Lucia Nasi and Dr. Marco Campanini of IMEM-CNR of Parma (Italy)
- Prof. Suzanne Fery-Forgues of Université Paul Sabatier UMR 5623 (France)
- Ph.D. Gaelle Recher of Université Rennes1 UMR 6026 (France)
- Prof. Giulio Cerullo and Ph.D. Francesco Scotognella of Politecnico di Milano (Italy)

all people of the UMR 6510 of Université Rennes1 (France) and all the people of the MMAA of Università degli Studi di Parma.

This thesis was supported by the Italo-French University through the Vinci Program.

# Bibliography


[1] U. Banin, Y. Cao, D. Katz, O. Millo. *Nature*, **1999**, *400*, 542.

[2] X. Peng, L. Manna, W. Yang, J. Wickham, E. Scher, A. Kadavanich, A. P. Alivisatos. *Nature*, **2000**, *404*, 59

[3] W. W. Yu, L. Qu, W. Guo, X. Peng. *Chem. Mater.*, **2003**, *15*, 2854.

[4] A. H. Mueller, M. A. Petruska, M. Achermann, D. J. Werder, E. A. Akhadov, D. D. Koleske, M. A. Hoffbauer, V. I. Klimov. *Nano Lett.*, **2005**, *5*, 1039.

[5] W. U. Huynh, X. Peng, A. P. Alivasatos. *Adv. Mater.*, **1999**, *11*, 923.

[6] A. N. Shipway, E. Katz, I. Willner. *ChemPhysChem*, **2000**, *1*, 18.

[7] Y. C. Cao, R. Jin, C. A. Mirkin. *Science*, **2002**, *297*, 1536.

[8] F. Hu, L. Wei, Z. Zhou, Y. Ran, Z. Li, M. Gao. *Adv. Mater.*, **2006**, *18*, 2553.

[9] M. Okubo, H. Minami, K. Morikawa. *Colloid Polym. Sci.*, **2003**, *281*, 214.

[10] C. Szymanski, C. Wu, J. Hooper, M. A. Salazar, A. Perdomo, A. Dukes, J. McNeill. *J. Phys. Chem. B*, **2005**, *109*, 8543.

[11] F. Chen, Y. Kondo, T. Hashimoto, *Macromolecules.* **2007**, *40*, 3714.

[12] J. Rieger, D. Horn, *Angew. Chem. Int. Ed.*, **2001**. *40*, 4330.

[13] Y. S. Zhao, H. Fu, A. Peng, Y. Ma, D. Xiao, J. Yao. *Adv. Mater.*, **2008**, *20*, 2859

[14] H. Kasai, H. Kamatani, S. Okada, H. Oikawa, H. Matsuda, H. Nakanishi. *Jpn. J. App. Phys.*, **1996**, *35*, L221.

[15] R. C. Smith, W. M. Fischer, D. L. Gin. *J. Am. Chem. Soc.*, **1997**, *119*, 4092.

[16] A. Sellinger, P. M. Weiss, A. Nguyen, Y. Lu, R. A. Assink, W. Gong, C. J. Brinker. *Nature*, **1998**, *394*, 256.

[17] V. Parthasarathy, S. Fery-Forgues, E. Campioli, G. Recher, F. Terenziani, M. Blanchard-Desce. *Small*, **2011**, *7*, 3219.

[18] E. Campioli, C. Rouxel, M. Campanini, L. Nasi, M. Blanchard-Desce, F. Terenziani. *Small*, **2013**, DOI: 10.1002/smll.201202504

[19] A.-D. Peng, D.-B. Xiao, Y. Ma, W.-S. Yang, J.-N. Yao. *Adv. Mater.*, **2005**, *17*, 2070.

[20] S. Kita, S. Masuo, S. Machida, A. Itaya. *Jpn. J. Appl. Phys.*, **2006**, *45*, 6501.

[21] J. Yang, R. Wang, R. Ding, A.-W. Li, Y.-S. Yu, J.-P. Wang, H. Yang. *Chem. Res. Chinese Universities*, **2011**, *27*, 1045.

[22] T. Ashai, T. Sugiyama, H. Masuhara. *Acc. Chem. Res.*, **2008**, *41*, 1790.

[23] H. Kasai, H. S. Nalwa, H. Oikawa, S. Okada, H. Matsuda, N. Minami, A. Kakuda, K. Ono, A. Mukoh, H. Nakanishi. *Jpn. J. Appl. Phys.*, **1992**, *31*, L1132.

[24] H. Masuhara, H. Nakanishi. in *Single Organic Nanoparticles*, Springer, Berlin, **2003**, Ch.2, p.17.

[25] T. Tachikawa, H.-R. Chung, A. Masuhara, H. Kasai, H. Oikawa, H. Nakanishi, M. Fujitsuka, T. Majima. *J. Am. Chem. Soc.*, **2006**, *128*, 15944.

[26] A. J. Gesquiere, T. Uwada, T. Ashai, H. Masuhara, P. F. Barbara, *Nano Lett.*, **2005**, *5*, 1321.

[27] H. Auweter, H. Haberkorn, W. Heckmann, D. Horn, E. Luddecke, J. Rieger, H. Weiss, *Angew. Chem. Int. Ed.*, **1999**, *38*, 2188.

[28] D. Xiao, L. Xi, W. Yang, H. Fu, Z. Shuai, Y. Fang, J. Yao, *J. Am. Chem. Soc.,* **2003**, *125*, 6740.

[29] S.-J. Lim, B.-K. An, S. D. Jung, M.-A. Chung, S. Y. Park, *Angew. Chem. Int. Ed.*, **2004**, *43*, 6346.

[30] F. F. Abram. *Homogenous Nucleation Theory*, **1974**, Academic Press, NY.

[31] V. K. La Mer, R. H. Dinegar, *J. Am. Chem. Soc.*, **1950**, *72*, 4847.

[32] C. N. R. Rao, A. Muller, A. K. Cheetham. *Nanomaterials chemistry: recent developments and new directions.* **2007**, Wiley-VCH, Weinheim. Cap. 4, p. 141.

[33] P. F. Luckham, *Adv. Colloid Interface Sci.*, **2004**, *111*, 29.

[34] H. C. Hamaker, *Physica*, **1937**, *4*, 1058.

[35] http://www.nanocomposix.com/kb/general/characterization-techniques

[36] E. J. W. Verwey, J. T. G. Overbeek. *Theory of stability of lyophobic colloids.* **1948**, Elsevier, Amsterdam.

[37] L. Blum, *J. Phys. Chem.* **1977**, *81*, 136.

[38] B. A. Rozemberg, R. Tenne, *Prog. Polym. Sci.*, **2008**, *33*, 40.

[39] H. Kasai, H. Kamatani, S. Okada, H. Oikawa, H. Matsuda, H. Nakanishi, *Jpn. J. Appl. Phys.*, **1996**, *35*, L221.

[40] H. Fu, B. H. Loo, D. Xiao, R. Xie, X. Ji, J. Yao, B. Zhang, L. Zhang, *Angew. Chem. Int. Ed.*, **2002**, *41*, 962.

[41] A.-D. Peng, D.-B. Xiao, Y. Ma, W.-S. Yang, J.-N. Yao, *Adv. Mater.*, **2005**, *17*, 2070.

[42] J. Luo, Z. Xie, J. W. Lam, L. Cheng, H. Chen, C. Qiu, H. S. Kwok, X. Zhan, Y. Liu, D. Zhu, B. Z. Thang, *Chem. Commun.*, **2001**, 1740.

[43] C. Sissa, V. Parthasarathy, D. Drouin-Kucma, M. H. V. Werts, M. Blancard-Desce, F. Terenziani. *Phys. Chem. Chem. Phys.*, **2010**, *12*, 11715.

[44] Y. Hong, J. W. Y. Lam, B. Z. Tang. *Chem. Comm.*, **2009**, 4332.

[45] H. Tong, Y. Hong, Y. Dong, Y. Ren, M. Häussler, J. W. Y. Lam, K. S. Wong, B. Z. Tang. *J. Phys. Chem. B*, **2007**, *111*, 2000.

[46] S. Kim, Q. Zheng, G. S. He, D. J. Bharali, H. E. Pudavar, A. Baev, P. N. Prasad. *Adv, Funct. Mater.*, **2006**, *16*, 2317.

[47] B.-K. An, A.-K. Kwon, S.-D. Jung, S. Y. Park. *J. Am. Chem. Soc.*, **2002**, *124*, 14410.

[48] M. Melucci, L. Favaretto, A. Zanelli, M. Cavallini, A. Bongini, P. Maccagnani, P. Ostoja, G. Derue, R. Lazzaroni, G. Barbarella. *Adv. Funct. Mater.*, **2010**, *20*, 445.

[49] A. Loudet, K. Burgess. *Chem. Rev.*, **2007**, *107*, 4891.

[50] J.-H. Olivier, J. Widmaier, R. Ziessel. *Chem. Eur. J.*, **2011**, *17*, 11709.

[51] S. Badré, V. Monnier, R. Méallet-Renault, C. Dumas-Verdes, E. Y. Schmidt, A. I. Mikhaleva, G. Laurent, G. Levi, A. Ibanez, B. A. Trofimov, R. P. Pansu. *J. Photochem. Photobiol. A*, **2006**, *183*, 238.

[52] A. Burghart, H. Kim, M. B. Welch, L. H. Thoresen, J. Reibenspies, K. Burgess. *J. Org. Chem.*, **1999**, *64*, 7813.

[53] F. Bergstrom, I. Mikhalyov, P. Hagglof, R. Wortmann,T. Ny, L.B.A. Johansson. *J. Am. Chem. Soc.*, **2002**, *124*, 196.

[54] H. Tajalli, A. Ghanadzadeh Gilani, M.S. Zakerhamidi, P. Tajalli. *Dyes and Pigments*, **2008**, *78*, 15.

[55] E.G. Marson. *Optics Commun.*, **1981**, *37*, 56.

[56] P.R. Hammond. *Optics Commun.*, **1979**, *29*, 331.

[57] S.L. Bondarev, V.N. Knyukshto, V.I. Stepuro, A.P. Stupak, A.A. Turban. *J. Appl. Spectros.*, **2004**, *71*, 194.

[58] P. Greespan, S.D. Fowler. *J. Lipid Res.*, **1985**, *26*, 781.

[59] G. Diaz, M. Melis, B. Batetta, F. Angius. A.M. Falchi, *Micron*, **2008**, *39*, 819.

[60] J.R. Daban, *Electrophoresis*, **2001**, *22*, 874.

[61] S.B. Ruvinov, X.J. Yang, K.D. Parris, U. Banik, S.A. Ahmed, E.W. Miles, D.L. Sackett. *J. Biol. Chem.*, **1995**, *270*, 6357.

[62] P. Romoino, E. Margallo, G. Nicolo. *J. Lipid Res.*, **1996**, *37*, 1207.

[63] N.C. Maiti, M.M. Krishna, P.J. Britto, N. Periasamy. *J. Phys. Chem. B*, **1997**, *101*, 11051.

[64] A. Datta, D. Mandal, S.K. Pal, K. Bhattacharya. *J. Phys. Chem. B*, **1997**, *101*, 10221.

[65] W. Denk, J. H. Strickler, W. W. Webb. *Science*, **1990**, *248*, 73.

[66] P. T. C. So. Two-photon Fluorescence Light Microscopy. *Enciclopedia of Life Sciences*. **2002** Macmillan Publishers Ltd, Nature Publishing Group.

[67] C. -H. Tsoa, W. Loa, P. -Y. Huangb, T. -L. Hsub, C. -C. Yehb, S. -J. Linc, S. -H. Jeec, C. -C. Chen, C. -Y. Donga. *Proc. of SPIE*, **2004**, *5323*, 360.

[68] J. M. Squirrell, D. L. Wokosin, J. G. White, and B. D. Bavister, *Nat. Biotech.*, **1999**, *17*, 763.

[69] K. Svoboda, K, W. Denk, D. Kleinfeld, and D. W. Tank, *Nature*, **1997**, *385*, 161.

[70] P. T. C. So, H. Kim, and I. E. Kochevar, *Opt. Exp.*, **1998**, *3*, 339.

[71] K. W. Dunn, T. A. Sutton. *ILAR J.*, **2008**, *49*, 66.

[72] A. A. Heikal, W. W. Webb, *Proc. SPIE,* **2002**, 4812.

[73] H. M. Kim, B. R. Cho, *Acc. Chem. Res.,* **2009**, *42*, 863.

[74] H. M. Kim, B. R. Cho, *Chem. Asian. J.,* **2011**, *6*, 58.

[75] S. Sumalekshmy, C. J. Fahrni, *Chem. Mater.,* **2011**, *23*, 483..

[76] A. R. Kherlopian, T. Song, Q. Duan, M. A. Neimark, M. J. Po, J. K. Gohagan, A. F. Laine. *BMC System Biology*, **2008**, *2*, 74.

[77] J. Gao, K. Chen, R. Xie, J. Xie, S.-W. Lee, Z. Cheng, X. Peng, X. Chen. *Small*, **2010**, *6*, 256.

[78] A. J. Tavares, L. Chong, E. Petryayeva, W. R. Algar, U. J. Krull. *Anal. Bioanal. Chem.,* **2011**, *399*, 2331.

[79] T. Y. Ohulchanskyy, I. Roy, K.-T. Yong, H. E. Pudavar, P. N. Prasad. *Advanced Review*, **2010**, *2*, 162.

[80] J. Choi, A. Burns, R. M. Williams, Z. Zhou, W. R. Zipfel, U. Wiesner, A. Y. Nikitin. J. *Biomed. Opt.*, **2007**, *12*, 064007.

[81] P. Sharma, S. Brown, G. Walter, S. Santra, B. Moudgil. *Adv. Colloid. Interf. Sci.*, **2006**, 471.

[82] J. Mérian, J. Gravier, F. Navarro I. Texier. *Molecules*, **2012**, *17*, 5564.

[83] M. H. V. Werts, S. Gmouh, O. Mongin, T. Pons, M. Blanchard-Desce. *J. Am. Chem. Soc.*, **2004**, *126*, 16294.

[84] L. Ventelon, S. Charier, L. Moreaux, J. Mertz, M. Blanchard-Desce. *Angew. Chem.*, **2001**, *113*, 2156; *Angew. Chem. Int. Ed.* **2001**, *40*, 2098.

[85] B. R. Cho, K. H. Son, S. H. Lee, Y.-S. Song, Y.-K. Lee, S.-J. Jeon, J. H. Choi, H. Lee, M. Cho. *J. Am. Chem. Soc.*, **2001**, *123*, 10039.

[86] O. Mongin, A. P. Quintana, F. Terenziani, D. Drouin, C. Le Droumaguet, A.-M. Caminade, J.-P. Majoral, M. Blanchard-Desce. *New J. Chem.*, **2007**, *31*, 1354.

[87] O. Mongin, T. R. Krishna, M. H. V. Werts, A.-M. Caminade, J.-P. Majoral and M. Blanchard-Desce. *Chem. Commun.*, **2006**, 915.

[88] H. Y. Kim, T. G. Bjorklund, S.-H. Lim, C. J. Bardeen. *Langmuir*, **2003**, *19*, 3941.

[89] Q. Zhao, K. Li, S. Chen, A. Qin, D. Ding, S. Zhang, Y. Liu, B. Liu, J. Zhi Sun, B. Zhong Tang. *J. Mater. Chem.*, **2012**, in press.

[90] J. B. Birks. *Photophysics of Aromatic Molecules*, **1970**, Wiley, London.

[91] A. Silinsh, *Organic Molecular Crystals*. **1980**, Springer-Verlag, Berlin.

[92] Y. Shirota, *J. Mater. Chem.* **2005**, *15*, 75.

[93] F. Terenziani, M. Morone, S. Gmouh, M. Blanchard-Desce. *ChemPhysChem.*, **2006**, *7*, 685.

[94] F. Terenziani, V. Parthasarathy, A. Pla-Quintana, T. Maishal, A.-M. Caminade, J.-P. Majoral, M. Blanchard-Desce. *Angew. Chem. Int. Ed.*, **2009**, *48*, 8691.

[95] E. Ishow, A. Brosseau, G. Clavier, K. Nakatani, P. Tauc, C. Fiorini-Debuisschert, S. Neveu, O. Sandre, A. Léaustic. *Chem. Mater.*, **2008**, *20*, 6597.

[96] D. R. Larson, W. R. Zipfel, R. M. Williams, S. W. Clark, M. P. Bruchez, F. W. Wise, W. W. Webb. *Science,* **2003**, *300*, 1434.

[97] [54] V. Lebret, L. Raehm, J.-O. Durand, M. Smaihi, C. Gerardin, N. Nerambourg, M. H. V. Werts, M. Blanchard-Desce. *Chem. Mater.* **2008**, *20*, 2174.

[98] T. Sato and R. Ruch. *Stabilization of colloidal dispersion by polymer adsorption*. Marcel Dekker Inc., **1980**, New York.

[99] R. J. Hunter, *Zeta Potential in Colloid Science: Principles and Applications*, Academic Press, **1981**, London.

[100] A. J. Bard, L. R. Faulkner, *Electrochemical Methods*, 2:nd edn, John Wiley & Sons Inc., **2001**.

[101] D.H. Napper, *Polymeric Stabilization of Colloidal Dispersions*. Academic Press, **1983**, London.

[102] J. N. Israelachvili, *Intermolecular and surface forces*, Academic Press, **1992**.

[103] H. Katagi, H. Kasai, S. Okada, H. Oikawa, K. Komatsu, H. Matsuda, Z. Liu, H. Nakanishi. *Jpn. J. Appl. Phys.* **1996**, *35*, L1364.

[104] K. Baba, H. Kasai, A. Masuhara, S. Okada, H. Oikawa, H. Nakanishi. *Jpn. J. Appl. Phys.,* **2007**, *46*, 7558.

[105] R. O. Al-Kaysi, A. M. Müller, T.-S. Ahn, S. Lee, C. J. Bardeen. *Langmuir*, **2005**, *21*, 7990.

[106] R. Yasukuni, T. Asahi, T. Sugiyama, H. Masuhara, M. Sliwa, J. Hofkens, F. C. De Schryver, M. Van der Auweraer, A. Herrmann, K. Müllen. *Appl. Phys. A*, **2008**, *93*, 5.

[107] A. Spangenberg, R. Métivier, J. Gonzalez, K. Nakatani, P. Yu, M. Giraud, A. Léaustic, R. Guillot, T. Uwada, T. Asahi. *Adv. Mater.*, **2009**, *21*, 309.

[108] N. Tagawa, A. Masuhara, T. Onodera, H. Kasai, H. Oikawa. *J. Mater. Chem.*, **2011**, *21*, 7892.

[109] M. Amelia, D. Zoppitelli, C. Roscini, L. Latterini. C*hemPhysChem*, **2010**, *11*, 3089.

[110] A. G. L. Olive, A. Del Guerzo, C. Schäfer, C. Belin, G. Raffy, C. Giansante. *J. Phys. Chem. C*, **2010**, *114*, 10410.

[111] X. Li, Y. Qian, S. Wang, S. Li, G. Yang. *J. Phys. Chem. C*, **2009**, *113*, 3862.

[112] C. Vijayakumar, K. Sugiyasu, M. Takeuchi. *Chem. Sci.*, **2011**, *2*, 291.

[113] D. P. Hagberg, X. Jiang, E. Gabrielsson, M. Linder, T. Marinado, T. Brinck, A. Hagfeldt, L. Sun. *J. Mater. Chem.* **2009**, *19*, 7232.

[114] A. G. L. Olive, A. Del Guerzo, C. Schafer, C. Belin, G. Raffy, C. Giansante. J. Phys. Chem. C, **2010**, 10410.

[115] A.-D. Peng, D.-B. Xiao, Y. Ma, W.-S. Yang, J.-N. Yao. Adv. Mater., **2010**, *17*, 2070.

[116] J. L. Chavez, H. Jiang, R. S. Duran. Nanotechnology, **2010**, *21*, 055703.

[117] C. Vijayakumar, K. Sugiyasu, M. Takeuchi. Chem. Sci., **2011**, *2*, 291.

[118] Q. Li, C. Zhang, J. Y. Zheng, Y. S. Zhao, J. Yao. Chem. Commun., **2012**, *48*, 85.

[119] C. Zhang, J. Y. Zheng, Y. S. Zhao, J. Yao. Adv. Mater. **2011**, *23*, 1380.

[120] F.Qian, S.Gradecak, Y. Li, C. Y. Wen and C. M. Lieber. Nano Lett., **2005**, *5*, 2287.

[121] M.Green. Small, **2005**, *1*, 684.

[122] C. W. Chan and S. Nie, Science. **1998**, *281*, 2016.

[123] H. G. Zhu, M. J. McSchane, J. Am. Chem. Soc. **2005**, *127*, 13448.

[124] H. Y. Huang, E. E. Remsen andK. L.Wooley, Chem. Commun., **1998**, 1415.

[125] C. Zhang, J. Y. Zheng, Y. S. Zhao, J. Yao. Chem. Commun., **2010**, *46*, 4959.

[126] L. Kang, Y. Chen, D. Xiao, A. Peng, F. Shen, X. Kuang, H. Fu, J. Yao. Chem. Commun., **2007**, 2695.

[127] C. Song, Z. Ye, G. Wang, J. Yuan, Y. Guan. ACS Nano, **2010**, *4*, 5389.

[128] L. Kang, Y. Chen, D. Xiao, A. Peng, F. Shen, X. Kuang, H. Fu, J. Yao. Chem. Commun. **2007**, 2695.

[129] V. Sundstrom. Annu. Rev. Phys. Chem., **2008**, *59*, 53.

[130] T. Wilson and J. W. Hastings. Annu. Rev. Cell. Dev. Biol., **1998**, *14*, 197.

[131] B. Valeur, Molecular Fluorescence: Principles and Applications. **2001**, Wiley-VCH.

[132] T. Renger. Photosynth. Res., **2009**, *102*, 471.

[133] T. Förster. Ann. Phys., **1948**, *437*, 55.

[134] T. Förster. Disc. Far. Soc., **1959**, *27*, 7.

[135] T. Förster. Radiation Res. Supp., **1960**, *2*, 326.

[136] T. Förster. "Modern quantum chemistry", **1965**, Academic Press, p. 93.

[137] S. Saha and A. Samanta. J. Phys. Chem. A, **2002**, *106*, 4763.

[138] D. Bera, L. Qian, T.-K. Tseng, P. H. Holloway. Materials **2010**, *3*, 2260.

[139] I.-Y. Jeon, J.-B. Baek. Materials **2010**, *3*, 3654.

[140] T. Pellegrino, S. Kudera, T. Liedl, T. A. Munoz Javier, L. Manna, W. J. Parak. Small **2005**, *1*, 48.

[141] P. Zijlstra, M. Orrit. Rep. Prog. Phys., **2011**, *74*, 106401.

[142] V. Biju, T. Itoh, A. Anas, A. Sujith, M. Ishikawa. Anal. Bioanal. Chem., **2008**, *391*, 2469.

[143] P. Ball, L. Garwin. Nature, **1992**, *355*, 761.

[144] T. K. Sau, A. L. Rogach, F. Jäckel, T. A. Klar, J. Feldmann. Adv. Mater., **2010**, *22*, 1805.

[145] R. J. Gehr, R. W. Boyd. Chem. Mater., **1996**, *8*, 1807.

[146] C. W. Chen, C. H. Wang, C. M. Wei, Y. F. Chen. Appl. Phys. Lett., **2009**, *94*, 071906.

[147] A. Patra, C. G. Chandaluri, T. P. Radhakrishnan. Nanoscale, **2012**, *4*, 343.

[148] Y. S. Zhao, H. Fu, A. Peng, Y. Ma, D. Xiao, J. Yao. Adv. Mater., **2008**, *20*, 2859.

[149] A. J. Gesquiere, T. Uwada, T. Asahi, H. Masuhara, P. F. Barbara. Nano Lett., **2005**, *5*, 1321.

[150] J. L. Chávez, H. Jiang, R. S. Duran. Nanotechnology, **2010**, *21*, 055703.

[151] C. Song, Z. Ye, G. Wang, J. Yuan, Y. Guan. ACS Nano, **2010**, *4*, 5389.

[152] C. Zhang, J. Y. Zheng, Y. S. Zhao, J. Yao. Chem. Commun., **2010**, *46*, 4959.

[153] J. Chen, P. Zhang, G. Fang, P. Yi, F. Zeng, S. Wu. J. Phys. Chem. B, **2012**, *116*, 4354.

[154] L. Wang, T. Xia, L. Wang, H. Chen, L. Dong, G. Bian. Microchim. Acta, **2005**, *149*, 267.

[155] A. L. Stevens, A. Kaeser, A. P. H. J. Schenning, L. M. Herz. ACS Nano, **2012**, *6*, 4777.

[156] L. Kang, Y. Chen, D. Xiao, A. Peng, F. Shen, X. Kuang, H. Fu, J. Yao. Chem. Commun., **2007**, 2695.

[157] R. J. Hunter. Zeta Potential in Colloid Science: Principles and Applications, Academic Press, London, **1981**.

[158] H. Ishii, K. Sugiyama, E. Ito, K. Seki. Adv. Mater., **1999**, *11*, 605.

[159] S. C. Veenstra, H. T. Jonkman. J. Polym. Sci. Part B: Polym. Phys., **2003**, *41*, 2549.

[160] W. Osikowicz, M. P. de Jong, W. R. Salaneck. Adv. Mater., **2007**, *19*, 4213.

[161] V. Chiş, G. Mile, R. Ştiufiuc, N. Leopold, M. Oltean. J. Mol. Struct., **2009**, 47.

[162] C. Xu and W. W. Webb. J. Opt. Soc. Am. B, **1996**, *13*, 481

# List of Publications

- V. Parthasarathy, S. Fery-Forgues, E. Campioli, G. Recher, F. Terenziani, M. Blanchard-Desce.
  *Dipolar versus Octupolar Triphenylamine-Based Fluorescent Organic Nanoparticles as Brilliant One- and Two-Photon Emitters for (Bio)imaging.*
  Small, **2011**, *7*, 3219.

- E. Campioli, C. Rouxel, M. Campanini, L. Nasi, M. Blanchard-Desce, F. Terenziani.
  *Enforcing Luminescence at Organic Nanointerfaces: Luminescence Spatial Confinement and Amplification in Molecular-Based Core–Shell Nanoparticles.*
  Small, **2013**, DOI: 10.1002/smll.201202504

### Articles in Preparation

- E. Campioli, F. Terenziani, M. Blanchard-Desce.
  *Morphological and Spectroscopic Characterizations of Triphenylamine-based Nanoparticles Reprecipitated under Ultrasounds and Low-Concentration Additives.*
  In preparation.

- E. Campioli, F. Terenziani, M. Blanchard-Desce, M. Campanini.
  *Study of three layer Core@Shell@Shell Organic Nanoparticles During Time: the Effect of PMMA doping on Fluorescence Preservation.*

In preparation.